INFORMATION TO USERS

This manuscript has been reproduced from the microfilm master. UMI films the text directly from the original or copy submitted. Thus, some thesis and dissertation copies are in typewriter face, while others may be from any type of computer printer.

The quality of this reproduction is dependent upon the quality of the copy submitted. Broken or indistinct print, colored or poor quality illustrations and photographs, print bleedthrough, substandard margins, and improper alignment can adversely affect reproduction.

In the unlikely event that the author did not send UMI a complete manuscript and there are missing pages, these will be noted. Also, if unauthorized copyright material had to be removed, a note will indicate the deletion.

Oversize materials (e.g., maps, drawings, charts) are reproduced by sectioning the original, beginning at the upper left-hand corner and continuing from left to right in equal sections with small overlaps. Each original is also photographed in one exposure and is included in reduced form at the back of the book.

Photographs included in the original manuscript have been reproduced xerographically in this copy. Higher quality 6" x 9" black and white photographic prints are available for any photographs or illustrations appearing in this copy for an additional charge. Contact UMI directly to order.

UMI®

Bell & Howell Information and Learning
300 North Zeeb Road, Ann Arbor, MI 48106-1346 USA
800-521-0600

LIGHT SCATTERING BY NONSPHERICAL PARTICLES: NUMERICAL SIMULATION AND APPLICATIONS

By

Wenbo Sun

SUBMITTED IN PARTIAL FULFILLMENT OF THE
REQUIREMENTS FOR THE DEGREE OF
DOCTOR OF PHILOSOPHY
AT
DALHOUSIE UNIVERSITY
HALIFAX, NOVA SCOTIA
AUGUST 2000

DALHOUSIE UNIVERSITY

FACULTY OF GRADUATE STUDIES

The undersigned hereby certify that they have read and recommend to the Faculty of Graduate Studies for acceptance a thesis entitled "Light Scattering By Nonspherical Particles: Numerical Simulation and Applications"

by Wenbo Sun

in partial fulfillment of the requirements for the degree of Doctor of Philosophy.

Dated: August 25, 2000

External Examiner

Research Supervisor

Examining Committee

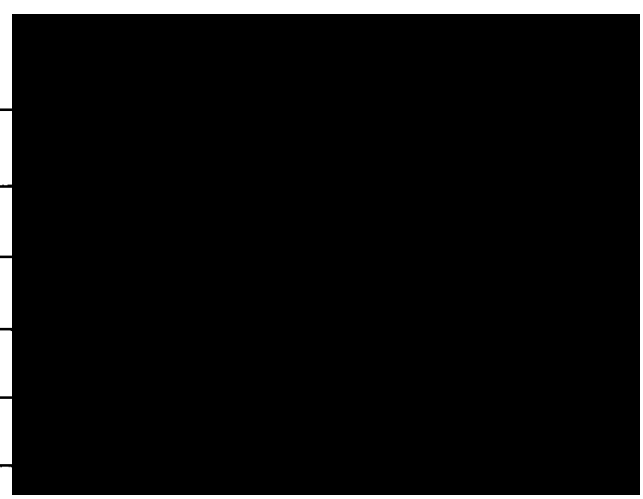

DALHOUSIE UNIVERSITY

Date: **August 2000**

Author: **Wenbo Sun**

Title: **LIGHT SCATTERING BY NONSPHERICAL PARTICLES: NUMERICAL SIMULATION AND APPLICATIONS**

Department: **Oceanography**

Degree: **Ph.D.** Convocation: **October** Year: **2000**

Permission is herewith granted to Dalhousie University to circulate and to have copied for non-commercial purposes, at its discretion, the above title upon the request of individuals or institutions.

Signature of Author

To Fangdi and Cindy

Contents

List of Tables

List of Figures

Abstract

Remote sensing studies and climate research require precise knowledge of the single-scattering properties of nonspherical particles. In this study, a three dimensional finite-difference time domain (FDTD) program with a perfectly matched layer (PML) absorbing boundary condition is developed to provide a numerical solution for light scattering by nonspherical dielectric particles. The FDTD model is used to study the single-scattering properties of cirrus ice crystals in the infrared and to investigate the scattering patterns by particles with various morphologies. The FDTD scheme is extended to simulate light scattering and absorption by particles with large complex refractive index. The FDTD scheme is also extended to be applied to simulate light propagation in dielectric media with particles embedded.

The anomalous diffraction theory (ADT) is considered to be suitable for the calculation of the extinction and absorption efficiencies for nonspherical particles with small refractive indices. In this study, an analytical ADT model for light scattering by arbitrarily oriented hexagonal and cylindrical particles is developed. The differences between the analytical ADT model and the simplified ADT model, which is often used in climate and remote sensing studies, are also examined.

Using the FDTD model, we examine a number of commonly used approximate methods including Mie theory, the ADT, and the geometrical optics method (GOM), for the calculation of the scattering and absorption properties of hexagonal ice crystals in cirrus clouds. Some problems in the retrieval of cirrus particle size are addressed.

Symbols and Abbreviations

a	radius of a particle
α_s, α_l	slope of size distribution
α, β	azimuth and elevation angle
a_n, b_n, c_n, d_n	coefficients for the expansion of the scattering and internal fields in spherical harmonics
ABC	absorbing boundary condition
ADT	anomalous diffraction theory
$B(T)$	Planck function
β, β_a	extinction and absorption coefficient
c	wave speed
CMP	composite method
D	width of a particle
D_{ge}	generalized effective particle size
DFT	discrete Fourier transform
D_r	radial component of the electric displacement
$d\sigma$	surface area element
Δs, Δx, Δy, Δz	the FDTD grid cell size
E_0	reference incident electric field
E_n	$i^n E_0(2n+1)/n(n+1)$
$\vec{E}$	electric field vector
$\vec{E}_s$	scattered electric field vector
$\vec{E}_t$	internal electric field vector
E_x, E_y, E_z	electric field components in x, y and z direction
E_{xy}, E_{xz}	E_x split in the PML
E_{yx}, E_{yz}	E_y split in the PML
E_{zx}, E_{zy}	E_z split in the PML

ϵ	permittivity (dielectric constant), emissivity
ϵ_0	permittivity in vacuum
ϵ_i	imaginary part of permittivity
ϵ_i'	imaginary part of host medium permittivity
ϵ_r	real part of permittivity
ϵ_r'	real part of host medium permittivity
ϕ	azimuth angle
$\mathbf{F}$	transformation matrix for incident and scattered Stokes parameters
FDTD	finite-difference time domain
g	asymmetry factor
$\hat{g}$	asymmetry factor for randomly oriented particles
$G(\vec{r}, \vec{\xi})$	3-D Green function
GOM	geometric optics method
h	height of a particle
$h_n^{(1)}$	spherical Hankel function
$\vec{H}$	magnetic field vector
$\vec{H}_s$	scattered magnetic field vector
$\vec{H}_t$	internal magnetic field vector
H_x, H_y, H_z	magnetic field components in x, y and z direction
H_{xy}, H_{xz}	H_x split in the PML
H_{yx}, H_{yz}	H_y split in the PML
H_{zx}, H_{zy}	H_z split in the PML
Im	imaginary part
IWC	ice water content
j_n	spherical Bessel function
k	wavenumber
k_t	wavenumber inside the particle
L	length of a particle
L_1	lower limit of particle length
L_2	upper limit of particle length
L_*	L for the minimum in the bimodal size distribution
$\bar{L}_l$	mean maximum dimension for large particles
$\bar{L}_s$	mean maximum dimension for small particles
λ	wavelength
λ_0	wavelength in vacuum
λ_d	wavelength in particle

m	refractive index
m_i	imaginary part of refractive index
m_r	real part of refractive index
m_t	refractive index of the particle
$\vec{M}_{oln}^{(1)}, \vec{M}_{eln}^{(1)}, \vec{N}_{oln}^{(1)}, \vec{N}_{eln}^{(1)}$	spherical harmonics using Bessel function j_n
$\vec{M}_{oln}^{(3)}, \vec{M}_{eln}^{(3)}, \vec{N}_{oln}^{(3)}, \vec{N}_{eln}^{(3)}$	spherical harmonics using Hankel function $h_n^{(1)}$
MieS	Mie theory for surface area equivalent particles
MieV	Mie theory for volume equivalent particles
MieVS	Mie theory for both volume and surface area equivalent particles
μ	permeability
μ'	permeability of host medium
μ_0	permeability in vacuum
μ_t	permeability of the particle
n(L)	size distribution for particles
N_{0l}	quantity relating size distribution for large particles to IWC
N_{0s}	quantity relating size distribution for small particles to IWC
N_l	size distribution for large particles
N_s	size distribution for small particles
ν	deviation of the size distribution from exponential mode
ω	angular frequency
P	projected area
$\hat{P}$	projected area for randomly oriented particles
$\mathbf{P}$	phase matrix
$\vec{P}$	electric polarization vector
PML	perfectly matched layer
P_n^1	associated Legendre polynomial
π_n	$P_n^1/sin\theta$
ψ	phase delay
Ψ	orientation angle of electric field in the constant-phase plane
ψ_n, ψ_n^*	Riccati-Bessel function and complex conjugate of the Riccati-Bessel function of order n
ψ_n', $\psi_n'^*$	derivatives of the Riccati-Bessel function and complex conjugate of the Riccati-Bessel function of order n
Q_a, Q_e, Q_s	absorption, extinction and scattering efficiency
$\hat{Q}_a$, $\hat{Q}_e$, $\hat{Q}_s$	absorption, extinction and scattering efficiency for randomly oriented particles

$\mathbf{P}$	phase matrix
ρ_i	density of ice
r_p, r_s, r_v, r_{vs}	radius of equivalent particle
Re	real part
$R(0)$	reflection coefficient for normal incidence
$R(\theta)$	reflection coefficient for incidence angle θ
S	surface area
SADT	simplified ADT
$s(0)$	forward-scattering amplitude
s_1, s_2, s_3, s_4	elements of the amplitude scattering matrix
σ_a, σ_e, σ_s	absorption, extinction and scattering cross-section
$\hat{\sigma}_a$, $\hat{\sigma}_e$, $\hat{\sigma}_s$	absorption, extinction and scattering cross-section for randomly oriented particles
σ_m	maximum conductivity
$\sigma(\rho)$	conductivity at position ρ
σ_x, σ_y, σ_z	electric conductivity of the PML
σ_x^*, σ_y^*, σ_z^*	magnetic conductivity of the PML
t	time
τ_n	$dP_n^1/d\theta$
θ	zenith angle
T_c	cloud temperature
T_m	measured temperature
T_s	surface temperature
TOA	top of atmosphere
V	volume
W_a, W_e, W_s	absorption, extinction and scattering rate of the particle
x	particle size parameter ($2\pi a/\lambda_0$)
ξ_n, ξ_n^*	Riccati-Hankel function and complex conjugate of the Riccati-Hankel function of order n
ξ_n', $\xi_n'^*$	derivatives of the Riccati-Hankel function and complex conjugate of the Riccati-Hankel function of order n

Acknowledgements

I would like to thank my supervisor Dr. Qiang Fu for his support, constructive ideas and strict supervision. My sincere gratitude goes to the members of my supervisory committee. Dr. Petr Chýlek of the Physics Department and the Oceanography Department, Dr. Ian Folkins of the Oceanography Department, and Dr. Gorden Videen of the US Army Research Lab for their helpful suggestions and criticism. I also thank Dr. Michael Mishchenko of the NASA Goddard Institute for Space Studies for providing with me his papers and T-matrix code, and for taking on the job of the external examiner.

I wish to extend my gratitude to Dr. Ping Yang of the NASA Goddard Space Flight Center for his assistance in the early stage of this research. Also, great thanks to Dr. Zhizhang Chen of the Electrical and Computer Engineering Department for his great help on many difficult problems during my programming for the 3D PML FDTD model. I also should thank Dr. David Secker of the Science and Technology Research Center, University of Hertfordshire, for his offering the measurement results for light scattering by droplets. Special thanks to Dr. Majdi Baddourah of the National Energy Research Scientific Computing Center (NERSC) for his great help with the NERSC machines.

Also, thanks to my wife Huiying for her patience and encouragement, and thanks to my elder daughter Fangdi and my younger daughter Cindy for giving me so much happiness. And finally, I should also thank Colonel Hansen and the late Mrs. Hansen for their great help with my housing and living in Halifax.

Chapter 1

Introduction

Cirrus clouds, primarily present in the upper troposphere and lower stratosphere, are globally distributed and are composed almost exclusively of nonspherical ice crystals (Liou 1986; Starr 1987; Miloshevich *et al.* 1992). Remote sensing studies and climate research require precise knowledge of the single-scattering properties of nonspherical particles including cirrus ice crystals, snowflakes and aerosols, due to their effect on radiative transfer in the atmosphere system (Stephens *et al.* 1990; Takano *et al.* 1992; Fu *et al.* 1999). Light scattering and absorption processes depend not only on the incident wavelength and the refractive index of the particle, but also on the particle size, shape and orientation. Because for a particle with an arbitrary shape, an appropriate coordinate system for the boundary condition at the particle surface cannot be imposed, it appears unlikely to produce a universally effective exact solution for the light scattering and absorption processes of these natural particles. To date, except for some simple particle shapes, such as spheres (Mie 1908), double sphere systems (Videen *et al.* 1996), spheroids (Asano and Yamamoto 1975), infinite circular cylinders (Rayleigh 1918; Wait 1955), Chebyshev particles (Mugnai and Wiscombe 1986), finite circular cylinders (Mishchenko *et al.* 1996a) and cubes (Laitinen and Lumme 1998), theoretical scattering treatments are not available for the scattering and absorption by nonspherical particles. Non-analytical solutions such as Rayleigh theory (Rayleigh 1871) can be applied when the particle size parameter is much

smaller than one. When the size parameter is larger than ~40, the geometric optics method (GOM) (Takano and Liou 1989; Yang and Liou 1996b; Macke *et al.* 1996) can be used for nonspherical particles. However, in the resonance region (Barber and Yeh 1975), Rayleigh theory and the GOM are not applicable because of the assumptions pertaining to each technique.

Since there are significant observational and computational difficulties in determining the radiative properties of nonspherical ice crystals in cirrus clouds, it is common practice to approximate nonspherical ice crystals by spherical particles (e.g., Stephens *et al.* 1990; Sun and Shine 1995), spheroids (Asano and Yamamoto 1975) or long circular cylinders (Liou 1972; Stephens 1980), so that the exact theories can be used. Unfortunately, none of these approaches accounts for the hexagonal structure of ice crystals with finite length.

Additionally, it was recently suggested that the anomalous diffraction theory (ADT) (van de Hulst 1957) would be an appropriate method to calculate the single scattering properties of nonspherical particles (Mitchell 1995). The ADT is an approximate method, which is often used to calculate the extinction and absorption coefficients of water droplets and ice crystals (e.g., Ackerman and Stephens 1987; Mitchell and Arnott 1994). The ADT can be applied analytically to nonspherical particles of various shapes. However, by comparing results from the ADT with those from the discrete dipole approximation, Maslowska *et al.* (1994) concluded that the ADT cannot be used for light scattering and absorption by nonspherical particles without verification with rigorous methods. Furthermore, due to the difficulty in obtaining analytical or numerical solutions for randomly oriented particles using the original notation of the ADT, a randomly oriented particle with a volume of V and a projected area of P is usually converted to a cylinder with the same volume but a thickness of V/P. The light extinction and absorption cross-sections of the randomly oriented particle are then approximated using the ADT to the cylinder with the incident radiation normal to the base of the cylinder (Bryant and Latimer 1969). This simplified ADT is widely used (Mitchell and Arnott 1994; Arnott *et al.* 1994).

However, like the ADT itself, the accuracy of this simplification needs to be checked.

To get accurate solutions for the radiative properties of nonspherical particles in the resonance region, numerous promising approaches, including the method of moments (Harrington 1968; Morgan, 1981), the discrete-dipole approximation (DDA) (Purcell and Pennypacker 1973; Singham and Bohren 1987; Draine 1988; Flatau *et al.* 1990; Draine and Flatau 1994; Draine 1998), the digitized Green-function technique (Goedecke and O'Brien 1988), the integral equation technique (Chen and Islander 1990), the T-matrix or extended boundary condition method (Waterman 1971; Barber and Hill 1990; Mishchenko *et al.* 1996b), and the multiple-scattering approach (Chiappetta 1980), have been developed. These approaches are usually applicable to size parameters less than approximately 15 in practice and/or to specific shapes with smooth and continuous surfaces. Among these light scattering models, the most frequently used methods are the DDA and the T-matrix approach.

The DDA was first developed by Purcell and Pennypacker (1973) for scattering and absorption calculations involving dielectric grains of cubic shape whose sizes are comparable to or smaller than the incident wavelength. It is a flexible technique for calculating the light scattering and absorption by particles with arbitrary shapes and composition. The DDA consists of approximating the actual target by an array of the dipoles. Each of the dipoles is subject to an electric field which is the sum of the incident wave and the electric fields due to all of the other dipoles. Through the solution of the electric field at each dipole position, the scattering and absorption properties of the target can be obtained. Because the DDA replaces the solid particle with an array of point dipoles occupying positions on a cubic lattice, and the lattice spacing must be small compared to the wavelength of the incident light in the particle, the DDA requires large computer storage and CPU time. The DDA works well for materials with $|m-1| \leq 3$ and target dimension $D \leq 5\lambda$, where λ is the wavelength in the surrounding medium (Draine 1998).

The T-matrix approach (Waterman 1971) is one of the most powerful exact techniques for computing light scattering by nonspherical particles based on rigorously

solving Maxwell's equations. Standard T-matrix computations become ill-conditioned for particles with a small or zero imaginary part of the refractive index because of the strong effect of the ripple structure (Wielaard *et al.* 1997). Using a matrix inversion scheme based on a special lower triangular-upper triangular factorization, rather than on the standard Gaussian elimination, Wielaard *et al.* (1997) improved numerical stability of T-matrix computations for nonabsorbing and weakly absorbing nonspherical particles. As a result, the maximum convergent size parameter for particles with small or zero absorption can increase by a factor of several, and can exceed 100. However, although the method is claimed to be, potentially, applicable to any particle shapes, most practical implementations of the technique pertain to bodies of revolution such as spheroids and circular cylinders.

To compute the single-scattering properties for arbitrarily-shaped particles such as ice crystals in cirrus clouds, we develop a numerical scheme in this study by using the finite-difference time domain (FDTD) technique. The finite-difference time domain (FDTD) formulation (Yee 1966) for electromagnetic field problems is a direct numerical solution of Maxwell time-dependent curl equations, and is an elegant and robust tool for solving light-scattering problems. The scheme treats the scattering and absorption of the particle as an initial value problem, and it can be applied to particles of arbitrary shapes and composition. Pioneered by the initial work of Yee (1966) and many other electrical engineers, the FDTD method has been used extensively to solve various kinds of electromagnetic problems. With the development of a number of highly absorbing boundary conditions from the late 1970's to 1990's, the usefulness of the FDTD method in dealing with the scattering by an arbitrarily shaped or inhomogeneous object has been widely recognized. Yang and Liou (1995; 1996a) employed the FDTD method for light scattering by small ice crystals. A transmitting boundary condition was used. They showed that their FDTD model can work well for size parameters smaller than 10. For larger size parameters, the errors become significant.

The stability and accuracy of the FDTD method are determined by many factors,

such as the boundary conditions, cell size, scatterer size, etc. Improving the accuracy and stability of the FDTD program and applying the FDTD technique to different physical problems have been active pursuits over the past 15 years. In this study, our major effort concentrates on developing an accurate FDTD model for the calculation of light scattering and absorption by dielectric particles of arbitrary shapes. The FDTD for light scattering and absorption by dielectric particles with large complex refractive indices is also studied. Moreover, because of the practical importance in various fields of application and engineering, the FDTD model is further extended to simulate light propagation in dielectric media with particles or voids embedded. In Chapter 2, a three-dimensional FDTD program is developed, which is accurate for dielectric particles with size parameters as large as 40. In Chapter 3, appropriate treatments of the material properties and electromagnetic fields associated with the particle boundaries are presented so that the FDTD scheme can provide reliable solution for light scattering and absorption by particles with a wide range of refractive indices. In Chapter 4, the extension of the FDTD model for light propagation in dielectric media with particles or voids embedded is given. Additionally, to examine the applicability of the ADT in the study of the cirrus radiation effect and the remote sensing of the cirrus particle sizes, we develop the analytical ADT for finite hexagonal ice crystals and circularly cylindrical particles. The results from the original ADT and the simplified ADT are also compared. These are documented in Chapter 5. The applications of the FDTD model in the examination of the accuracy of the approximate light scattering models and in the retrieval of the microphysical properties of cirrus clouds are reported in Chapter 6. Conclusions are given in Chapter 7.

Chapter 2

Finite-difference time domain solution of light scattering by dielectric particles with a perfectly matched layer absorbing boundary condition

2.1 Introduction

Pioneered by the work of Yee (1966) and many other electrical engineers, the finite-difference time domain (FDTD) solutions of Maxwell's equations have been extensively applied to electromagnetic problems such as antenna design, radar cross section computation, waveguide analysis and some other open-structure problems. The FDTD technique is a numerical solution to Maxwell's equations, and is formulated by replacing temporal and spatial derivatives in Maxwell's equations with their finite-difference correspondences. In this method, the electric field grid, which is offset both

spatially and temporally from the magnetic field grid, is used to obtain update equations that yield the present fields throughout the computational domain in terms of the past fields. The update equations are used in a leap-frog scheme to incrementally march the electromagnetic fields forward in time. This method can be accurately applied to general electromagnetic structures, including particles of arbitrary shapes and composition. However, like other numerical approaches, the FDTD method requires large computer storage and large CPU time, even for particles with small size parameters. Moreover, the stability and accuracy of the FDTD program are determined by many factors such as the boundary condition, mesh size and scatterer size, etc. Topics related to improvement of its accuracy, reduction of memory and CPU time requirement, and applications to larger objects, have been actively pursued over the past 15 years (Holland 1994; Xu *et al.* 1997, 1998).

In applications of the FDTD technique to problems in an unbounded space, one of the key issues is the truncation of the computational domain via artificial boundary conditions. In the case of studying light scattering by particles of arbitrary shapes, it is essential to use the most effective and efficient boundary treatment. Yang and Liou (1996a) employed the FDTD method for light scattering by small nonspherical ice crystals using a transmitting boundary condition (Liao *et al.* 1984; Yang and Liou 1998a). They found that the FDTD works well for particles with size parameters smaller than 10. In this study, we develop a three-dimensional FDTD program to provide a numerical solution for light scattering by nonspherical dielectric particles. A newly developed, so-called perfectly matched layer (PML) absorbing boundary condition (ABC) (Berenger 1994,1996; Katz *et al.* 1994) is used to truncate the computational domain. We apply the FDTD program for light scattering by dielectric particles with size parameters as large as 40 to show its accuracy and efficiency. In Section 2.2, the FDTD with PML ABC for dielectric scatterers is formulated. In Section 2.3, the FDTD program is validated using the exact solutions. Some applications of the present program to nonspherical particles are presented in Section 2.4. The summary and conclusions are given in Section 2.5.

2.2 The finite-difference time domain method with a perfectly matched layer absorbing boundary condition

2.2.1 The finite-difference time domain method

The finite-difference time domain (FDTD) formulations of electromagnetic field problems is a direct numerical solution of Maxwell's time-dependent curl equations. Consider a source-free medium, where Maxwell's equations can be written as

$$\nabla \times \vec{E} = -\mu \frac{\partial \vec{H}}{\partial t}, \tag{2.1a}$$

$$\nabla \times \vec{H} = \epsilon \frac{\partial \vec{E}}{\partial t}, \tag{2.1b}$$

where $\vec{E}$ and $\vec{H}$ are the electric and magnetic fields, respectively; μ is the permeability, and ϵ is the permittivity of the dielectric medium.

Assuming that the time-dependent part of the electromagnetic field is $exp(-i\omega t)$, the electric and magnetic fields can be written in the form

$$\vec{E}(x, y, z, t) = \vec{E}(x, y, z) exp(-i\omega t), \tag{2.2a}$$

$$\vec{H}(x, y, z, t) = \vec{H}(x, y, z) exp(-i\omega t), \tag{2.2b}$$

where $\omega = kc$, k and c are the wavenumber and the speed of the electromagnetic wave, respectively, in free space.

ϵ in Eq.(2.1b) is complex for an absorptive medium and can be expressed as

$$\epsilon = \epsilon_r + i\epsilon_i. \tag{2.3a}$$

Since the refractive index $m = \sqrt{\epsilon\mu}$, and for nonferromagnetic medium μ is unity, the real and imaginary parts of ϵ may be expressed by the real and imaginary parts of m in the form

$$\epsilon_r = m_r^2 - m_i^2, \quad \epsilon_i = 2m_r m_i. \tag{2.3b}$$

To apply the FDTD method for light scattering by small ice crystals, Yang and Liou (1996a) introduced a way of transforming Maxwell's equations to a source-dependent form that governs the scattering process of a dielectric particle so that complex calculations can be avoided when the scatterer is absorptive. Here, the equivalent Maxwell's equations for absorptive scatterer are derived without introducing the effective current as Yang and Liou (1996a) did.

Inserting Eq.(2.2) into Eq.(2.1b) and using Eq.(2.3a), we have

$$\nabla \times \vec{H}(x,y,z) = \omega(\epsilon_i - i\epsilon_r)\vec{E}(x,y,z). \tag{2.4}$$

Multiplying Eq. (2.4) with $exp(-i\omega t)$ and using Eqs. (2.2) and (2.3a), we obtain

$$\nabla \times \vec{H}(x,y,z,t) = \omega\epsilon_i \vec{E}(x,y,z,t) + \epsilon_r \frac{\partial \vec{E}(x,y,z,t)}{\partial t}. \tag{2.5}$$

Eq.(2.5) can be further simplified to

$$\frac{\partial[exp(\tau t)\vec{E}(x,y,z,t)]}{\partial t} = \frac{exp(\tau t)}{\epsilon_r} \nabla \times \vec{H}(x,y,z,t). \tag{2.6}$$

where $\tau = \omega\epsilon_i/\epsilon_r$. Using the central finite-difference approximation for the temporal derivatives in Eq. (2.6) over the time interval $[n\Delta t, (n+1)\Delta t]$, we have

$$\vec{E}^{n+1}(x,y,z) = exp(-\tau\Delta t)\vec{E}^{n}(x,y,z) + exp(-\tau\Delta t/2)\frac{\Delta t}{\epsilon_r} \nabla \times \vec{H}^{n+1/2}(x,y,z), \tag{2.7a}$$

where Δt is the time increment, n is an integer denoting the time step. From Eq.(2.7a). the electric and magnetic fields are evaluated at alternate half-time steps (Yee 1966).

By discretizing Eq. (2.1a) over the time interval of $[(n-1/2)\Delta t, (n+1/2)\Delta t]$, which is a half-time step earlier than the time step when the electric field is evaluated, we have

$$\vec{H}^{n+1/2}(x,y,z) = \vec{H}^{n-1/2}(x,y,z) - \frac{\Delta t}{\mu} \bigtriangledown \times \vec{E}^{n}(x,y,z). \tag{2.7b}$$

Let $\Delta s = \Delta x = \Delta y = \Delta z$ denote the space increment; the explicit finite difference approximation of Eq. (2.7) can be derived in the following forms:

$$\begin{aligned} H_x^{n+1/2}(i,j+1/2,k+1/2) &= H_x^{n-1/2}(i,j+1/2,k+1/2) \\ &+ \frac{\Delta t}{\mu(i,j+1/2,k+1/2)\Delta s}[E_y^n(i,j+1/2,k+1) - E_y^n(i,j+1/2,k) \\ &+ E_z^n(i,j,k+1/2) - E_z^n(i,j+1,k+1/2)]. \end{aligned} \tag{2.8a}$$

$$\begin{aligned} E_x^{n+1}(i+1/2,j,k) &= exp[-\tau(i+1/2,j,k)\Delta t]E_x^n(i+1/2,j,k) + \\ exp[-\tau(i+1/2,j,k)\Delta t/2]&\frac{\Delta t}{\epsilon_r(i+1/2,j,k)\Delta s}[H_z^{n+1/2}(i+1/2,j+1/2,k) - \\ H_z^{n+1/2}(i+1/2,j-1/2,k) &+ H_y^{n+1/2}(i+1/2,j,k-1/2) - H_y^{n+1/2}(i+1/2,j,k+1/2)]. \end{aligned} \tag{2.8b}$$

The positions of the field components are illustrated in Fig. 2.1.

To obtain accurate numerical results, the spatial increment Δs must be much smaller than the wavelength within the scatterer and its minimum dimension. To guarantee the stability of the FDTD computation, the time increment Δt has to satisfy the following condition (Taflove and Brodwin 1975)

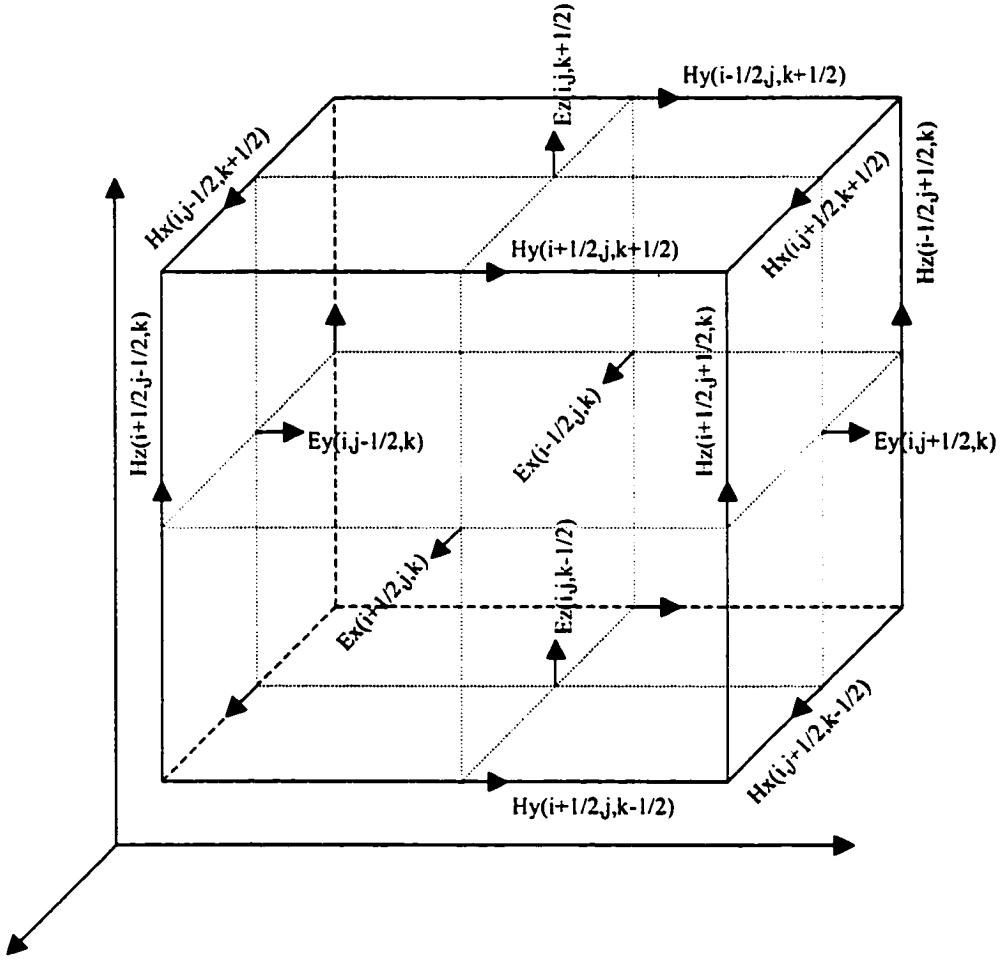

Figure 2.1: Positions of the electric and magnetic field components in an elementary cubic cell of the FDTD lattice.

$$c\Delta t \leq (\frac{1}{\Delta x^2} + \frac{1}{\Delta y^2} + \frac{1}{\Delta z^2})^{-1/2} \tag{2.9}$$

where c is the wave velocity within the scatterer.

2.2.2 Perfectly matched layer absorbing boundary condition

One major difficulty encountered in applying the FDTD method to open-structure problem is that the domain where the field is computed is unbounded. Since a finite-difference scheme over an infinite domain is impractical, the extent of the solution region must be limited by using an artificial absorbing boundary condition (ABC) (Sullivan 1996). The accuracy and stability of the FDTD program would be sensitive to the boundary condition used. Early approaches for the boundary condition are mostly one-way wave equation approximation techniques (Engquist and Majda 1971). Among those are Mur's second- and third-order ABC (Mur 1981), outgoing wave annihilators (Bayliss and Turkel 1980), transmitting boundary conditions (Liao *et al.* 1984), and the Higdon method (Higdon 1986). A recent development in ABCs was the perfectly matched layer (PML) absorbing boundary condition (ABC)(Berenger 1994,1996; Katz *et al.* 1994). In the 2D case (Berenger 1994), it is reported that reflection coefficients of PML are as low as 1/3000th of those based on standard second- and third-order analytical ABC. The PML for the 3D works just as well as in 2D (Katz *et al.* 1994).

To apply the FDTD method with PML ABC to a three-dimensional light scattering problem, the original finite difference algorithm developed by Yee (1966) needs to be modified. Following Berenger (1996) and Katz *et al.* (1994), the normal FDTD computational space is surrounded by PML regions as shown in Fig. 2.2, backed up by perfectly conducting walls. The PML creates a fictitious absorbing layer adjacent to the outer grid boundary. In the inner volume, the finite-difference equations are the usual discretizations of Maxwell's equations. In the PML regions, six Cartesian components of electric and magnetic vectors are split into twelve (e.g, H_x is split into

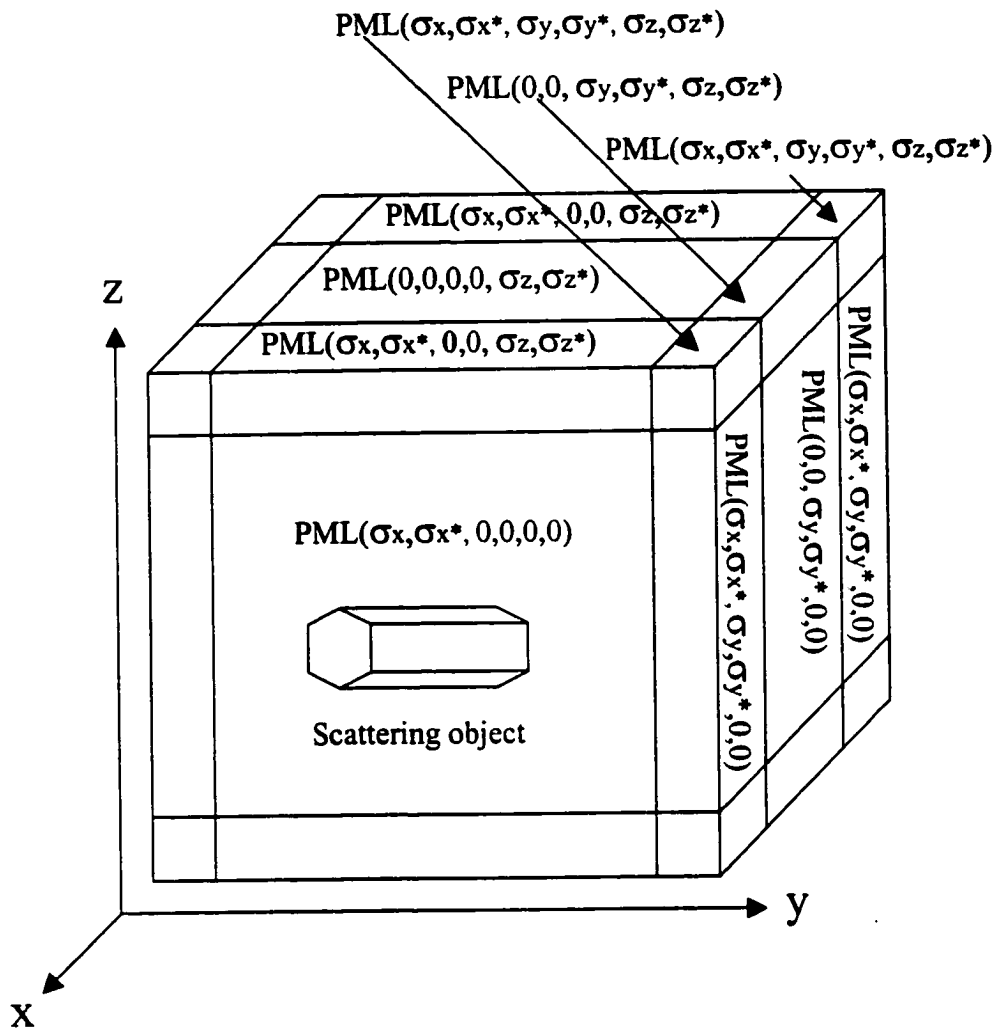

Figure 2.2: Computational domain terminated by the PML. The arrangement of the fictitious electric conductivity (σ) and magnetic conductivity (σ^*) in the PML walls is also shown.

H_{xy} and H_{xz}, and E_x is split into E_{xy} and E_{xz}), resulting in 12 modified Maxwell's equations such as

$$\mu_0 \frac{\partial H_{xy}}{\partial t} + \sigma_y^* H_{xy} = -\frac{\partial (E_{zx} + E_{zy})}{\partial y}, \tag{2.10a}$$

$$\mu_0 \frac{\partial H_{xz}}{\partial t} + \sigma_z^* H_{xz} = \frac{\partial (E_{yx} + E_{yz})}{\partial z}, \tag{2.10b}$$

$$\epsilon_0 \frac{\partial E_{xy}}{\partial t} + \sigma_y E_{xy} = \frac{\partial (H_{zx} + H_{zy})}{\partial y}, \tag{2.10c}$$

$$\epsilon_0 \frac{\partial E_{xz}}{\partial t} + \sigma_z E_{xz} = -\frac{\partial (H_{yx} + H_{yz})}{\partial z}, \tag{2.10d}$$

where the subscript 0 denotes the vacuum medium, and σ and σ^* are the fictitious electric and magnetic conductivities, respectively, which satisfy the condition

$$\frac{\sigma}{\epsilon_0} = \frac{\sigma^*}{\mu_0}. \tag{2.11}$$

Eq.(2.11) allows the impedance of the fictitious medium equal to that of free space and thus no reflection occurs when a plane wave propagates across a vacuum-PML interface.

On the six sides of the PML regions, the absorbing PML layers are matched to each other by having transverse conductivity equal to zero. As a result, the outgoing waves from the inner vacuum would propagate into these absorbing layers without reflection. At the 12 edges, two conductivities equal to zero, but the other four equal to those of the adjacent side PMLs. Thus, there is also no reflection from the side-edge interfaces. In the eight corners of the PML, the conductivities are assigned to those of the adjacent edges; none of the 12 conductivities is zero. Therefore, the reflection equals zero from all the edge-corner interfaces. The arrangement of fictitious conductivities in the PML is shown in Fig. 2.2. In theory, only the ideal continuous PML media can have perfect match without reflections. In the numerical PML, due

to step-type variations of conductivities between the PML sublayers and the break of the fields, a certain amount of numerical reflection and dispersion would occur. In order to reduce this reflection and dispersion, the conductivities should increase smoothly from a small value on the vacuum-PML interfaces to a large value on the outer boundaries. Thus, to approximate a continuous media, the number of PML cells used should be sufficient to approximate a continuous media.

After crossing the PML layer, the wave is reflected by the perfectly conducting conditions which ends the PML region; and then, after a second crossing, it can come back into the normal FDTD computational space. So, for a PML layer of thickness d, an apparent reflection factor is found to be (Berenger 1994)

$$R(\theta) = exp[-\frac{2cos\theta}{\epsilon_0 c}\int_0^d \sigma(\rho)d\rho], \tag{2.12}$$

where θ is the angle of incident radiation relative to the normal direction of the PML surface.

Berenger (1994) proposes that the conductivities should increase with depth within PML as

$$\sigma(\rho) = \sigma_m(\frac{\rho}{d})^n. \tag{2.13}$$

where n can be 1, 2 or 3 etc, but not necessarily an integer. In this study, we set n = 3. From Eqs. (2.12) and (2.13), the apparent reflection can be expressed as

$$R(\theta) = [R(0)]^{cos(\theta)}, \tag{2.14}$$

where $R(0)$ is the reflection factor at normal incidence. $R(0)$ is a key user-defined parameter which can be expressed as

$$R(0) = exp(-\frac{2}{n+1}\frac{\sigma_m d}{\epsilon_0 c}). \tag{2.15}$$

For grazing incidence, θ is close to $\pi/2$ and then the factor $R(\theta)$ is close to unity with any given σ. So the grazing incidence may cause some numerical reflections. Therefore, the scatterer and the PML should not be too close so that there will not be scattered waves impinging on the PML at grazing angles. Furthermore, Eq.(2.15) suggests that the PML should have a sufficient thickness, or enough number of cells, to achieve small reflections, which is another important reason why the number of PML layers needs to be kept at a reasonable level.

The finite-difference formulation of the 12 modified Maxwell's equations in the PML is straightforward. For instance, using the notations of the FDTD scheme, E_{xy} in the PML is computed based on Eq.(2.10c) as

$$E_{xy}^{n+1}(i+1/2,j,k) = exp[-\sigma_y(i+1/2,j,k)\Delta t/\epsilon_0]E_{xy}^{n}(i+1/2,j,k)+ \frac{1-exp[-\sigma_y(i+1/2,j,k)\Delta t/\epsilon_0]}{\sigma_y(i+1/2,j,k)\Delta y}[H_z^{n+1/2}(i+1/2,j+1/2,k)- H_z^{n+1/2}(i+1/2,j-1/2,k)], \tag{2.16}$$

where H_z equals the sum of H_{zx} and H_{zy} in the PML. In this study, H_z, as well as other electric and magnetic field components, is defined in the whole computational domain including the PML, but all the split field components such as H_{zx} and H_{zy} are defined only in the PML region. This treatment requires a little more memory than Berenger's original notations (Berenger 1996). However, this modification circumvents the complicated treatments to connect the field components at the interface between the PML and the normal FDTD computational space, which makes the program much more concise and readable.

The PML scheme has been successfully extended to the TLM-based FDTD method (Xu *et al.* 1997) and for the absorption of nonlinear electromagnetic waves (Xu *et al.* 1998). The reflection factor has been found to be better than 10^{-6} with 16 PML layers even in nonlinear cases.

2.2.3 Wave source implementation

Based on the equivalence theorem (Schelkunoff 1943; Merewether *et al.* 1980), we implement a plane wave source using the closed surface of a rectangular box within the vacuum region of the computational domain. The equivalence theorem states that the existence of wave-excitation source can be replaced by the equivalent electric and magnetic currents on the closed surface. If there is a scatterer inside this closed surface, the interior fields will be the total fields (incident and scattered), and the fields outside are just the scattered fields. By using scattered fields in this way, the field incident on the absorbing boundary condition is more readily absorbed. On the closed surface, both electric and magnetic sources are added to the fields as

$$\vec{H} \leftarrow \vec{H} - \frac{\Delta t}{\mu_0 \Delta s}(\vec{E}^{in} \times \hat{n}), \tag{2.17a}$$

$$\vec{E} \leftarrow \vec{E} - \frac{\Delta t}{\epsilon_0 \Delta s}(\hat{n} \times \vec{H}^{in}), \tag{2.17b}$$

where $\vec{H}^{in}$ and $\vec{E}^{in}$ are the incident fields, and $\hat{n}$ is the inward unit normal vector of the closed surface. For the numerical implementation, note that the nodes of $\vec{E}$ and $\vec{H}$ are at different spatial grid points. Furthermore, $\vec{H}^{in}$ and $\vec{E}^{in}$ may come from arbitrary directions. Therefore, the light scattering by an arbitrarily oriented particle can be computed. To obtain the incident fields $\vec{H}^{in}$ and $\vec{E}^{in}$ at the corresponding grid points on the closed surface, an auxiliary one-dimensional source FDTD grid is placed along the incident direction (Taflove 1995). At only one single point on the one-dimensional source grid, an arbitrary field excitation is added to the electric field components. Herein, a Gaussian pulse is used as the field excitation in the form

$$E(t) = exp[-(\frac{t}{30\Delta t} - 5)^2]. \tag{2.18}$$

In the time-marching of the FDTD formulation, the pulse propagates along the one-dimensional source FDTD grid. The incident field components at each grid point

on the closed surface is from a linear interpolation of the neighboring field values on the one-dimensional source grid. This process is exactly like the propagation of a plane wave to the grid points on the closed surface, and then the wave front on the closed surface is used to simulate the incident wave only inside the closed surface. This is called the total-field formulations. By comparing the total-field formulations with the scattered-field formulations in which only the scattered-field is computed throughout the computational domain, Holland and Williams (1983) found that, in terms of numerical dispersion, the total-field FDTD approach is superior to the scattered-field approach.

It has been assumed here that the medium surrounding the scatterer is free space and we then use the equivalence theorem for the implementation of the wave source on the closed surface. In general, the equivalence theorem can also be applied when the surrounding medium is an arbitrary dielectric medium. However, when the surrounding medium is not free space, both Eq.(2.17) and the one-dimensional FDTD formulation for the incident plane wave must be modified. We give the detailed discussion about the wave source implementation in general situations in Chapter 4.

2.2.4 Transformation of the near field to the far field

The near fields computed by the FDTD algorithm are in the time domain. To calculate the single scattering properties of the dielectric scatterer, the time-dependent fields must be transformed to the corresponding fields in the frequency domain. In this study, the discrete Fourier transform (DFT) is used to do this. Let Δt denote the time increment, n denote the time step, and $f(n\Delta t)$ be a component of the field in the time domain at the time step n. The field in the frequency domain is then given by

$$F(\omega) = \sum_{n=0}^{N} f(n\Delta t) exp(i\omega n\Delta t), \tag{2.19}$$

where N denotes the total time-marching steps.

In order to calculate the single scattering properties of a dielectric particle, we also need to transform the near-field in the frequency domain to the far-field (Yee *et al.* 1991; Luebbers *et al.* 1991; Barth *et al.* 1992). For a lossless particle, the equivalent electric and magnetic currents can be defined on a surface enclosing the particle, using the electromagnetic equivalence theorem; the far-field can then be obtained through these currents. However, for an absorptive particle, this approach is not numerically efficient. In this study, we use a volume integration method (Purcell and Pennypacker 1973; Goedecke and O'Brien 1988; Flatau *et al.* 1990; Draine and Flatau 1994; Yang and Liou 1996a) to evaluate the scattered far-field and the absorption cross-section.

For a dielectric medium, the electromagnetic wave equation in the frequency domain can be expressed in the source-dependent form as (Goedecke and O'Brien 1988)

$$(\nabla^2 + k^2)\vec{E}(\vec{r}) = -4\pi(k^2\vec{\mathbf{I}} + \nabla\nabla).\vec{P}(\vec{r}). \tag{2.20}$$

where $\vec{\mathbf{I}}$ is a unit dyad (Tai 1971) and $\vec{P}(\vec{r})$ is the polarization vector given by

$$\vec{P}(\vec{r}) = \frac{\epsilon(\vec{r}) - 1}{4\pi}\vec{E}(\vec{r}). \tag{2.21}$$

When the surrounding medium is air or free space, $\vec{P}(\vec{r})$ is nonzero only within the particle. The solution for Eq.(2.20) is given by an integral equation in the form (Tai 1971)

$$\vec{E}(\vec{r}) = \vec{E}_0(\vec{r}) + 4\pi \int\int\int_v G(\vec{r},\vec{\xi})(k^2\vec{\mathbf{I}} + \nabla_\xi\nabla_\xi).\vec{P}(\vec{\xi})d^3\xi, \tag{2.22}$$

where $\vec{E}_0(\vec{r})$ denotes the incident wave; the integration domain v is the region inside the dielectric particle; the 3-D Green function in free space, $G(\vec{r}.\vec{\xi})$, is given by

$$G(\vec{r},\vec{\xi}) = \frac{exp(ik|\vec{r}-\vec{\xi}|)}{4\pi|\vec{r}-\vec{\xi}|}. \tag{2.23}$$

In the far-field region ($kr \rightarrow \infty$), it can be proven by using Eq.(2.22) that the scattered far-field caused by the presence of a dielectric scatterer is (Yang and Liou 1996a)

$$\vec{E}_s(\vec{r})|_{kr\rightarrow\infty} = \frac{k^2 e^{ikr}}{4\pi r} \int\int\int_v [\epsilon(\vec{\xi}) - 1]\{\vec{E}(\vec{\xi}) - \hat{r}[\hat{r}.\vec{E}(\vec{\xi})]\} exp(-ik\hat{r}.\vec{\xi}) d^3\xi, \quad (2.24)$$

where $\hat{r}=\vec{r}/|\vec{r}|$ is the unit vector in the observation direction (see Fig. 2.3), and $\vec{\xi}$ is the position vector which represents (x,y,z). The scattered field $\vec{E}_s(\vec{r})$ can be broken down into the components parallel and perpendicular to the scattering plane in the form

$$\vec{E}_s(\vec{r}) = \hat{\alpha} E_{s,\alpha}(\vec{r}) + \hat{\beta} E_{s,\beta}(\vec{r}), \quad (2.25)$$

where $\hat{\alpha}$ and $\hat{\beta}$ are the unit vectors parallel and perpendicular to the scattering plane respectively, and

$$\hat{r} = \hat{\beta} \times \hat{\alpha}. \quad (2.26)$$

Therefore Eq.(2.24) can be written in a matrix form

$$\begin{bmatrix} E_{s,\alpha}(\vec{r}) \\ E_{s,\beta}(\vec{r}) \end{bmatrix} = \frac{k^2 exp(ikr)}{4\pi r} \int\int\int_v [\epsilon(\vec{\xi}) - 1] \begin{bmatrix} \hat{\alpha}.\vec{E}(\vec{\xi}) \\ \hat{\beta}.\vec{E}(\vec{\xi}) \end{bmatrix} exp(-ik\hat{r}.\vec{\xi}) d^3\xi$$

$$= \frac{exp(ikr)}{-ikr} \begin{bmatrix} s_2 & s_3 \\ s_4 & s_1 \end{bmatrix} \begin{bmatrix} E_{o,\alpha} \\ E_{o,\beta} \end{bmatrix}. \quad (2.27)$$

where s_i ($i = 1, 2, 3$ and 4) are the elements of the amplitude scattering matrix. s_1, s_2, s_3 and s_4 are defined in a sequence shown in Eq.(2.27) to make s_1 and s_3 associated with the incident E components perpendicular to the scattering plane, and to make

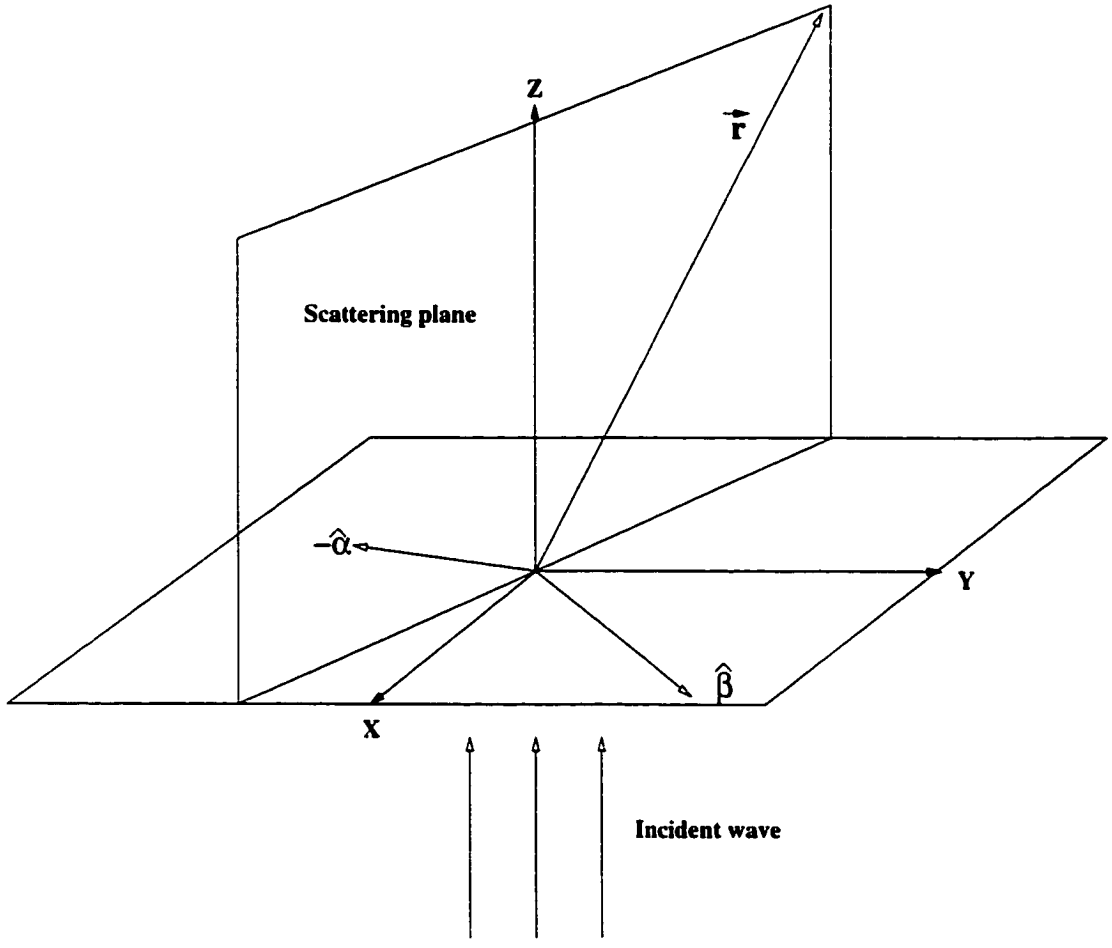

Figure 2.3: Incident and scattering geometry for the transformation of the near field to far field.

s_2 and s_4 associated with the incident E components parallel to the scattering plane. $E_{o,\alpha}$ and $E_{o,\beta}$ are the components of the incident E-field with respect to the scattering plane. Note here that if the incident wave is in the z direction as shown in Fig. 2.3, both $E_{o,\alpha}$ and $E_{o,\beta}$ are in the xoy plane with $E_{o,\beta}$ perpendicular and $E_{o,\alpha}$ parallel to the scattering plane. In the FDTD scheme the incident wave is defined by given $E_{o,x}$ and $E_{o,y}$, which denote the incident E-field components in x and y directions, respectively. Therefore, it is clear that

$$\begin{bmatrix} E_{o,\alpha} \\ E_{o,\beta} \end{bmatrix} = \begin{bmatrix} \hat{\beta}.\hat{x} & -\hat{\beta}.\hat{y} \\ -\hat{\beta}.\hat{y} & \hat{\beta}.\hat{x} \end{bmatrix} \begin{bmatrix} E_{o,x} \\ E_{o,y} \end{bmatrix}, \tag{2.28}$$

where $\hat{x}$ and $\hat{y}$ are unit vectors along the x and y axes, respectively. The amplitude scattering matrix can then be expressed as

$$\begin{bmatrix} s_2 & s_3 \\ s_4 & s_1 \end{bmatrix} = \begin{bmatrix} F_{\alpha,y} & F_{\alpha,x} \\ F_{\beta,y} & F_{\beta,x} \end{bmatrix} \begin{bmatrix} \hat{\beta}.\hat{x} & \hat{\beta}.\hat{y} \\ -\hat{\beta}.\hat{y} & \hat{\beta}.\hat{x} \end{bmatrix}. \tag{2.29}$$

where $F_{\alpha,x}$, $F_{\alpha,y}$, $F_{\beta,x}$ and $F_{\beta,y}$ are computed from the electric fields obtained by the FDTD in two polarization directions. If we assume the incident E-field amplitude is one,

(1) when $E_{o,x} = 1$ and $E_{o,y} = 0$, we have

$$\begin{bmatrix} F_{\alpha,x} \\ E_{\beta,x} \end{bmatrix} = \frac{ik^3}{4\pi} \int\int\int_v [1 - \epsilon(\vec{\xi})] \begin{bmatrix} \hat{\alpha}.\vec{E}(\vec{\xi}) \\ \hat{\beta}.\vec{E}(\vec{\xi}) \end{bmatrix} exp(-ik\hat{r}.\vec{\xi}) d^3\xi; \tag{2.30a}$$

(2) when $E_{o,x} = 0$ and $E_{o,y} = 1$, we have

$$\begin{bmatrix} F_{\alpha,y} \\ F_{\beta,y} \end{bmatrix} = \frac{ik^3}{4\pi} \int\int\int_v [1 - \epsilon(\vec{\xi})] \begin{bmatrix} \hat{\alpha}.\vec{E}(\vec{\xi}) \\ \hat{\beta}.\vec{E}(\vec{\xi}) \end{bmatrix} exp(-ik\hat{r}.\vec{\xi}) d^3\xi. \tag{2.30b}$$

Moreover, in terms of the Stokes parameters, we have

$$\begin{bmatrix} I \\ Q \\ U \\ V \end{bmatrix} = \frac{\mathbf{F}}{k^2 r^2} \begin{bmatrix} I_0 \\ Q_0 \\ U_0 \\ V_0 \end{bmatrix}, \tag{2.31}$$

where the subscript 0 denotes the incident wave. The transformation matrix is given by

$$\mathbf{F} = \begin{bmatrix} F_{11} & F_{12} & F_{13} & F_{14} \\ F_{21} & F_{22} & F_{23} & F_{24} \\ F_{31} & F_{32} & F_{33} & F_{34} \\ F_{41} & F_{42} & F_{43} & F_{44} \end{bmatrix}. \tag{2.32}$$

The elements of $\mathbf{F}$ are simply functions of s_i; they can be derived from the definition of Stokes parameters in terms of the electric fields, and are given by (Bohren and Huffman 1983)

$$F_{11} = \frac{1}{2}(s_1 s_1^* + s_2 s_2^* + s_3 s_3^* + s_4 s_4^*), \tag{2.33a}$$

$$F_{12} = \frac{1}{2}(s_2 s_2^* - s_1 s_1^* + s_4 s_4^* - s_3 s_3^*), \tag{2.33b}$$

$$F_{13} = Re(s_2 s_3^* + s_1 s_4^*), \tag{2.33c}$$

$$F_{14} = Im(s_2 s_3^* - s_1 s_4^*), \tag{2.33d}$$

$$F_{21} = \frac{1}{2}(s_2 s_2^* - s_1 s_1^* + s_3 s_3^* - s_4 s_4^*), \tag{2.33e}$$

$$F_{22} = \frac{1}{2}(s_1 s_1^* + s_2 s_2^* - s_3 s_3^* - s_4 s_4^*), \tag{2.33f}$$

$$F_{23} = Re(s_2 s_3^* - s_1 s_4^*), \tag{2.33g}$$

$$F_{24} = Im(s_2 s_3^* + s_1 s_4^*), \tag{2.33h}$$

$$F_{31} = Re(s_2 s_4^* + s_1 s_3^*), \tag{2.33i}$$

$$F_{32} = Re(s_2 s_4^* - s_1 s_3^*), \tag{2.33j}$$

$$F_{33} = Re(s_1 s_2^* + s_3 s_4^*), \tag{2.33k}$$

$$F_{34} = Im(s_2 s_1^* + s_4 s_3^*), \tag{2.33l}$$

$$F_{41} = Im(s_4 s_2^* + s_1 s_3^*), \tag{2.33m}$$

$$F_{42} = Im(s_4 s_2^* - s_1 s_3^*), \tag{2.33n}$$

$$F_{43} = Im(s_1 s_2^* - s_3 s_4^*), \tag{2.33o}$$

$$F_{44} = Re(s_1 s_2^* - s_3 s_4^*). \tag{2.33p}$$

The scattering cross-section is related to the first element of the scattering transformation matrix as follows

$$\sigma_s = \frac{1}{k^2} \int_0^{2\pi} \int_0^{\pi} F_{11} sin\theta d\theta d\varphi, \tag{2.34}$$

where θ is the scattering angle (zenith angle) and φ is the azimuth angle.

The scattering phase matrix **P** can be defined in terms of the transformation matrix as follows

$$\mathbf{P} = \frac{4\pi}{\sigma_s k^2}\mathbf{F}. \tag{2.35}$$

With a specific orientation, the scattering characteristics of nonspherical particles depend not only on the zenith angle (scattering angle) but also on the azimuth angle with respect to the scattering direction. The results should be azimuthally averaged and this is done to any element of **P** through

$$P(\theta) = \frac{1}{2\pi}\int_0^{2\pi} P(\theta,\varphi)d\varphi. \tag{2.36}$$

The asymmetry factor then can be numerically computed by

$$g = \frac{1}{2}\int_0^{\pi} P_{11}(\theta)cos\theta sin\theta d\theta. \tag{2.37}$$

The absorption cross-section is also calculated using the volume integration (Yang and Liou 1996a) in the form

$$\sigma_a = \frac{k}{|\vec{E}_0|^2}\int\int\int_v \epsilon_i(\vec{\xi})\vec{E}(\vec{\xi}).E^*(\vec{\xi})d^3\xi. \tag{2.38}$$

The extinction cross-section is simply the sum of the scattering and absorption cross-sections as

$$\sigma_e = \sigma_s + \sigma_a. \tag{2.39}$$

For the scattering by a nonspherical particle, the absorption and extinction cross-sections depend on the polarization of the incident wave. However, if the average of the cross-sections with respect to the two perpendicularly polarized incident waves is considered, it is independent of the plane on which the polarization of the incident wave is defined (Yang and Liou 1996a). The cross-sections for unpolarized light can then be expressed as the mean values of the the cross-sections with respect to the two perpendicularly polarized incident waves.

2.3 Validation of the perfectly matched layer finite-difference time domain

In principle, the FDTD method can be accurately applied to particles of arbitrary shapes and composition. However, there are numerical errors involved in the FDTD technique. These errors can be attributed to the numerical dispersion of the finite-difference analog, the approximation of a specific particle shape by a pseudo-structure constructed by cubic grid cells, the representation of near-field by the discretized data which does not account for the field variation within each cell, and reflections from the PML ABC. These errors are dependent on the grid size, the cell number in the free space between the scatterer and the PML, and the cell number in the PML, etc. Yang and Liou (1996a) pointed out that the errors of the FDTD technique can also be attributed to the residual energy inside the computational domain, when the time-marching iteration of the near-field based on the pulse technique is terminated.

For a fixed PML thickness, the reducing $R(0)$ by increasing the PML loss monotonically reduces the reflection from the domain boundary. However, this benefit levels off when $R(0)$ drops to less than 10^{-5} (Katz *et al.* 1994). Berenger (1994) found that the increasing PML cell number can also reduces the reflection from the domain boundary. But the PML thickness is restricted by the size of the computational domain due to the limitation of the computing resource. Generally, a PML thickness of 4-8 cells is reasonable for both accuracy and computing efficiency. For the distance between the scatterer and the PML, 5-20 cells are sufficient (Berenger 1994). Throughout this chapter, we set a $R(0)$ of 10^{-5}, use a 6-cell thick PML, and keep 7 cells for free space between the scatterer and the PML.

It was found that by using the PML ABC, the computational domain is reduced significantly when compared with traditional ABC approaches. In this study, the computations were performed on a SunSparc workstation and Cray SV1 machines, respectively, for particles with size parameters ≤ 20 and > 20. In the following, the PML FDTD scheme for the scattering by dielectric particles are examined by using

Mie theory for spheres, and the exact scattering solution for a pair of spheres in contact.

Figure 2.4 shows the extinction efficiency (Qe) and absorption efficiency (Qa), and asymmetry factor (g) of spherical ice crystals computed by Mie theory and the PML FDTD method at a wavelength of 10.8 μm ($m = 1.0891 + 0.18216i$), which is a particularly important wavelength in satellite remote sensing. Also shown are the absolute and relative errors of the PML FDTD results. In the FDTD calculations, a grid size of $\Delta s = \lambda/20$ is used. We can see that the FDTD errors for both extinction efficiency and absorption efficiency are very small. For size parameter larger than 2.0, the relative errors for Qe are within ~1.0%, and the relative errors for Qa are within ~0.5%. The errors in asymmetry factors due to the FDTD are ~0.1%. These results are true even when size parameter reaches 40. In consideration of the trend of the error, it is safe to believe that the PML FDTD can produce Qe and Qa with errors within ~1.0% for quite large size parameters. For size parameter smaller than 2.0, the relative errors become larger for Qe, Qa and g. This is because when using $\Delta s = \lambda/20$, the sphere is approximated by only a few cubic cells (e.g., for a size parameter equals to 1.0, it has only about 6 cubic cells in diameter to approach a sphere). Numerical results show that using smaller cell size would result in more accurate results.

It should be noted here that using $\Delta s = \lambda/20$, errors due to the FDTD with the conventional boundary condition are about 5% for the extinction and absorption efficiencies at the size parameter of 10, as reported in Fig. 5 of Yang and Liou (1996a). Their errors also increase as the size parameter increases. It may be concluded that the accuracy of the FDTD method is sensitive to the boundary conditions used.

Figures 2.5 to 2.7 show the scattering phase functions for spherical ice crystals computed by Mie theory and the PML FDTD scheme using a wavelength of 10.8 μm for different size parameters. Also shown are the absolute and relative errors of the FDTD results. We can see that the errors in the scattering phase functions are typically smaller than 5%. Larger errors due to the FDTD only occur when the scattering phase functions are minimum. These errors can be largely related to the

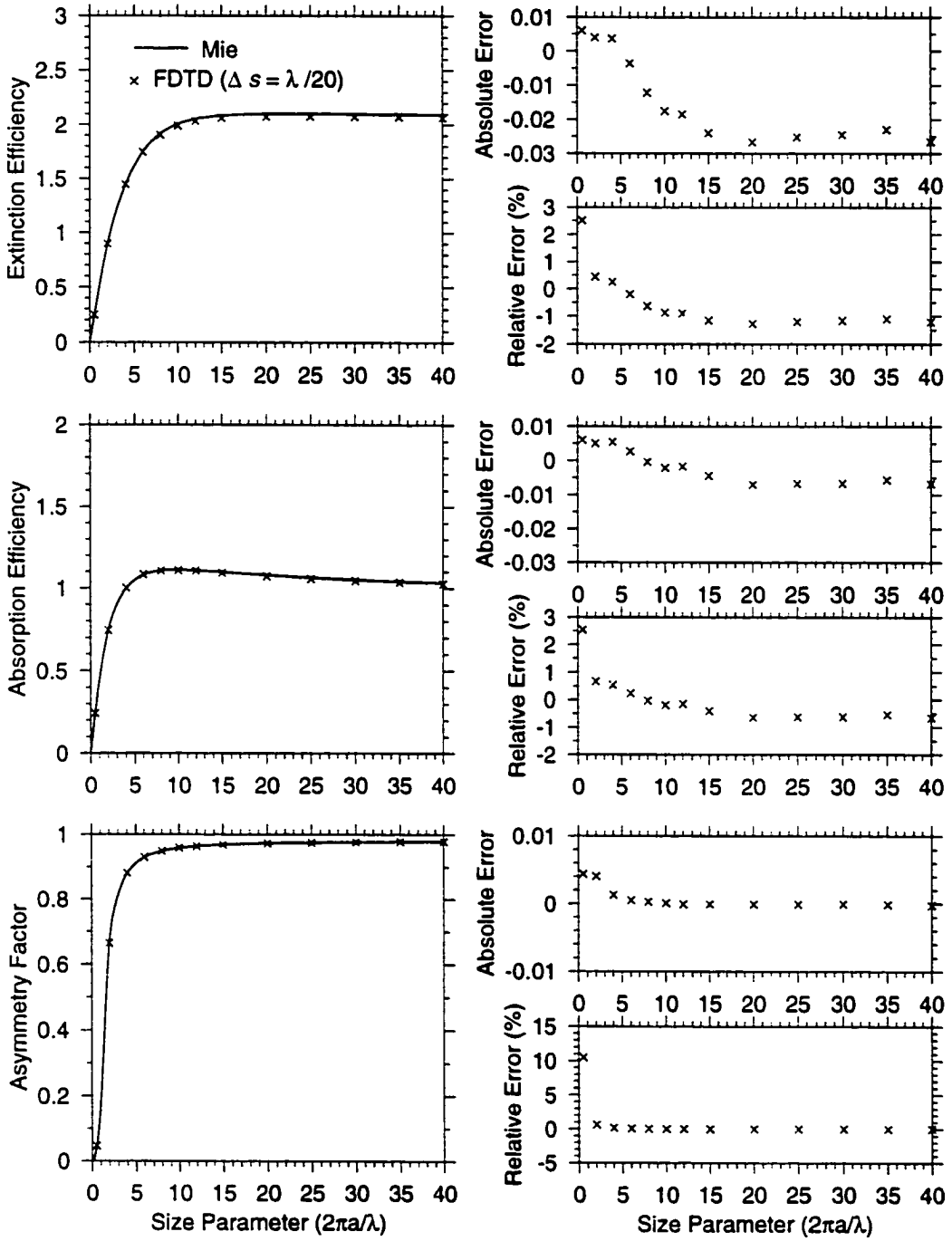

Figure 2.4: The extinction efficiency, absorption efficiency and asymmetry factor for spherical ice crystals as functions of the size parameter, $2\pi a/\lambda$. where a is the radius of the sphere and λ is the wavelength. These results are computed by Mie theory and the PML FDTD method at a wavelength of 10.8 μm ($m = 1.0891 + 0.18216i$). Also shown are the absolute and relative errors of the FDTD results. A grid size of $\Delta s = \lambda/20$ is used in the FDTD calculation.

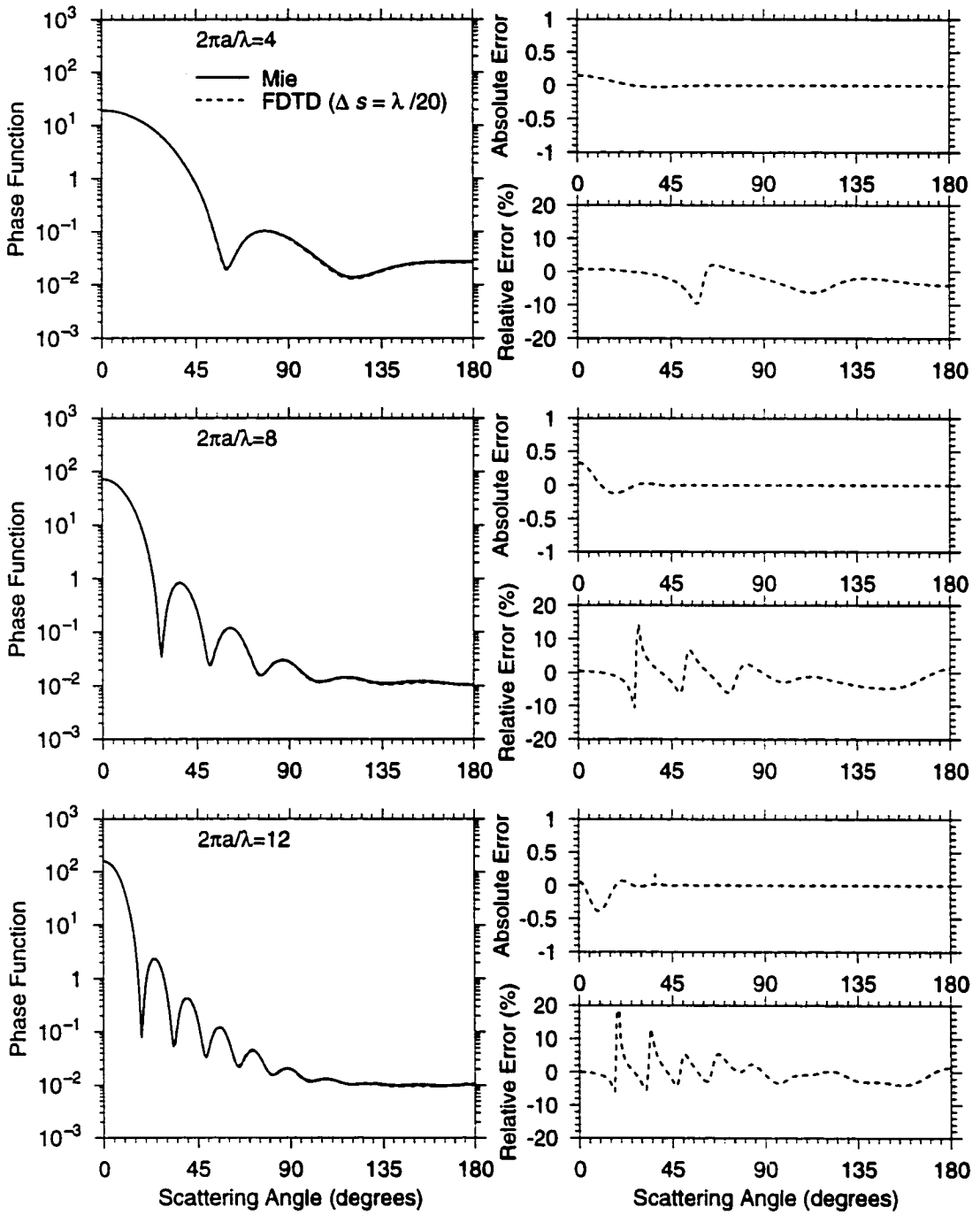

Figure 2.5: The scattering phase functions for spherical ice crystals computed by Mie theory and the PML FDTD method at a wavelength of 10.8 μm ($m = 1.0891 + 0.18216i$) for different size parameters. Also shown are the absolute and relative errors of the FDTD results. In the FDTD calculations, a cell size of $\Delta s = \lambda/20$ is used.

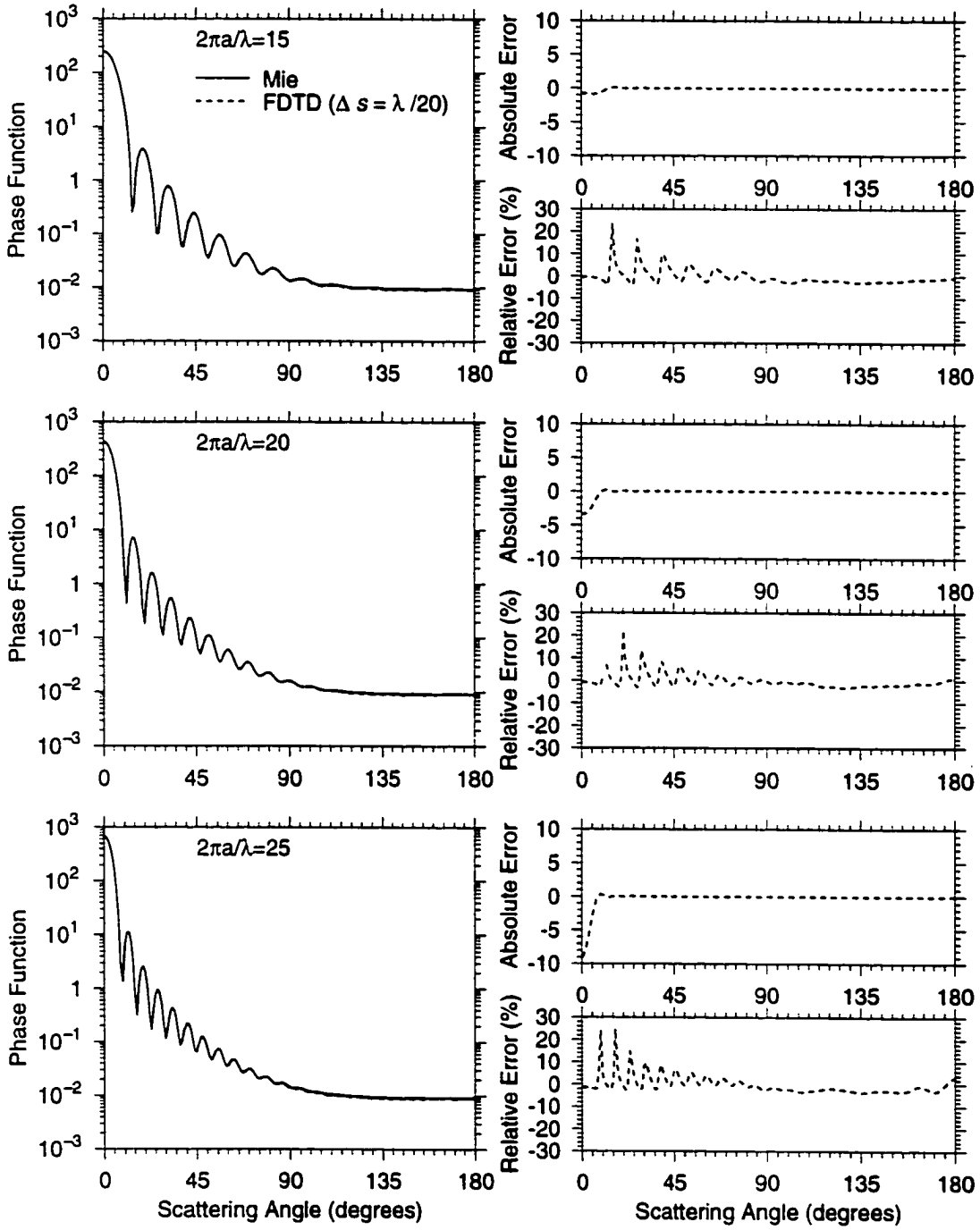

Figure 2.6: Same as Fig. 2.5 but for size parameters of 15. 20 and 25.

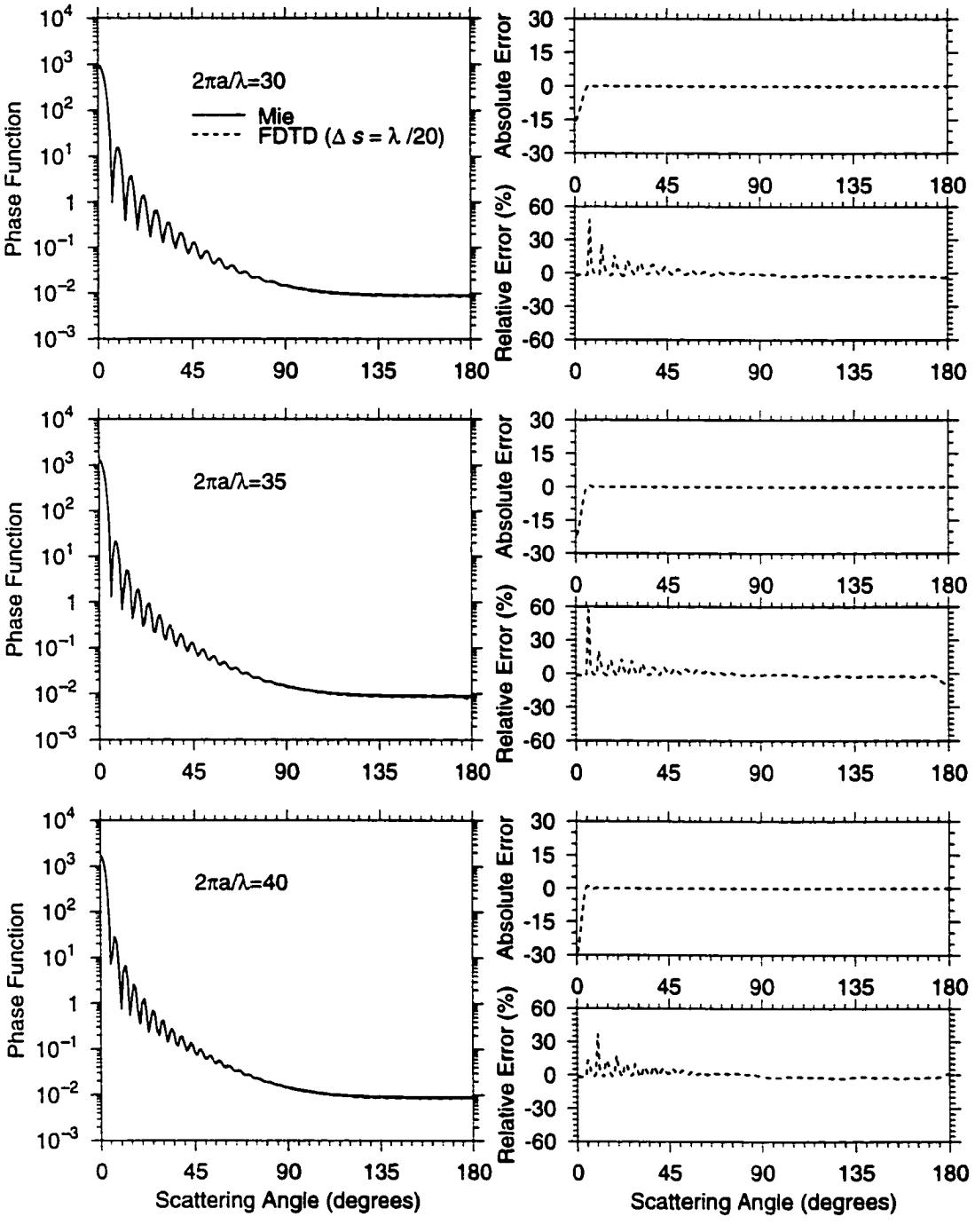

Figure 2.7: Same as Fig. 2.5 but for size parameters of 30, 35 and 40.

numerical dispersion of the finite-difference analog, and the approximation of a sphere by cubic grid cells, as well as the representation of near-field by the discretized data. To reduce the errors, finer cells should be used, but larger CPU time and storage space are required.

Figure 2.8 shows the scattering phase functions for spherical ice crystals computed by Mie theory and the PML FDTD method at wavelengths of $0.55\mu m$ ($m = 1.311$), 10.8 μm ($m = 1.0891 + 0.18216i$) and 12.99 μm ($m = 1.4717 + 0.3890i$) for a size parameter of 6. We choose the three wavelengths to demonstrate the effectiveness of the PML FDTD to different refractive indices of ice. In order to see how the use of smaller cells affects accuracy, we use three different cell sizes of $\lambda/20$, $\lambda/30$ and $\lambda/60$ in the PML FDTD calculation. Also shown are the absolute and relative errors of phase functions computed by the PML FDTD. For different refractive index, we cannot see significant difference in errors. Figure 2.8 shows that the PML FDTD program is insensitive to the refractive index or the wavelength in this application. We can also see that the relative errors decrease by using higher resolution meshes for each wavelength. Using $\Delta s = \lambda/60$, the relative errors in the scattering phase function are smaller than ~4%.

The exact solution of light scattering by a double sphere system is available using the multipole method (Videen *et al.* 1996). Figure 2.9 shows a comparison of the scattering phase functions from a pair of spheres ($r = \lambda/2$ for each sphere) in contact, illuminated end-on. The PML FDTD program was used with a cell size $\Delta s = \lambda/60$. $m = 1.53 + 0.001i$ was used to approach the refractive index of biological spores (Tuminello *et al.* 1997) at a wavelength of $0.55\mu m$. For this nonspherical double sphere system, only a small discrepancy exists between the calculated results of the two models. At the minimum value of the phase function, the relative error of the FDTD result is ~19%. However, it is noted here that the minimum value of the phase function is 2.96617×10^{-3} and the absolute error of the FDTD result is only -6.96830×10^{-4}. Therefore, the FDTD program is shown to work well for nonspherical particles as well as for spherical particles.

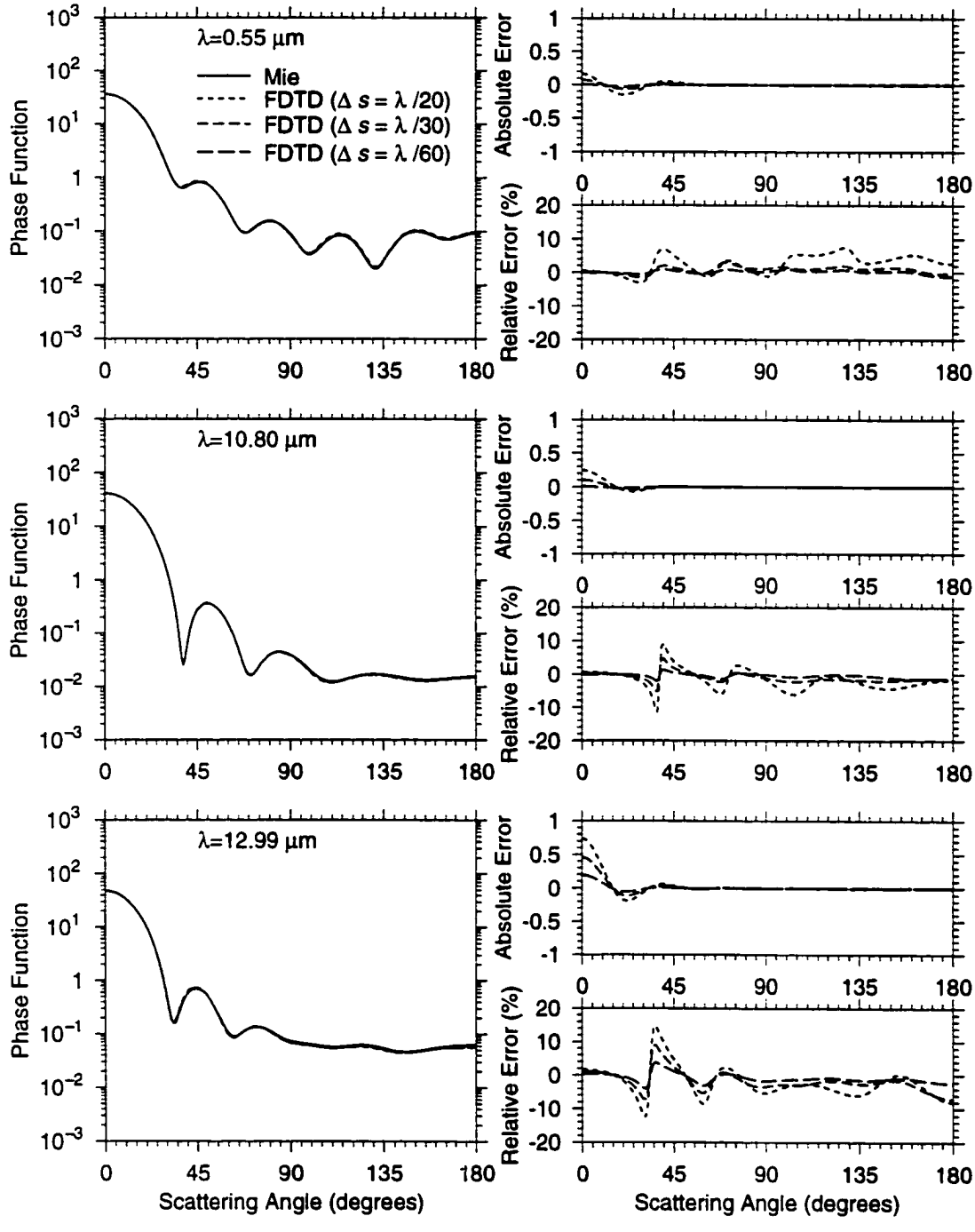

Figure 2.8: The scattering phase functions for spherical ice crystals computed by Mie theory and the PML FDTD method at wavelengths of 0.55 μm ($m = 1.311$), 10.8 μm ($m = 1.0891 + 0.18216i$), and 12.99 μm ($m = 1.4717 + 0.3890i$) for a size parameter of 6. Also shown are the absolute and relative errors of the FDTD results. Different cell sizes of $\Delta s = \lambda/20$, $\lambda/30$ and $\lambda/60$ are used in the FDTD calculations.

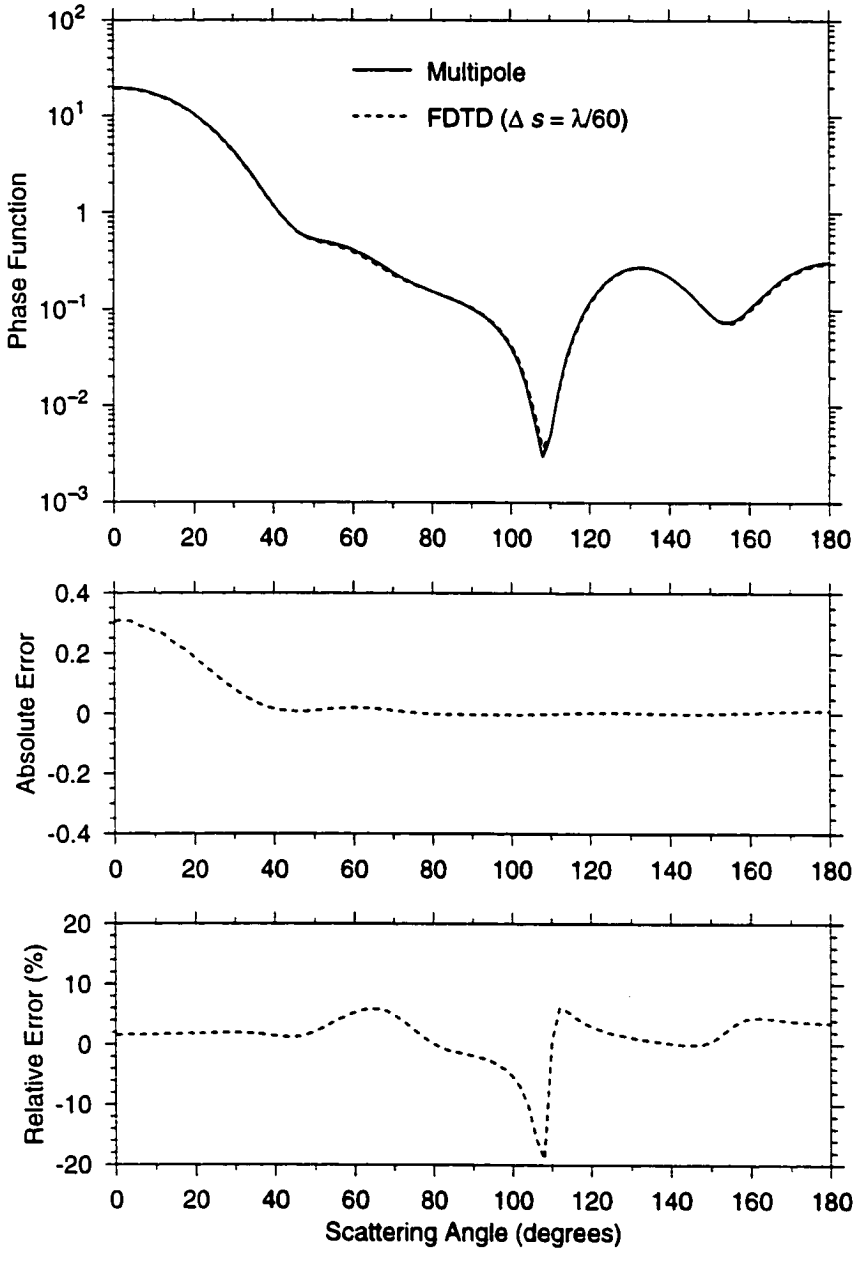

Figure 2.9: The scattering phase function for a pair of spheres ($r = \lambda/2$) in contact, illuminated end-on. The results are calculated using the multipole method and the PML FDTD program with a cell size $\Delta s = \lambda/60$. $m = 1.53 + 0.001i$ is used to represent the refractive index of biological spores at a wavelength of $0.55\mu m$. Also shown are the absolute and relative errors of the FDTD results.

2.4 Applications to nonspherical particles

2.4.1 Hexagonal ice crystals

From *in situ* aircraft observations, it has been learned that cirrus clouds are largely composed of nonspherical plates, columns, and bullet rosettes (Heymsfield and Platt 1984) with a basic hexagonal structure. The size parameter for these ice crystals can range from ~10^{-1} to 10^3 at thermal infrared wavelengths (~4 - 100 μm). This wide size parameter range introduces tremendous difficulty in the modeling of optical properties of nonspherical ice crystals (Liou and Takano 1994).

In both climate and remote sensing applications, calculations involving scattering and absorption by nonspherical ice crystals at thermal infrared wavelengths are usually highly simplified. Mie theory is often used, but nonspherical particles must first be converted into spheres (e.g., Plass and Kattawa 1968; Arnott *et al.* 1997). Other commonly used approximations include the anomalous diffraction theory (ADT) and the geometric optics method (GOM) (e.g., Takano and Liou 1989). For example, Sun and Shine (1995) applied the GOM for hexagonal ice crystals with size parameters greater than 30 and Mie theory for size parameters less than 30.

Figure 2.10 shows the absorption efficiency of randomly oriented hexagonal ice crystals as a function of size parameter at a wavelength of 12.99 μm ($m = 1.4717 + 0.389i$). The aspect ratios (length/width) for these nonspherical ice crystals roughly follow the observations reported by Ono (1969) and Auer and Veal (1970). The results are derived from different scattering algorithms: Mie theory for a sphere with an equivalent projected area, ADT, GOM, and FDTD technique. We can see that in the resonance region. Mie theory overestimates the absorption efficiency while the ADT and GOM underestimate it. The absorption efficiency from the ADT approaches one for large size parameters because the ADT does not consider the external reflection. Differences between the ADT and GOM for small size parameters can be explained by the absence of refraction and reflection in the ADT.

Based on the single scattering properties of hexagonal ice crystals derived from the

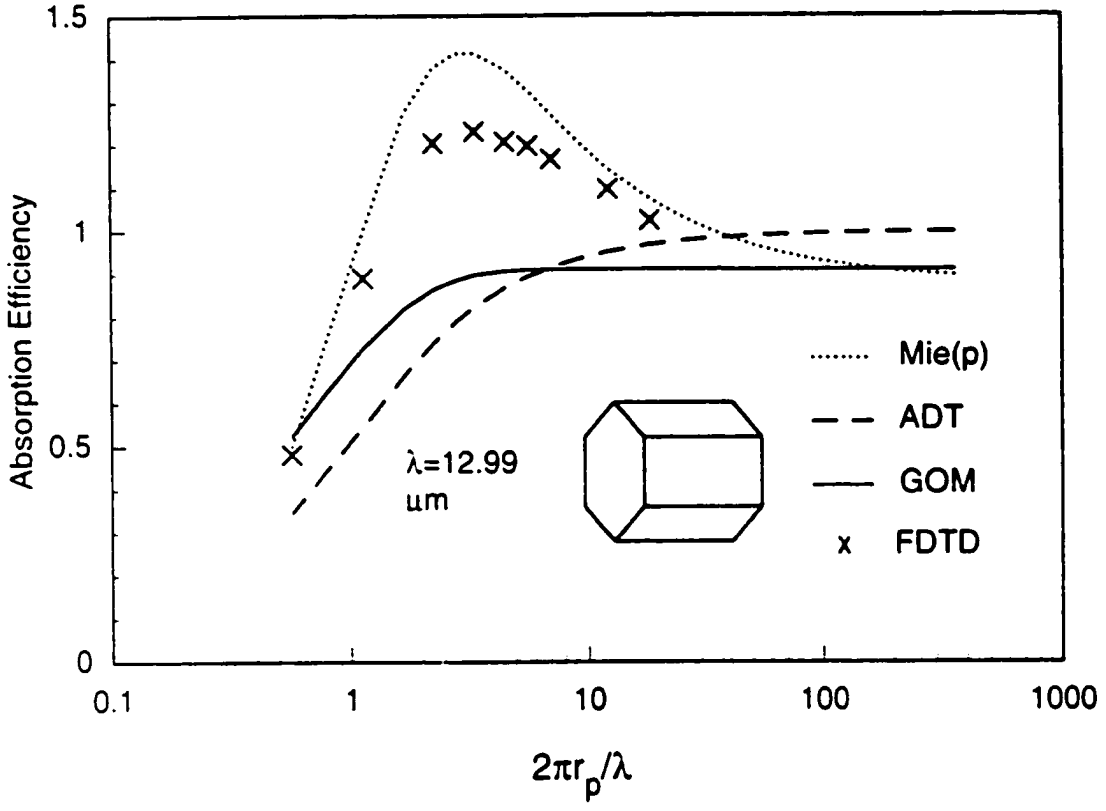

Figure 2.10: Comparison of absorption efficiency for randomly oriented hexagonal ice crystals derived from different scattering program: Mie theory for spheres with equal projected area, anomalous diffraction theory (ADT), geometric optics method (GOM), and finite-difference time domain (FDTD) technique. The results are shown as functions of size parameter $2\pi r_p/\lambda$, where r_p is the radius for a projected area equivalent sphere.

GOM for large size parameters and the FDTD technique for small size parameters, we (Fu *et al.* 1998; 1999) developed a composite scheme which appropriately interpolates results for size parameters between ~10 and ~50. Applying this composite technique, errors in the broadband emissivity of cirrus clouds associated with conventional approaches were examined (Fu *et al.* 1999). It was found that the relative errors in the emissivity due to using the approximate light scattering programs can be as large as ~30%. We have developed an accurate parameterization of the infrared radiative properties of cirrus clouds for climate models using the single-scattering properties from the composite method (Fu *et al.* 1998).

It is well known that in the resonance region, absorption efficiencies of spherical particles can be much larger than one. This is the so-called tunneling effect whereby the incident radiation outside the projected area of the particle can be absorbed. From Fig. 2.10, we can see that in the resonance region, absorption efficiencies of hexagonal particles can also be larger than one, which means that for particles whose surfaces are not smooth, the tunneling effect is still significant. The tunneling effect is clearly shown in the upper panel of Fig. 2.11, which illustrates a Poynting vector field near and inside a hexagonal ice crystal ($D/L = 1$ and $D\pi/\lambda = 2.5$, where D and L denote the width and length of the hexagonal crystal, respectively). The Poynting vector represents the flux density of electromagnetic energy and the direction of energy propagation. The results are obtained using the FDTD technique at a wavelength of 12.99 μm ($m = 1.4717 + 0.389i$). The incident radiation is perpendicular to the symmetrical axis of the particle with the electric field polarized in the z direction. The Poynting vector field on a plane perpendicular to the symmetrical axis of the particle at $L/2$ is shown. We see that photons passing near the particle edge can be captured and absorbed. When the incident electric field is polarized in y direction, as shown in the lower panel of Fig. 2.11, we can see that incident energy propagates along the surface of the particle. Therefore, for natural incident light, tunneling effect and surface wave both exist. The absorption of natural incident light is determined by the two processes.

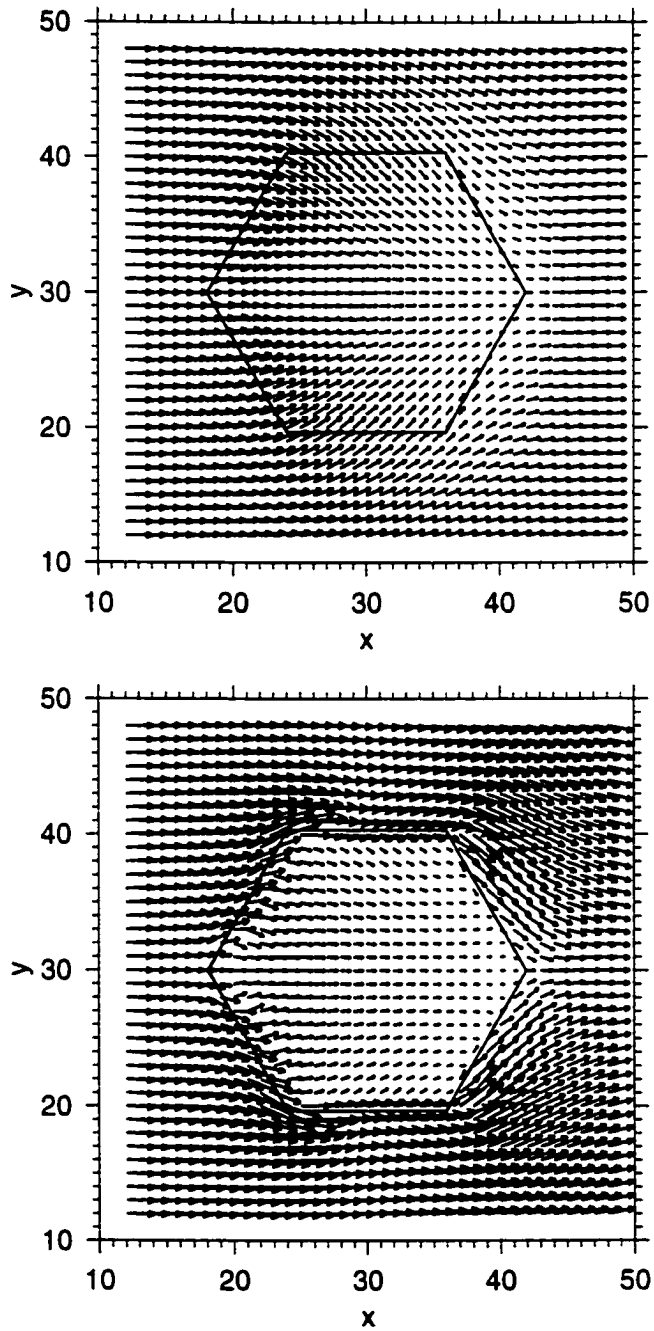

Figure 2.11: Poynting vectors near and inside a hexagonal ice crystal ($D/L = 1$ and $D\pi/\lambda = 2.5$) on a plane perpendicular to the symmetrical axis of the particle at $L/2$. A wavelength of 12.99 μm ($m = 1.4717 + 0.389i$) is used. For the upper panel, the incident electric field is polarized in z-direction; for the lower panel, the incident electric field is polarized in y-direction.

What we learn from Figs.(2.10) and (2.11) are quite different from what Mitchell (1995) assumed for nonspherical particles. Mitchell (1995) claimed that the light scattering and absorption by nonspherical particles are very different from those by spheres and should be simulated more appropriately by the ADT method. Here we can conclude that the ADT neglects important physical processes such as tunneling effect and surface wave while Mie theory overestimates the effects of these processes for nonspherical particles.

2.4.2 Irregular tetrahedral aggregates

One type of nonspherical particle whose optical properties are of interest is a cluster of bio-warfare agent spores. When a liquid solution containing such spores is aerosolized and the liquid evaporates, compact, nearly spherical clusters of these spores remain. Early warning systems depend on rapid identification of these particles, and elastic and fluorescent light scattering may play a crucial role in the development of such systems (Pinnick *et al.* 1998; Videen *et al.* 1998).

Herein, the PML FDTD is applied to an aggregation of spores which is approximated by four spherules in a tetrahedral orientation as shown in Fig. 2.12. The log of the scattering intensity as a function of the zenith and azimuth angle for the tetrahedral structure is shown in Fig. 2.13 for an incident angle of 0^o (z-direction). We can see the enhancement at three azimuth angles of 60^o, 180^o and 300^o when the zenith angle is $\sim 40^o$. More discussions on the application of the PML FDTD method to the light scattering from irregular tetrahedral aggregates are reported in Videen *et al.* (1998).

2.4.3 Deformed droplets

Deformed liquid droplets are of importance in industrial areas involving sprays, therapeutic aerosols, and combustion aerosols, where aerodynamic particle size is commonly measured to assess the airborne behavior of the droplets (Videen *et al.* 2000).

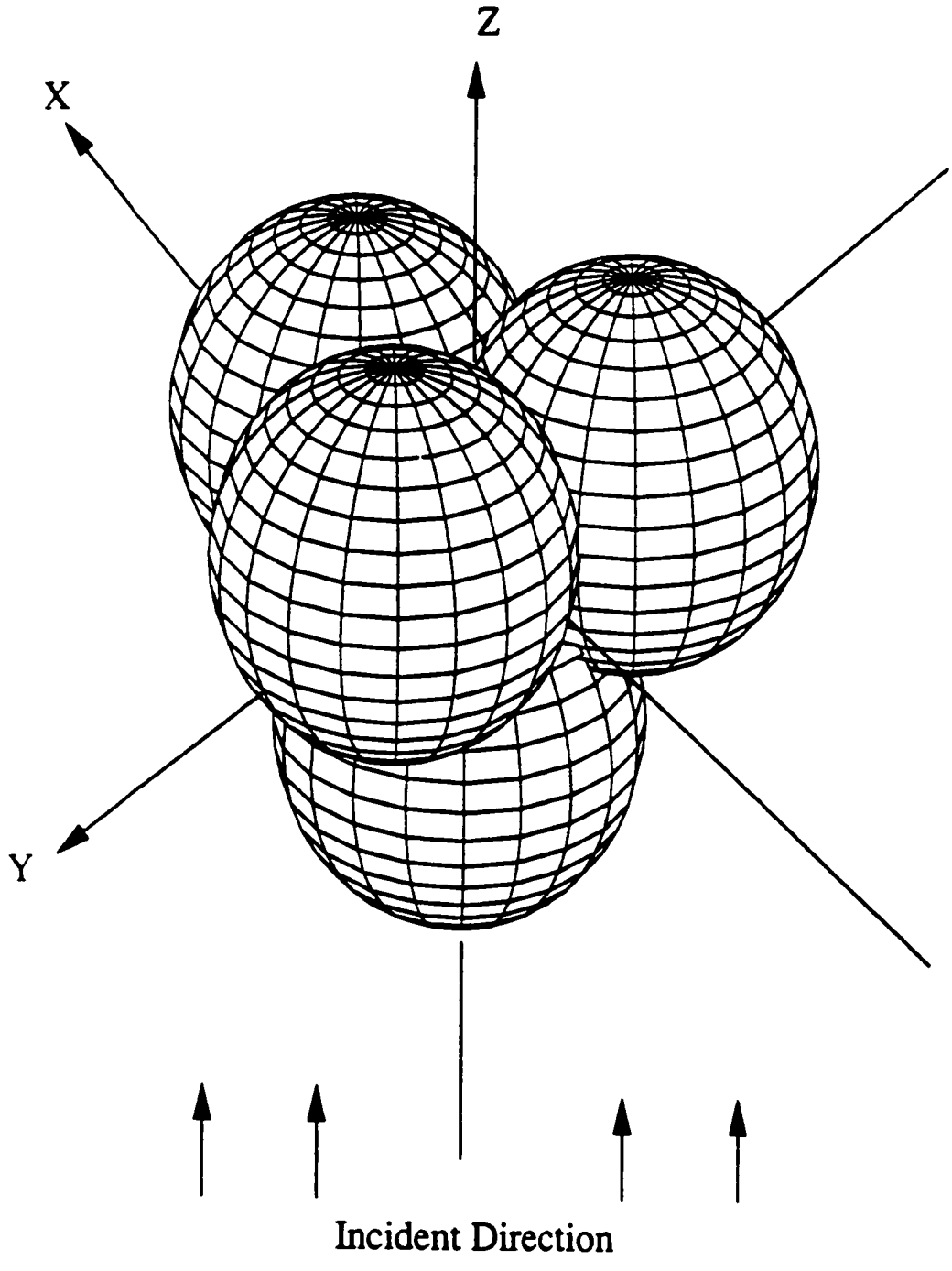

Figure 2.12: Diagram of the tetrahedral scattering system. Four $r = \lambda/2$,m = 1.53 + 0.001i spheres are in contact.

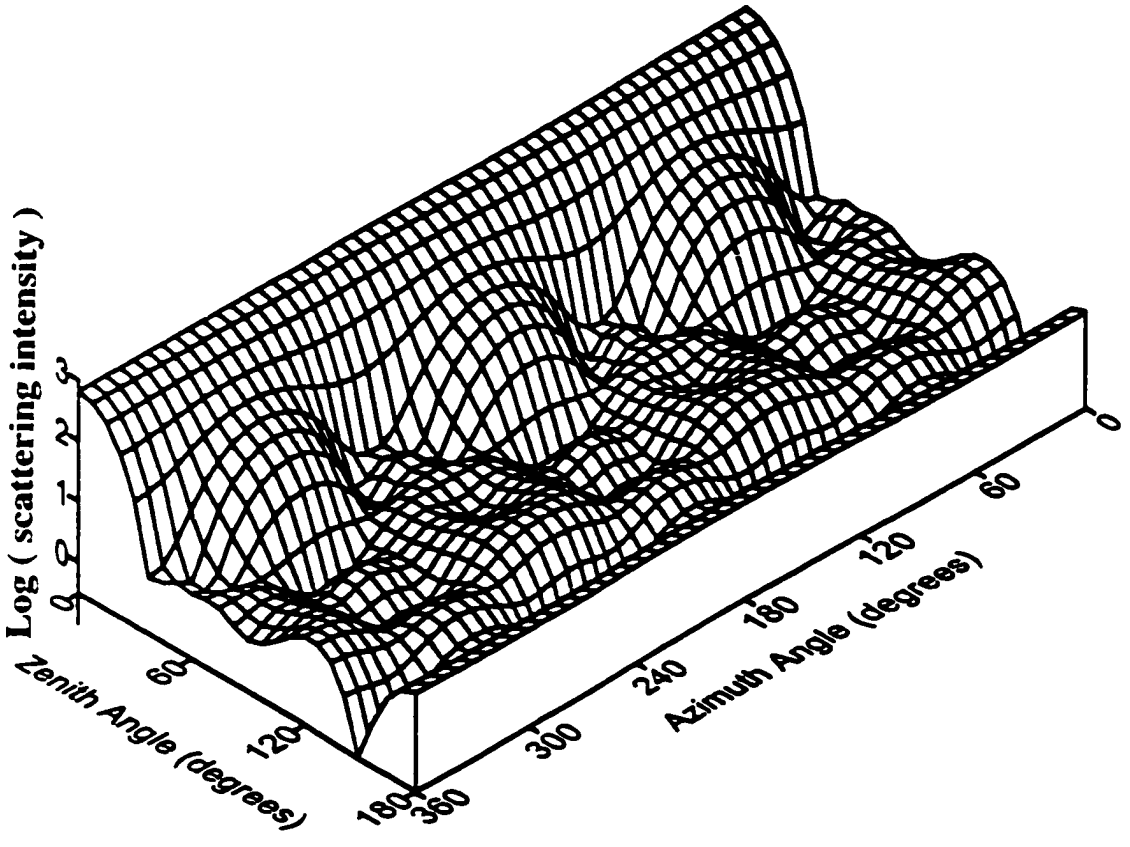

Figure 2.13: Angular dependence of the scattering intensity of the system illustrated in Figure 2.12 when the light is incident in positive z-direction.

With the development of multi-pixel detectors such as intensified charge-coupled device (ICCD) cameras, light scattering by these droplets can be angularly measured in a two-dimensional way. At the same time, modeling of the light scattering by deformed droplets is necessary not only for validation of the measurements, but also for retrieval of the droplet shapes from the measurements. In this study, light scattering by a distorted droplet is simulated with the FDTD technique. The shape of the distorted droplet is analytically given in a form (Videen *et al.* 2000)

$$r = r_0 + d(1 - 3cos^2\alpha), \tag{2.40}$$

where r_0 is the radius of an undistorted droplet and d is the amount of distortion. The droplet is axisymmetric about y axis as shown in Fig. 2.14. For the droplet to have an aspect ratio (the largest dimension L/ the smallest dimension D) of 2, $d = 0.246r_0$. Figure 2.15 shows the two-dimensional angular optical scattering by a deformed oleic-acid droplet illuminated edge-on at $\lambda = 0.6328$ μm ($m = 1.4599$) calculated with the FDTD technique. The aspect ratio of the droplet is 2. The size parameter in terms of D is $\pi D/\lambda = 24$. The radial direction originated at the center of the figure denotes the scattering angle θ from 0^o to 180^o. The azimuth angle ϕ is denoted by the anti-clockwise direction. The figure is plotted for azimuth angle from 90.5^o anti-clockwise to 88.5^o. The scattering from this particle displays high-intensity streaks and significant enhancement and weakness due to interference. This scattering pattern bears a strong resemblance to several of the experimentally measured patterns obtained by Secker *et al.* (2000) shown in Fig. 2.16. In Fig. 2.16, the laser beam is incident in a direction perpendicular to the falling direction of the droplet.

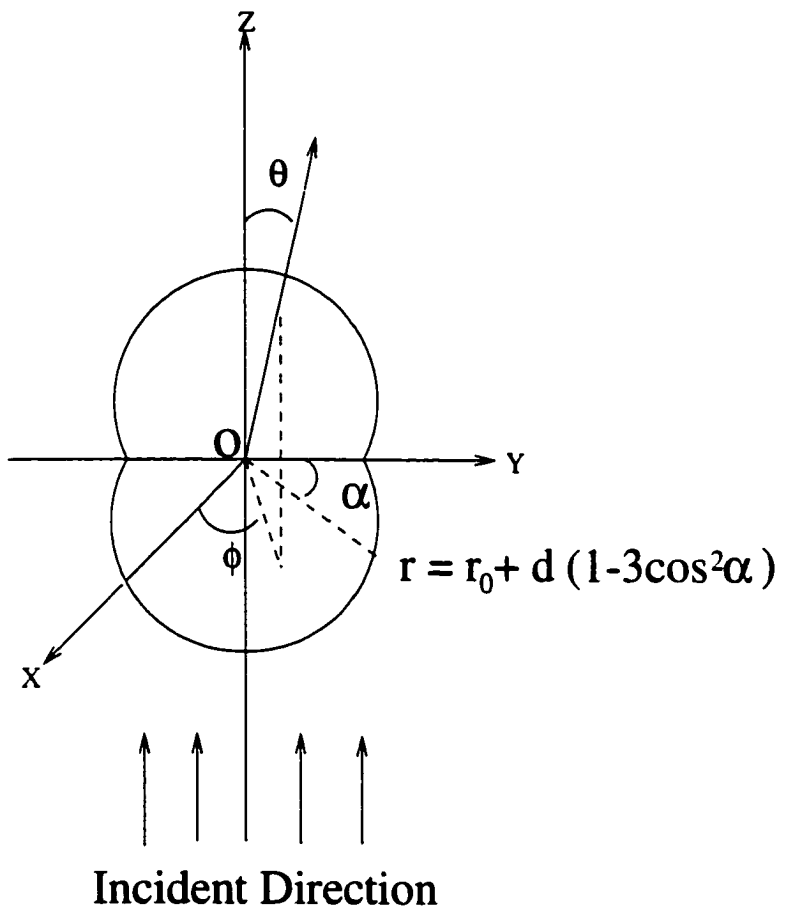

Figure 2.14: Diagram of a deformed droplet with edge-on incidence.

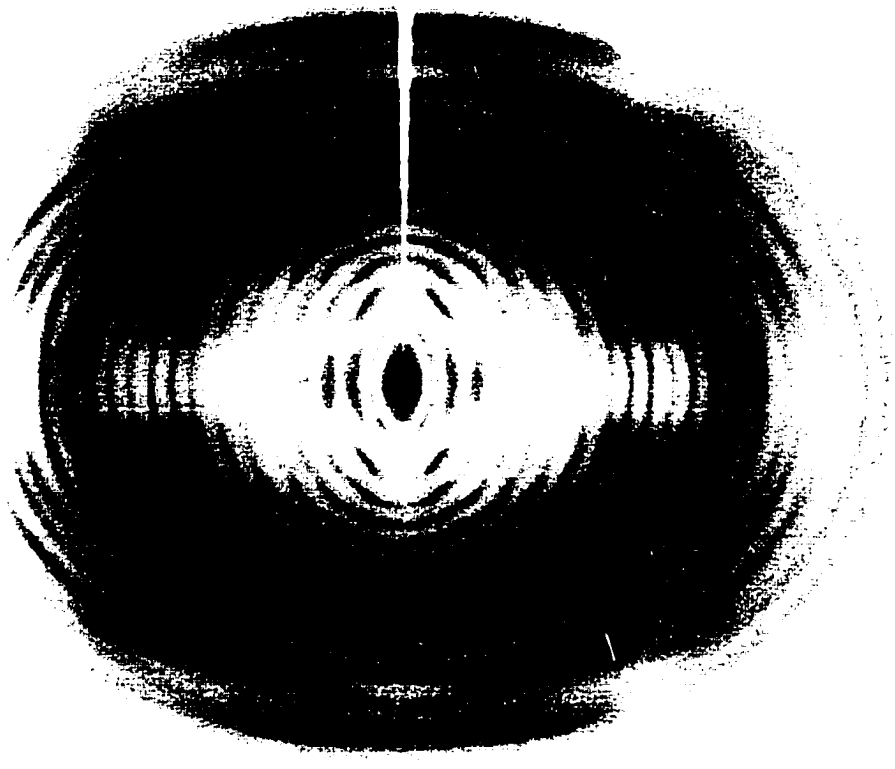

Figure 2.15: Two-dimensional angular optical scattering by a deformed oleic-acid droplet illuminated edge-on at $\lambda = 0.6328$ μm ($m = 1.4599$) calculated with the FDTD technique. The aspect ratio of the droplet is 2. The size parameter in terms of D is $\pi D/\lambda = 24$.

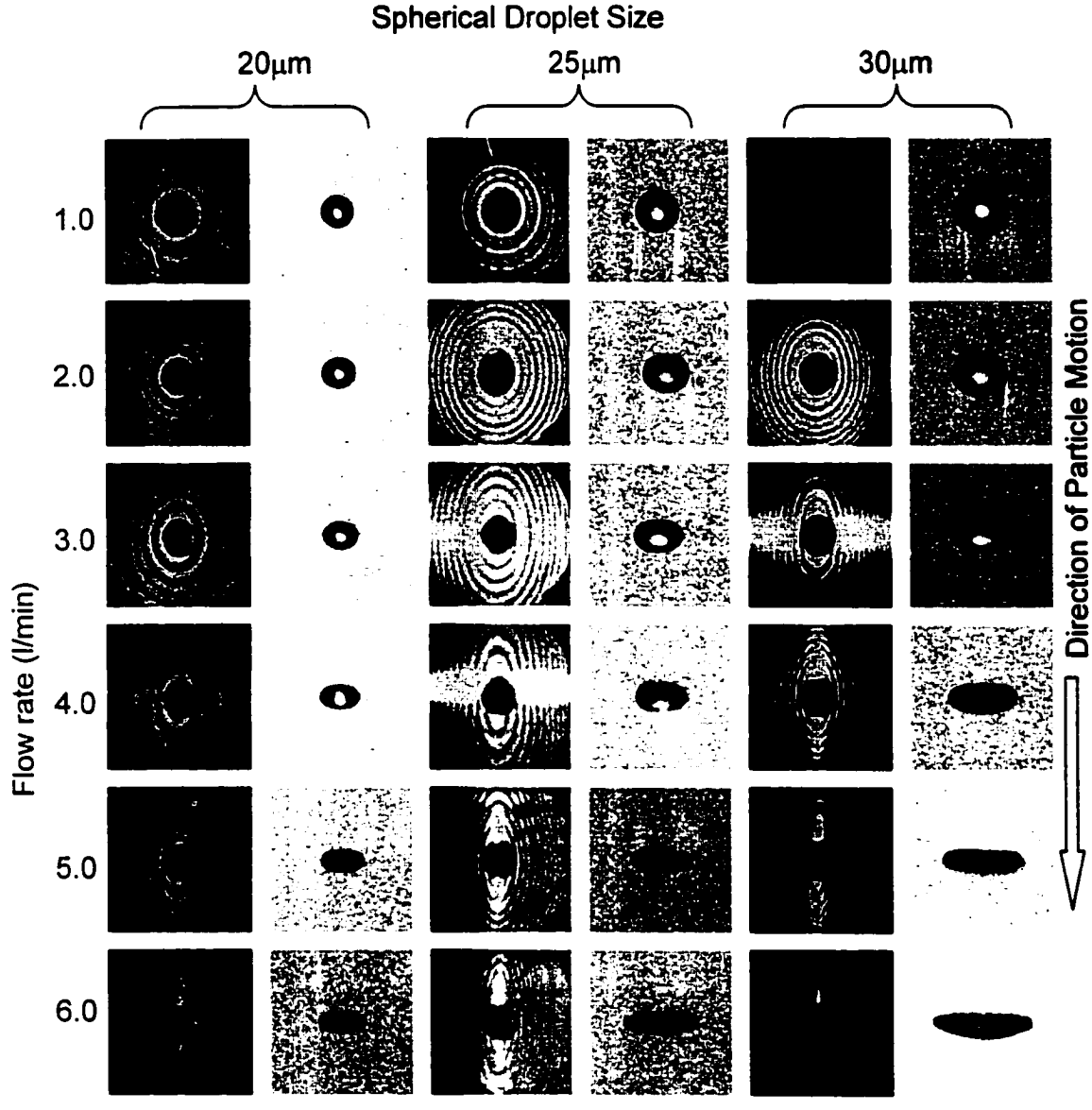

Figure 2.16: Experimentally measured light scattering patterns by oleic-acid droplets at $\lambda = 0.6328$ μm obtained by Secker *et al.* (2000).

2.5 Summary and conclusions

A finite-difference time domain (FDTD) program has been developed in this study. The perfectly matched layer (PML) absorbing boundary condition (ABC) has been used. This PML FDTD program is validated by Mie theory for spheres and by the multipole method for a nonspherical double-sphere system. Compared with these reference results, the relative errors in absorption and extinction efficiencies due to the PML FDTD are within ~1% for particles with size parameters as large as 40. The relative errors for the scattering phase function are typically within ~5%. The accuracy of this technique guarantees its reliability in applications to remote sensing and climate studies.

The PML FDTD scheme has been applied to hexagonal ice crystals at IR wavelengths. It is shown that the conventional approaches for light scattering by nonspherical particles introduce significant errors, particularly in the resonance region. This scheme has also been applied to the light scattering by irregular tetrahedral aggregates, which have potential application to early warning systems to identify clusters of bio-warfare agent spores. For applications to deformed droplets, this scheme may help people in the experimental field to identify the particle shapes.

Because of the use of the PML ABC, the computational domain for the FDTD is reduced significantly. In this study, the computations were performed on a regular workstation, even for particles with size parameters as large as 20.

Chapter 3

Application of the finite-difference time domain technique to light scattering by dielectric particles with large complex refractive indices

3.1 Introduction

There exist materials with large complex refractive indices, which include, e.g., water and high-water-content biological tissues at microwave wavelengths. The study of electromagnetic wave scattering and absorption by highly refractive dielectric targets with arbitrary shape and composition has important applications in radar remote sensing (Battan 1973) and in the study of microwave propagation in the biological tissues (Nadobny 1998).

Using a perfectly matched layer (PML) absorbing boundary condition (ABC) (Berenger 1994, 1996; Katz *et al.* 1994), we have developed a three-dimensional (3D)

FDTD scheme for light scattering by nonspherical dielectric particles as presented in Chapter 2. When a grid cell size of $\lambda/20$ was employed, we showed that the 3D PML FDTD method can achieve an accuracy of ~1% in extinction and absorption efficiencies and ~5% in scattering phase function for particles with size parameters as large as 40 (i.e., D~13λ). In the work reported in Chapter 2, however, the 3D PML FDTD model was applied to light scattering by ice crystals, biological spores, and oleic-acid droplets, whose refractive indices are generally small. In this study, we will focus on the application of the FDTD method to highly refractive dielectric particles.

In Section 3.2, we will discuss the numerical treatments related to particle boundaries in the finite-differencing scheme and appropriate methods will be presented. In Section 3.3, we will first present the numerical results in order to show the importance of appropriate boundary treatments in the FDTD solutions. The accuracy of the FDTD scheme is then determined for particles with $m = 7.1499 + 2.914i$ using the exact solutions. The summary and conclusions will be given in Section 3.4.

3.2 Particle boundary treatments

In the 3D PML FDTD model, the target is defined with cubic grid cells. Therefore, the staircasing effect has always been a source of errors. Because of the large discontinuity in permittivity between the target and surrounding medium for particles with a large refractive index, the numerical treatments of the electromagnetic fields near the particle boundaries will also become an important issue in the FDTD simulations.

3.2.1 Dielectric property treatment

In the FDTD method, the scatterer with an arbitrary shape and composition is approximated with an array of cubic cells. At each position of the electric field components (See Fig.2.1), the permittivity of the medium in the computational domain including the scatterer must be assigned before the time-marching of the FDTD formulation. For cells totally inside one medium, the permittivity is homogeneous. But

for cells split by the particle boundaries, the permittivity at different field-component positions may not be identical. In our FDTD scheme, we have used the local values of the permittivity at different field-component positions.

For the cells split by the interfaces between neighboring media, however, the averaging techniques for the material properties are often used. In the FDTD model developed by Yang and Liou (1996a; 1998b), the grid cell was considered to be the basic spatial unit and the permittivity was assumed to be homogeneous for each cell. Thus, for any grid cell with inhomogeneous permittivity, such as grid cells split by the particle-boundary interfaces, an effective permittivity was evaluated using an effective medium theory. The most widely used effective-medium theories are the Maxwell-Garnett theory and the Bruggeman theory (Chýlek and Srivastava 1983). If particles of one material are dispersed in a continuous host of another material (separated-grain structure), the use of the Maxwell-Garnett rule is indicated. If the space is filled by a random mixture of two or more constituents (aggregate structure), the Bruggeman theory is the appropriate option. Other frequently used effective-medium theories are the volume average of the dielectric constants and the volume average of the refractive index (Dobbie and Chýlek 1998). Unfortunately, when a space is filled with two constituents, but they are clearly separated by a single interface (which is the case of a FDTD grid cell split by the particle edge), there seems no sound basis for all these mixing rules to be applied. Following Yee (1966), Yang and Liou (1996a; 1998b) selected components of the magnetic field at the center of cell faces and the electric field counterparts at the cell edges. Therefore, another averaging, which involves four neighboring cells for each electric component position, was recommended to evaluate the permittivity for the FDTD simulation. Recent studies (Nadobny *et al.* 1998), however, have suggested that extra errors in the light scattering simulation could be caused by the averaging of the material property.

In the next section, numerical results will be presented to show that for the permittivity at different field-component positions, using simply the local value of the permittivity at each point is more accurate than using averaged values. For the

comparison purpose, the averaging is done within a cubic cell centered at the corresponding field-component position. The Maxwell-Garnett rule with free space as the host is used to evaluate the effective permittivity if the free space exceeds half of the cubic averaging range; otherwise, the inverted Maxwell-Garnett rule with particle material as the host is used. It should be noted that the averaging method used here involves only one-time averaging to obtain the electric permittivity for the FDTD simulation, which is found to work better than the method involving two-time averaging.

3.2.2 Electric field interpolation

The FDTD can only produce the components of near fields at the mesh grid points as shown in Fig. 2.1. However, because the scattering phase matrix, and the extinction and absorption cross-sections are determined by the scattered far field, it is necessary to transform the near field to the far field (Yang and Liou 1996a). In this study, we use a volume integration method (Purcell and Pennypacker 1973; Goedecke and O'Brien 1988; Flatau *et al.* 1990; Draine and Flatau 1994; Yang and Liou 1996a) to evaluate the scattering and absorption properties. Here, without sacrificing the generality, we will address some issues related to the volume integration using a homogeneous particle. Its absorption cross-section, e.g., can be written in the FDTD scheme using the cubic cell in the form

$$\sigma_a = \frac{k}{|\vec{E}_0|^2} \int\int\int_v \epsilon_i(\vec{\xi})\vec{E}(\vec{\xi}).\vec{E}^*(\vec{\xi})d^3\xi.$$

$$= \frac{2\pi\epsilon_i\Delta s^3}{|\vec{E}_0|^2} \sum_{i,j,k} |\vec{E}[(i+\Delta i)\Delta s, (j+\Delta j)\Delta s, (k+\Delta k)\Delta s]|^2 \delta_{i,j,k}, \tag{3.1}$$

where $\vec{E}_0$ is the incident electric vector and v is the volume of the particle. For cells totally in the particle, $\Delta i = \Delta j = \Delta k = 0$ and $\delta_{i,j,k} = 1$. But for cells split by the particle boundaries, $\delta_{i,j,k}$ is the fraction of the particle volume within the cell, and Δi, Δj and Δk are so defined that $[(i+\Delta i)\Delta s, (j+\Delta j)\Delta s, (k+\Delta k)\Delta s]$ is the gravity

center of the particle volume within the cell. It is noted that when $|\vec{E}|^2 = 1$, we have $\Delta s^3 \sum_{i,j,k} \delta_{i,j,k} = v$. Similar volume integration is required to obtain the extinction cross-section and the scattering phase matrix.

In the FDTD scheme, the electric components Ex, Ey and Ez for each cell are not evaluated at the same position (Fig.2.1) and they are all perpendicular to their respective cubic cell faces. To perform the volume integration numerically, we need to interpolate the electric field components at the FDTD grid points to the gravity center of the cell. The simplest way to do so is to directly interpolate the FDTD electric components for Ex, Ey and Ez at the gravity center of the cell. This is valid if the permittivity difference between the particle and the surrounding medium is small so that the field discontinuity at the particle boundaries is not significant. However, when the permittivity difference between the particle and the surrounding medium is large, the direct interpolation of the FDTD electric components within the cells split by the particle boundaries would result in significant errors, as will be shown in the next section.

To interpolate the FDTD field components within the cells partially occupied by the particle, the ideal method is to use the exact boundary condition for electromagnetic fields at the material interfaces; that is, the tangential components of electric fields and the normal components of the electric displacements are continuous through the interfaces. When a particle is implemented in the FDTD mesh, the normal vector of the particle surface element can be determined in principle. Therefore, for the field interpolation within the cells involving the particle boundary, we can first decompose the FDTD electric vectors into the normal and tangential field components relative to the boundary surface elements. Following the exact boundary condition, the tangential components of electric fields and the normal components of the electric displacements are then interpolated. After the interpolation, the normal electric field components are obtained from the interpolated normal electric displacements divided by the particle permittivity.

In a FDTD grid cell split by the particle boundary, the normal direction of the

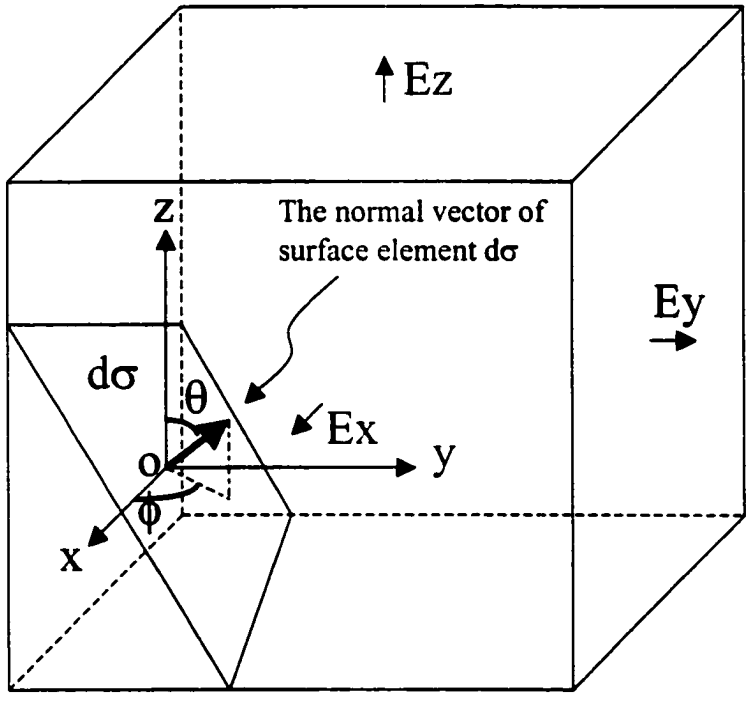

Figure 3.1: Schematic diagram of a particle surface element within a FDTD grid cell and its normal vector.

particle surface element can be defined using its local zenith and azimuth angles θ and ϕ with respect to the FDTD Cartesian coordinates (See Fig. 3.1). So for the given grid cell, the projections of the FDTD electric components Ex, Ey and Ez to the radial, θ and ϕ directions are

$$Ex_r = Ex sin\theta cos\phi, \tag{3.2a}$$

$$Ex_\theta = Ex cos\theta cos\phi, \tag{3.2b}$$

$$Ex_\phi = -Ex sin\phi, \tag{3.2c}$$

$$Ey_r = Ey sin\theta sin\phi, \tag{3.2d}$$

$$Ey_\theta = Ey cos\theta sin\phi, \tag{3.2e}$$

$$Ey_\phi = Ey cos\phi, \tag{3.2f}$$

$$Ez_r = Ez cos\theta, \tag{3.2g}$$

$$Ez_\theta = -Ez sin\theta, \tag{3.2h}$$

$$Ez_\phi = 0, \tag{3.2i}$$

where the θ and ϕ components above are parallel to the surface element, while the radial component is perpendicular to it. Therefore, based on the boundary conditions for electromagnetic fields at the material interfaces, we can perform linearly interpolation using the electric displacement for the radial components and using the electric field for the θ and ϕ components.

The interpolations would be done for all components in Eq.(3.2) individually. Then the interpolated components at the cell or gravity center of the given cell could be added together for the radial, θ and ϕ directions, respectively, and denoted as D_r, E_θ and E_ϕ. Here, D_r is the electric displacement component in the radial direction.

These fields could be transformed into electric components in the Cartesian coordinate system using

$$Ex = \frac{D_r}{\epsilon} sin\theta cos\phi + E_\theta cos\theta cos\phi - E_\phi sin\phi, \tag{3.3a}$$

$$Ey = \frac{D_r}{\epsilon} sin\theta sin\phi + E_\theta cos\theta sin\phi + E_\phi cos\phi, \tag{3.3b}$$

$$Ez = \frac{D_r}{\epsilon} cos\theta - E_\theta sin\theta, \tag{3.3c}$$

where ϵ is the permittivity of the particle.

If a particle has a regular shape such as spheres, spheroids, cubes and circular cylinders, etc., it is practical to do the field interpolation using the exact boundary conditions. However, for particles with arbitrary shapes, it would be much more difficult, although not impossible, to use this treatment. Therefore, in this study, we also test another approximate boundary field interpolation. In this method, we first obtain the electric displacement components using the FDTD electric components multiplied by the local permittivity. We then interpolate the electric displacement components to the gravity center of each cell. The electric components used in Eq.(3.1) would be the interpolated electric displacement divided by the particle permittivity. Again, this treatment has significance only for the grid cells split by the particle edge. For other grid cells, either inside or outside the particle, because the dielectric constants are the same, this treatment is equivalent to simply doing the interpolation for electric fields.

It should be noted that for the interpolation at the gravity center (which is different from the cell center for a cell split by the particle edge), the FDTD field components on the neighboring grid cells are also needed. However, if we use the electric field at the cell center in Eq.(3.1), the FDTD field components on the given grid cell are enough for the interpolation. This simplification may cause some errors but requires significantly less memory or computational time. Therefore, it is also worth examining the errors due to the use of the cell-center interpolation. Note here that, for

the interpolation involving the electric displacements, the related electric component is still the interpolated electric displacement divided by the particle permittivity.

3.3 Numerical results

In the numerical simulations, we set a 6-cell thick PML with reflection coefficient $R(0)$ of 10^{-5} and keep 6 cells for free space between the scatterer and the PML (Berenger 1994, 1996; Katz *et al.* 1994). If not specified, a grid cell size $\Delta s = \lambda_d/20$ is used, where λ_d denotes the wavelength inside the particle. The accuracy of the FDTD results is examined using Mie theory which is exact for spheres. The size parameter of a particle is defined as $2\pi a/\lambda$, where a is the radius of the sphere and λ is the wavelength in the surrounding medium.

3.3.1 Effects of particle boundary treatments

A wide range of refractive indices are used to examine the effects of the treatments involving particle boundary on the FDTD simulations. These refractive indices include 1.311, $1.4717 + 0.389i$ and $5 + 2i$. The size parameters used are those where the extinction is the most significant. For refractive indices 1.311 and $1.4717 + 0.389i$ a size parameter of 6 is used. For refractive index $5 + 2i$, a size parameter of 2 is chosen.

Figure 3.2 shows the comparison of the scattering phase functions for spheres from Mie theory and those from the FDTD schemes. In the FDTD calculations, the dielectric constant (permittivity) at the location of the electric components for a given cell is either the averaged value, as discussed in Section 3.2 (average), or simply the local value at that point (no average). In both FDTD simulations, the electric fields in frequency domain are interpolated to the gravity center of each grid cell by considering the exact boundary conditions. We can see that, using the averaged dielectric constant, the errors in phase functions are generally larger, especially for the backscattering and the scattering minima. Figure 3.2 shows that the errors in

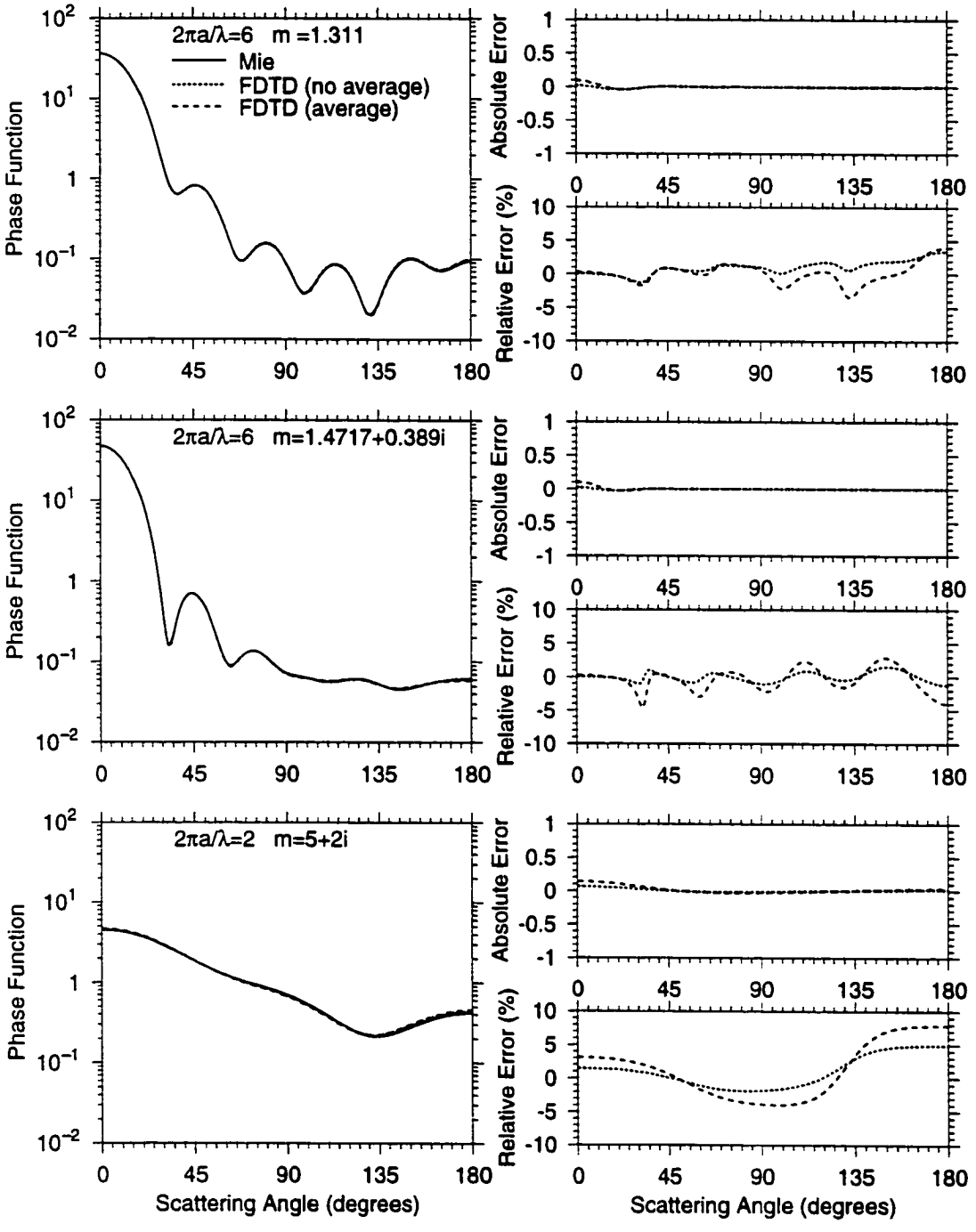

Figure 3.2: Comparison of the scattering phase functions for dielectric spheres with different refractive indices from Mie theory and those from the FDTD using different dielectric property treatments. In the FDTD calculations, the dielectric constant used at each position of the electric field components for a cell is either the averaged value (average) or simply the local value at that point (no average). The grid cell size is $\lambda_d/20$ where λ_d is the wavelength inside the particle. The size parameter is defined as $2\pi a/\lambda$ where a is the radius of the sphere and λ is the wavelength in the air.

the scattering phase function due to the FDTD without averaging of the permittivity are less than ~5%. Therefore, we recommend that the local value of the dielectric constant should be used in the FDTD scheme, which is not only more accurate, but which also requires less computational time and memory when compared with the scheme using average.

The effects of different field-interpolation schemes, including those using the electric-field (E), electric-displacement (D), and the exact boundary conditions (BC), are then examined. We compare the FDTD results using the three field-interpolation methods with those from Mie theory. In all the FDTD calculations, the local values of the dielectric constants are used, and the field components are interpolated at the gravity centers of the grid cells. Figure 3.3 shows the comparison of the scattering phase functions for spheres between Mie theory and the FDTD simulations. We can see that for all refractive indices used here, the interpolations using exact boundary conditions (BC) and electric displacement (D) give better results with errors smaller than ~5%. For small refractive indices, the electric-field interpolation (E) works well with errors smaller than 3% and 6% for $m = 1.311$ and $m = 1.4717 + 0.389i$, respectively. However, for large complex refractive indices, the errors due to the FDTD using the electric-field interpolation become large. For $m = 5 + 2i$, the error can reach ~12%. This happens because the dielectric constant varies greatly between the particle and the surrounding medium, which leads to the significant discontinuity of the normal-electric-field components at the particle boundary. Therefore, direct interpolation of the electric fields is not generally valid for particles with large refractive indices.

We have also checked the sensitivity of the FDTD results to the field-interpolation positions. Herein, the field components are interpolated either at the cell center or at the gravity center for a given grid cell. Figure 3.4 shows the comparison of the scattering phase functions for spheres calculated from Mie theory and those from the FDTD with different field interpolation positions. In the FDTD simulations, we use the local dielectric constant at each grid point for the wave propagation simulation, and use the exact boundary conditions for the field interpolation. We can see that

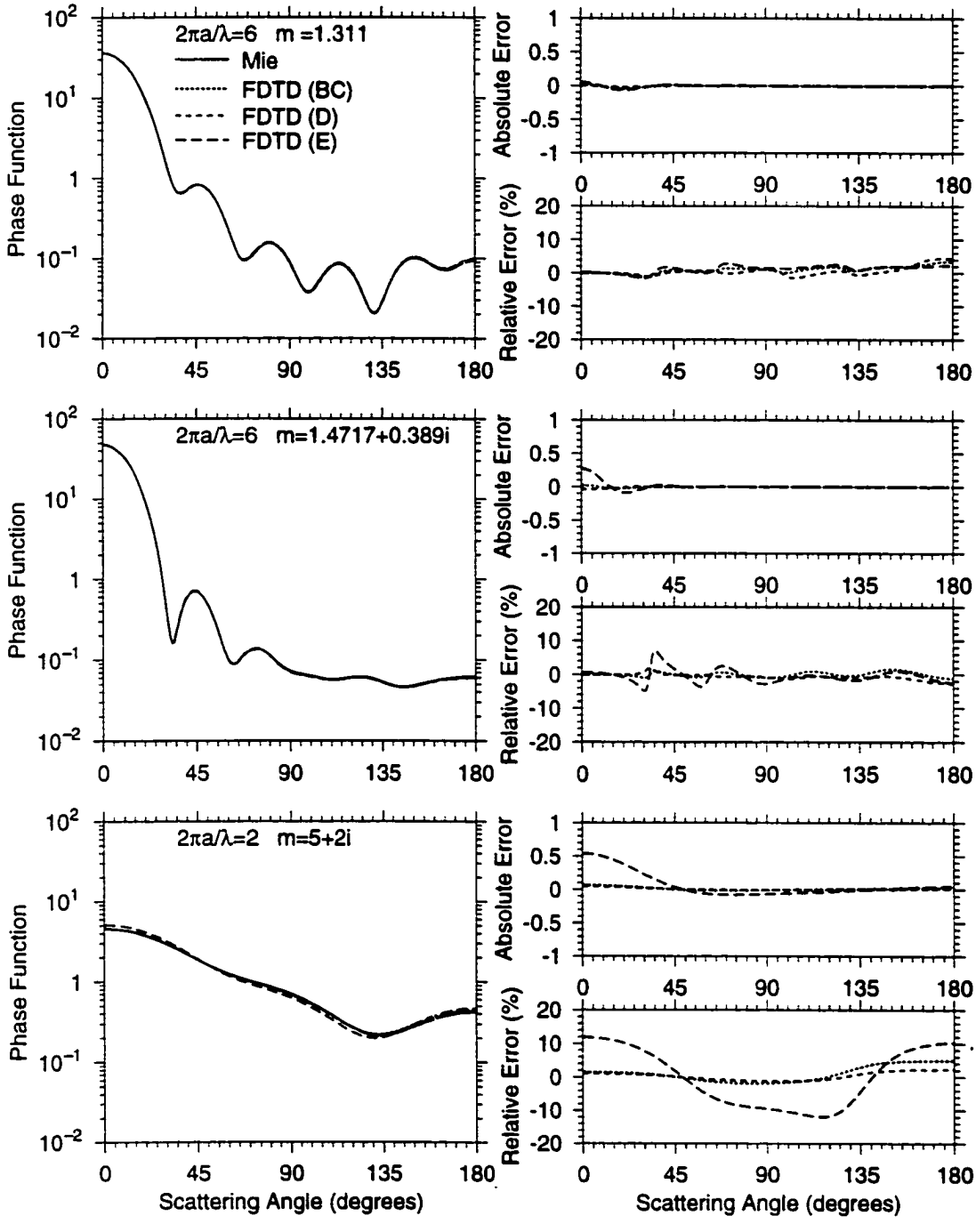

Figure 3.3: Comparison of the scattering phase functions of dielectric spheres with different refractive indices from Mie theory and those from the FDTD using different field-interpolation methods. Here *BC* denotes the interpolation using exact boundary conditions, *D* using the electric displacement, and *E* directly using electric field.

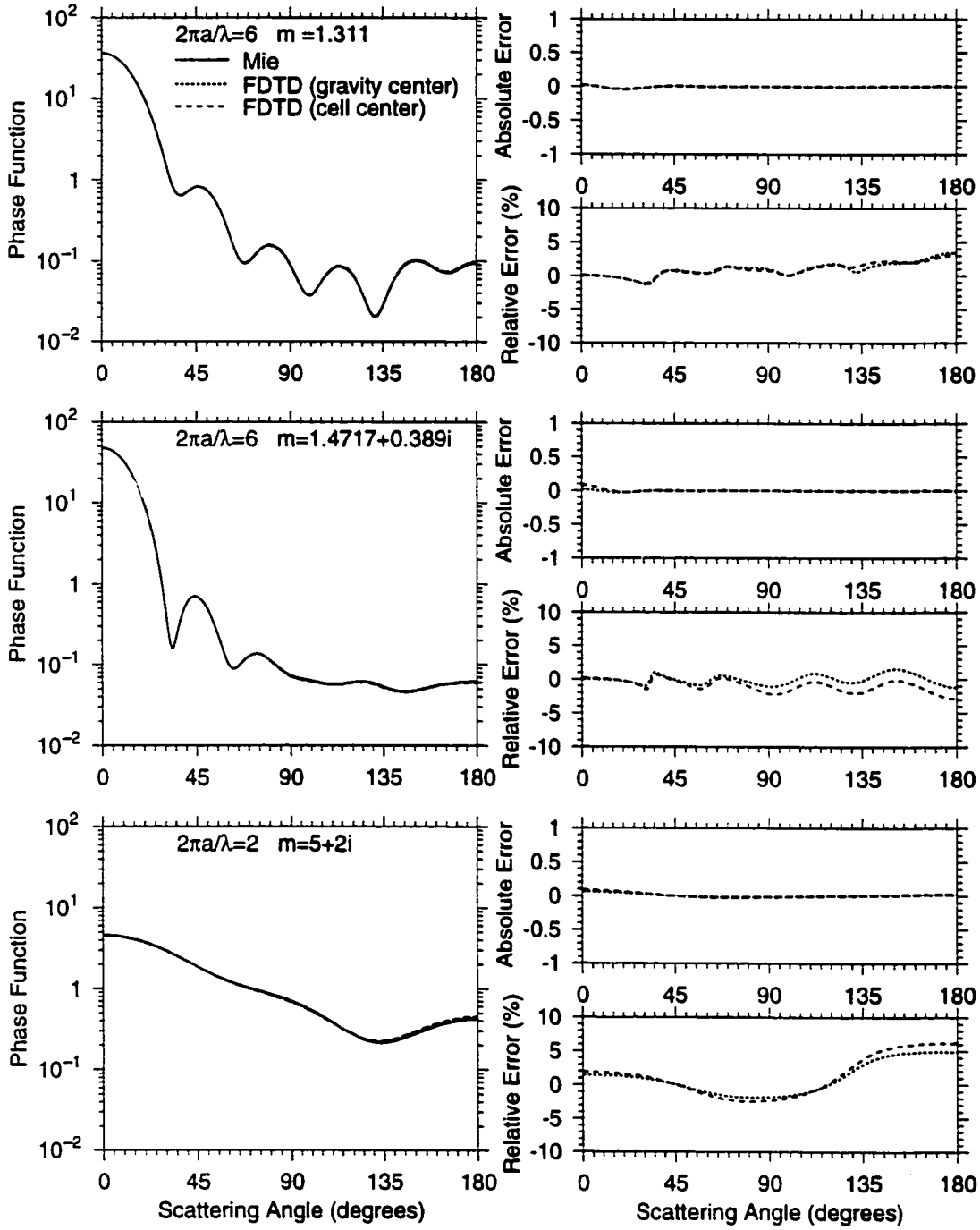

Figure 3.4: Comparison of the scattering phase functions of dielectric spheres with different refractive indices from Mie theory and those from the FDTD using different field interpolation positions. In the FDTD calculations, the field components are interpolated either at the cell center or at the gravity center.

the FDTD results are more sensitive to the interpolation position when the refractive index becomes larger. For refractive indices of $1.4717 + 0.389i$ and $5 + 2i$, using the interpolation at the cell center produces ~2-4% more errors in the scattering phase function.

The extinction and absorption efficiencies for the cases shown in Figs.3.2-3.4 are listed in Table 3.1. We can see that for small refractive indices (1.311 and $1.4717+0.389i$), all methods work well for the extinction and absorption calculations. The errors are generally ~1%, except for the FDTD using the electric displacement interpolation, which has errors ~2%. However, for large complex refractive index ($5+2i$), the FDTD with the electric field interpolation can result in an error of ~18%. The FDTD schemes using other interpolation methods for highly refractive particles can work well, but with larger errors than for small refractive indices. Here we can see again that, although the FDTD using the averaged dielectric constant is numerically more complicated, it introduces little advantage in accuracy in comparison with the scheme using the local dielectric constant. This is especially the case for the particles with large refractive indices. Table 3.1 shows that, the FDTD scheme using the local value of dielectric constant and interpolation at the gravity center by considering the electromagnetic boundary conditions can work well for both small and large refractive indices. The relative errors in the absorption and extinction efficiencies are smaller than ~3%. The FDTD using the electric-displacement interpolation can also produce reliable results for a wide range of refractive indices; and for particles with arbitrary shapes it is a more practical method. It is worth mentioning here that although the cell center interpolation produces more errors than the gravity center interpolation, the former is numerically more efficient.

3.3.2 Numerical results for $m = 7.1499 + 2.914i$

One application of the FDTD scheme is in the centimeter radar remote sensing of precipitating hydrometeors including raindrops, snow and hail/graupel. Since the hydrometeors are generally nonspherical, and can be a mixture of ice and water (e.g.,

Table 3.1: The extinction and absorption efficiencies for the cases in Figs. 3.2-3.4.

	$2\pi a/\lambda = 6$ m = 1.311	$2\pi a/\lambda = 6$ m = 1.4717 + 0.389i		$2\pi a/\lambda = 2$ m = 5 + 2i	
	Qe	Qe	Qa	Qe	Qa
Mie theory	3.8213	2.4864	1.3119	2.8063	1.0513
FDTD(no average)	3.7871(-0.89%)	2.4685(-0.71%)	1.3025(-0.71%)	2.8777(+2.54%)	1.0828(+2.99%)
FDTD(average)	3.7909(-0.80%)	2.4865(+0.00%)	1.3103(-0.12%)	2.9896(+6.53%)	1.1174(+6.28%)
FDTD(BC)	3.7871(-0.89%)	2.4685(-0.71%)	1.3025(-0.71%)	2.8777(+2.54%)	1.0828(+2.99%)
FDTD(D)	3.7775(-1.14%)	2.4278(-2.35%)	1.2793(-2.48%)	2.7690(-1.32%)	1.0222(-2.76%)
FDTD(E)	3.8008(-0.53%)	2.5059(+0.78%)	1.3208(+0.67%)	3.3223(+18.3%)	1.2384(+18.0%)
FDTD(gravity center)	3.7871(-0.89%)	2.4685(-0.71%)	1.3025(-0.71%)	2.8777(+2.54%)	1.0828(+2.99%)
FDTD(cell center)	3.7722(-1.28%)	2.4652(-0.85%)	1.3054(-0.49%)	2.8816(+2.68%)	1.1021(+4.83%)

hailstone), the interpretation of the radar reflectivity requires the light scattering scheme such as the FDTD for nonspherical particles with arbitrary composition. Here, the FDTD scheme is examined for dielectric spheres with a large refractive index of $7.1499 + 2.914i$. This refractive index is for water at the wavelength of 3.2 cm. In the FDTD simulation, we use the local value of the dielectric constant; and in the volume integration to obtain the single-scattering properties, we apply the interpolation for electric fields at the cell gravity center by considering the exact boundary conditions.

Figure 3.5 shows the extinction efficiency (Q_e), absorption efficiency (Q_a) and asymmetry factor (g) as functions of size parameters ($2\pi a/\lambda$) calculated using Mie theory and the FDTD for water spheres at a wavelength of 3.2 cm ($m = 7.1499 + 2.914i$). Also shown are the absolute and relative errors of the FDTD results. For the size parameters larger than one, we can see that the relative errors for Qe and Qa from the FDTD using $\Delta s = \lambda_d/20$ are generally within ~3% and ~4%, respectively. The errors in asymmetry factors due to the FDTD are smaller than ~1%. For size parameters smaller than 1.0, the relative errors in the single scattering properties become larger. This is largely because $\Delta s = \lambda_d/20$ could not resolve the small spheres well. To verify this explanation, Fig. 3.5 also shows the finite-difference time domain results for size parameters smaller than 3 by using higher resolution so that the small particles are resolved equally well as the particle with the size parameter 3. In this case, we can see that the relative errors in the extinction and absorption coefficients are smaller than ~4% for small particles.

The comparisons of scattering phase functions from Mie theory and the FDTD scheme with $\Delta s = \lambda_d/20$ for different size parameters are shown in Figs. 3.6 and 3.7. We can see that the errors in the scattering phase functions are typically smaller ~5%.

Figure 3.8 presents the effect of the cell size on the FDTD results. Here we consider a water sphere with size parameter of 3 for a wavelength of 3.2 cm. The cell sizes of $\lambda_d/20$, $\lambda_d/25$ and $\lambda_d/30$ are used. We can see that the relative errors decrease when higher resolution meshes are used.

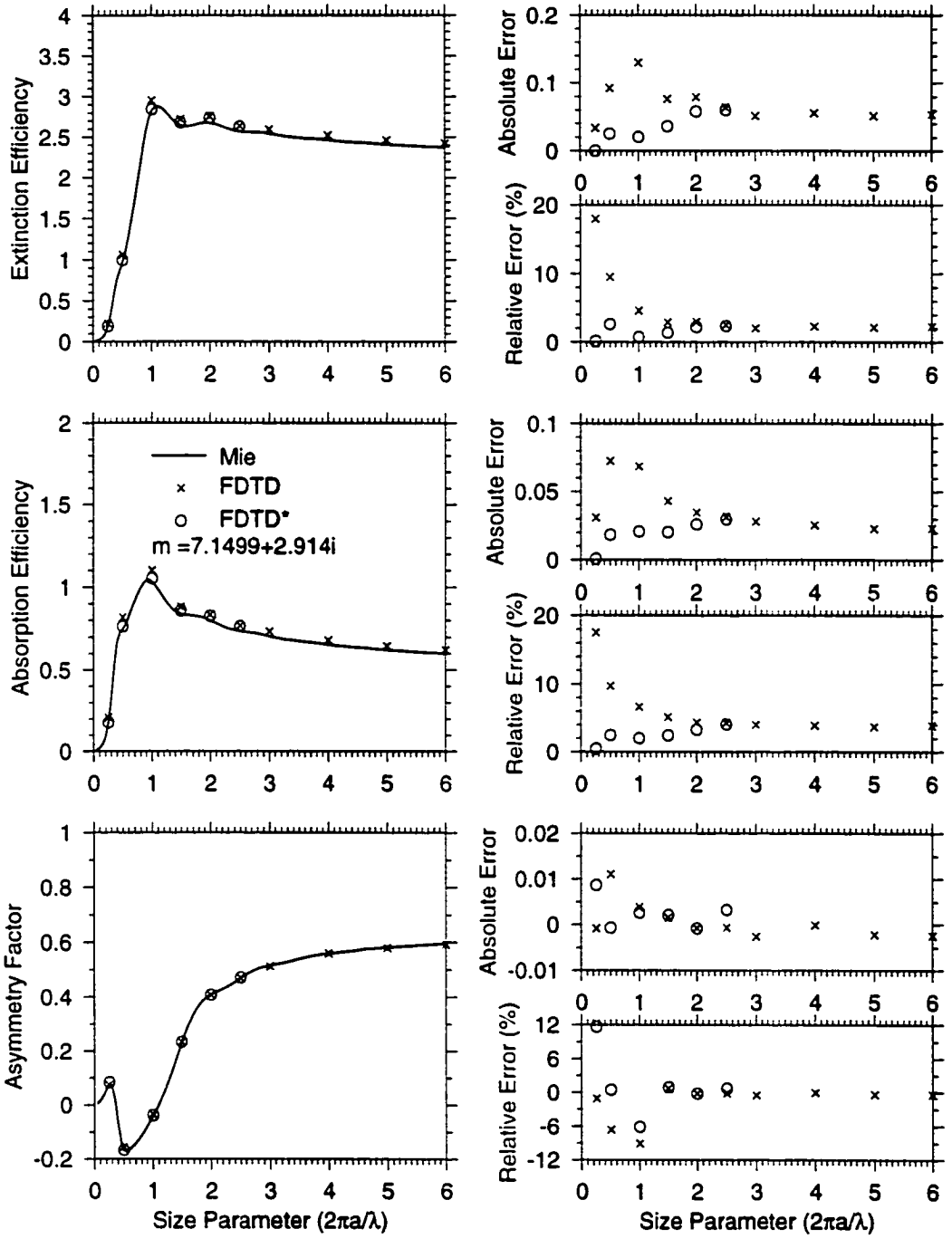

Figure 3.5: Extinction and absorption efficiencies, and asymmetry factor for water spheres as functions of size parameters. These results are from Mie theory and the FDTD at a wavelength of 3.2 cm ($m = 7.1499 + 2.914i$). In the FDTD calculation, a grid cell size of $\lambda_d/20$ is used. For size parameters smaller than 3, the FDTD results (FDTD*) are also shown by using the cell size so that the number of cells are the same as that for the particle with the size parameter of 3.

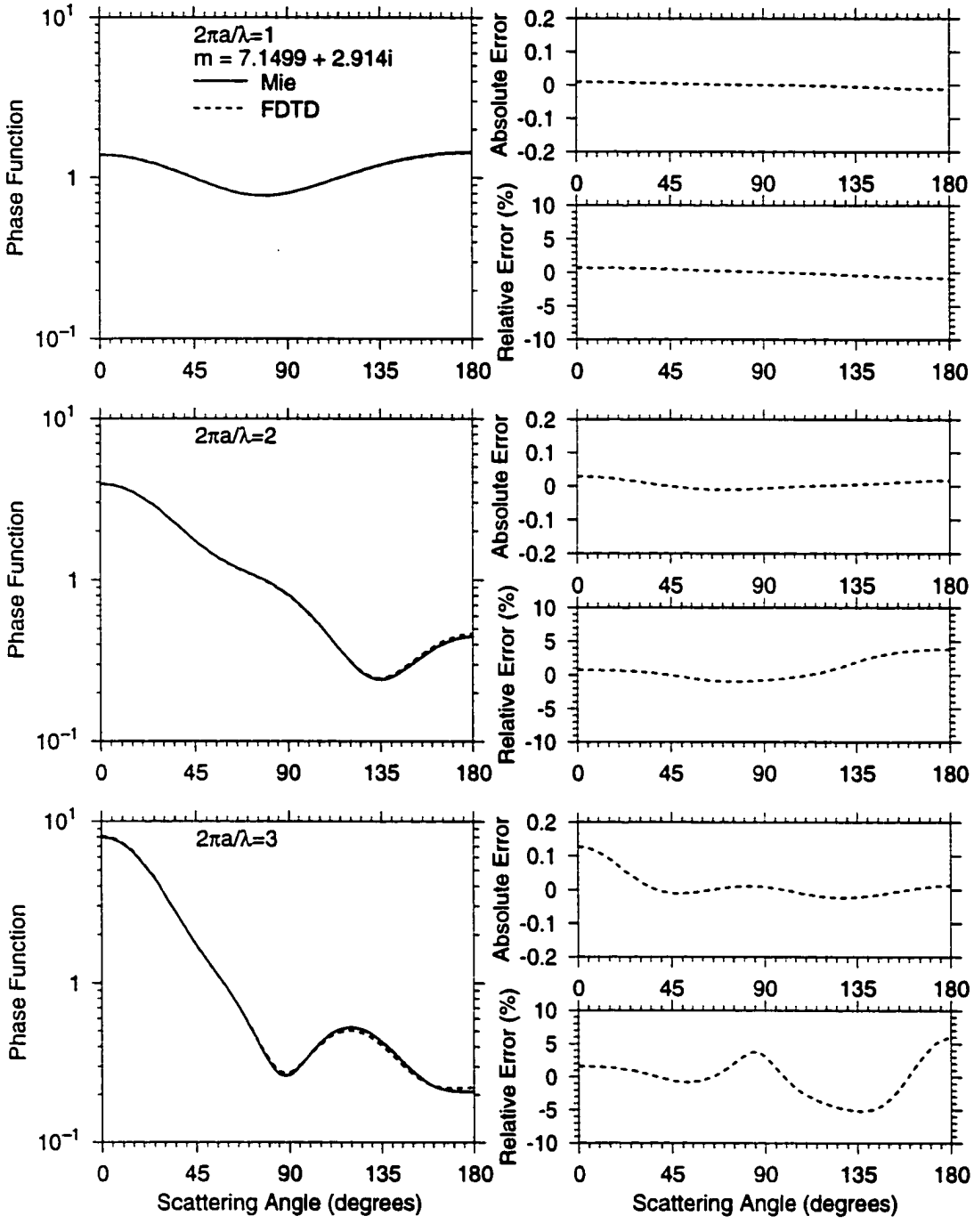

Figure 3.6: Comparison of the scattering phase functions for water spheres from Mie theory and those from the FDTD at a wavelength of 3.2 cm ($m = 7.1499 + 2.914i$) for size parameters of 1, 2 and 3.

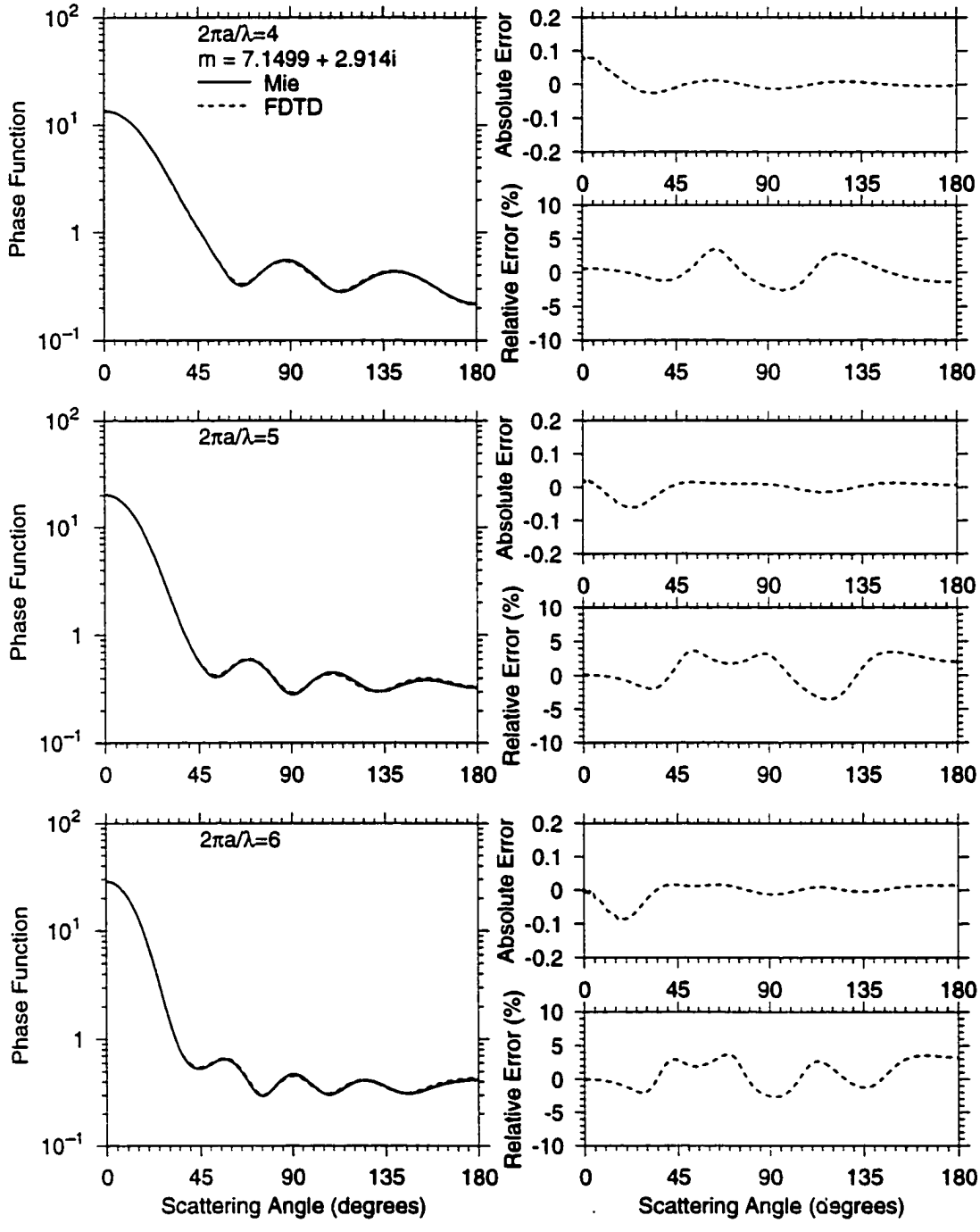

Figure 3.7: Same as Fig. 3.6, but for size parameters of 4, 5 and 6.

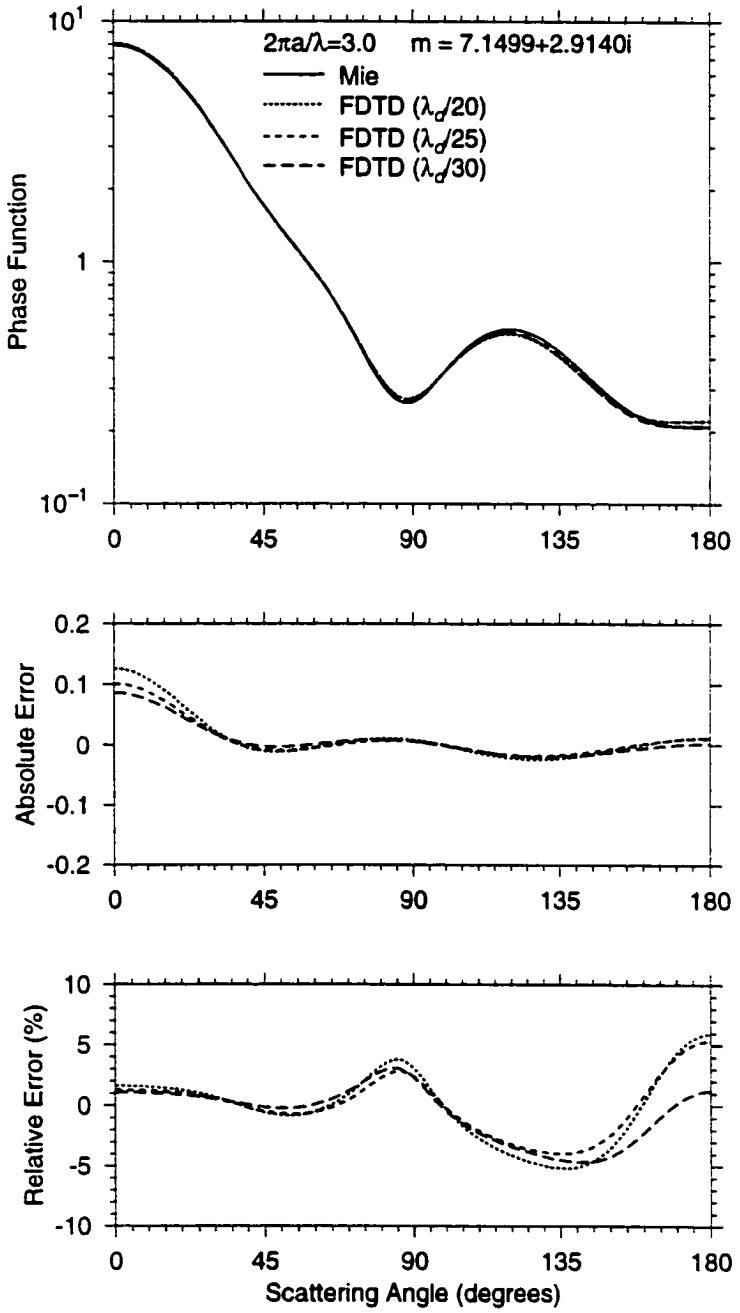

Figure 3.8: Comparison of the scattering phase functions for water spheres from Mie theory and those from the FDTD at a wavelength of 3.2 cm ($m = 7.1499 + 2.914i$) for a size parameter of 3. Different cell sizes of $\lambda_d/20$, $\lambda_d/25$ and $\lambda_d/30$ are used in the FDTD simulations where λ_d is the wavelength inside the particle.

The numerical results shown above demonstrate that the FDTD scheme with appropriate particle boundary treatments can be applied to dielectric particles with a wide range of refractive indices. However, for nonspherical particles with arbitrary composition, it is numerically difficult in the volume integration to use the gravity center interpolation by considering the exact boundary conditions. The results shown in Table 3.1 and Figs.3.2-3.4 suggest that it may be a reasonable approach to use the interpolation for the electric-displacement components at the cell center. In this way, the numerical scheme can be largely simplified. Figure 3.9 presents the comparison of scattering phase function computed from Mie theory and the FDTD method at the wavelengths of $10.8\mu m$ for ice sphere ($m = 1.0891 + 0.18216i$) and 3.2 cm for water sphere ($m = 7.1499 + 2.914i$), with the size parameters of 20 and 3, respectively. In the FDTD calculations here, we employ the interpolation for the electric displacement to the cell center. The relative errors obtained are comparable with the results presented in Fig. 2.6 and Fig. 3.6. The comparison of Mie theory and the FDTD scheme for the absorption and extinction efficiencies reveals that the relative errors are smaller than 3-4%. Therefore, the FDTD scheme using the cell center interpolation for the electric displacement, which is numerically more efficient and practical, can also obtain reliable results for dielectric particles with a large range of refractive indices.

3.4 Summary and conclusions

Numerical solutions for light scattering by dielectric particles with a wide range of refractive indices are provided using the finite-difference time domain technique, where the computational domain is truncated with a perfectly matched layer absorbing boundary condition. In this study, we have focused on the effects of numerical treatments related to the particle boundary on the FDTD results. The sensitivity study is performed for dielectric particles with different refractive indices including 1.311, $1.4717 + 0.389i$ and $5 + 2i$. The main conclusions are as follows.

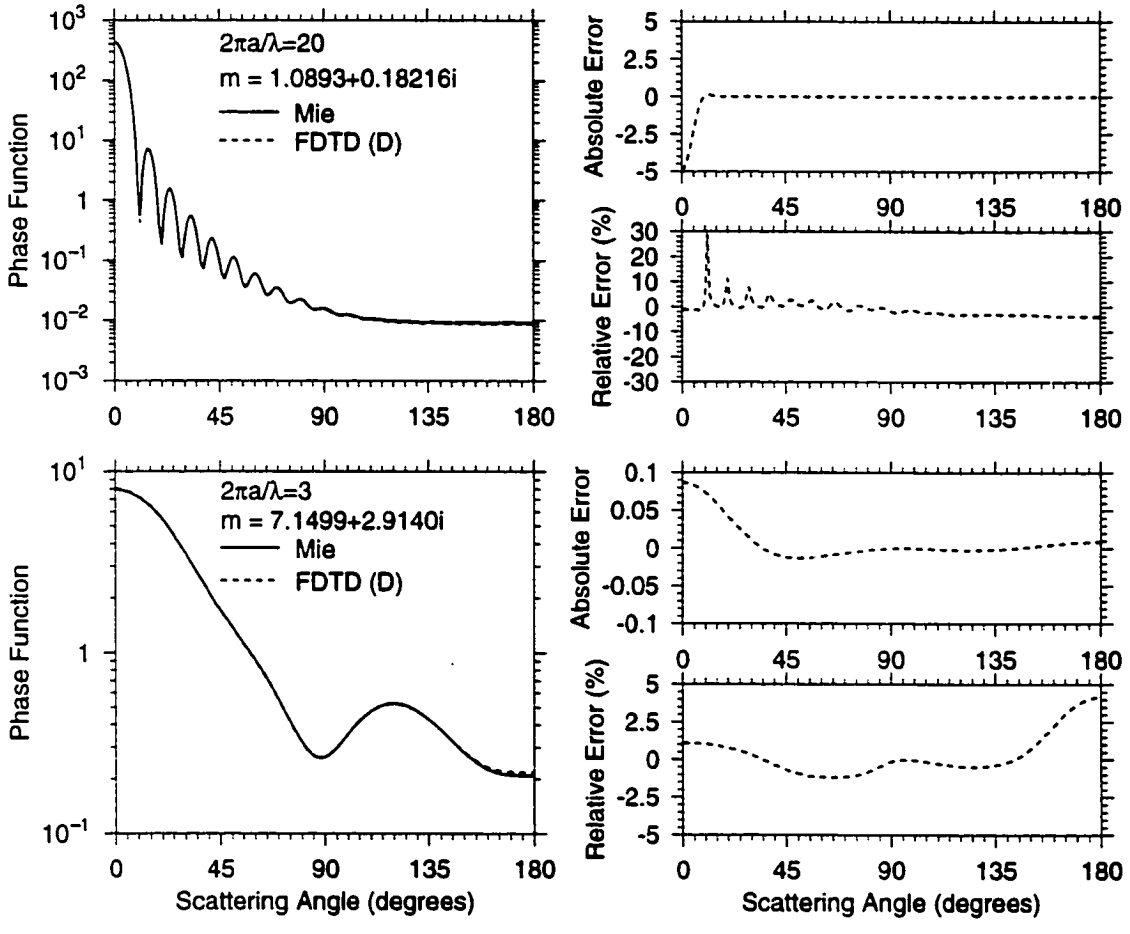

Figure 3.9: Comparison of the scattering phase functions from Mie theory and those from the FDTD at the wavelengths of $10.8\mu m$ for ice sphere ($m = 1.0891 + 0.18216i$) and 3.2 cm for water sphere ($m = 7.1499 + 2.914i$), with the size parameters of 20 and 3, respectively. A cell size of $\lambda_d/20$ is used where λ_d is the wavelength inside the particle. In the FDTD simulation, the interpolation using the electric displacement to the cell center is employed.

(1) The averaging of dielectric constant (permittivity) at grid points does not improve the accuracy of the FDTD scheme, although it would make the scheme numerically more complicated. It is recommended that the local value of the permittivity be used in the FDTD simulation.

(2) It is inappropriate to directly interpolate the electric components in the volume integration to calculate the scattering and absorption properties for dielectric particles with large refractive indices. However, reliable results can be obtained using the electric-displacement interpolation or the interpolation method based on the exact electromagnetic boundary conditions. Note that, the interpolation using the electric displacement is numerically more practical for particles with arbitrary shape and composition.

(3) The interpolation of the field components to different positions in the grid cell is also examined. Compared to the interpolation to the gravity center, the interpolation to the cell center introduces slightly more errors, but is computationally more efficient.

(4) The present FDTD scheme with appropriate treatments related to the particle boundary can be applied to dielectric particles with a wide range of refractive indices. The errors decrease with the decrease of the refractive indices.

The accuracy of the FDTD scheme, with the interpolation of the field components to the gravity center based on the exact electromagnetic boundary conditions, is examined by comparing Mie results for dielectric spheres with $m = 7.1499 + 2.914i$. The errors in the extinction and absorption efficiencies are less than ~4%. The errors in the scattering phase functions are smaller than ~5%. It is also found that similar accuracy is obtained by using the electric displacement interpolation to the grid cell center.

Chapter 4

Application of the finite-difference time domain technique to light propagation in dielectric media with particles embedded

4.1 Introduction

Most light scattering studies are related to targets surrounded by air or free space. For particles or voids embedded in absorbing media, such as particles and air bubbles in the ocean, or particles surrounded by water vapor in the atmosphere, light scattering problems must be solved in order to study ocean remote sensing or the radiative transfer in the atmosphere.

Light scattering by spherical particles or voids embedded in absorbing media was studied by Mundy *et al.* (1974), Chýlek (1977), Bohren and Gilra (1979), and Quinten and Rostalski (1996). However, there seems no report in this field for nonspherical particles. For particles or voids with arbitrary shapes embedded in dielectric media, the finite-difference time domain (FDTD) scheme (Yee 1966) may be an appropriate

method to solve the light scattering problems. The FDTD formulation in dielectric media is simply formulated as shown in Chapter 2. Another fundamental point of the FDTD is the wave source implementation in the FDTD lattice. For wave source implementation, a generic problem has been to accurately realize the physics of the source using as few electric or magnetic field components localized in the space lattice as possible, so that the additional computer storage and running time needed to simulate the source are small compared to the resources needed for the ordinary grid operations. In the context of FDTD solvers for Maxwell's equations, the incident plane wave source must meet the following essential requirements (Taflove 1995):

(1) The source should permit the numerical analog of the incident wave to enter the computational domain from what appears to be the space outside the computational domain.

(2) At any time step, the incident wave source must introduce no variations of the generated numerical plane wave across its wavefront, where the wavefront is defined as the plane perpendicular to the direction of propagation.

(3) The plane wave source should permit the numerical analog of the incident wave to have arbitrary vector-field polarization, arbitrary time-domain waveform, and arbitrary duration.

(4) The plane wave source should permit any scattered numerical waves to pass through the source locus without any hindrance or interaction, and eventually reach an infinite distance from the scatterer.

Following these requirements, in this study, we will introduce the implementation of the incident wave source conditions in dielectric media in Section 4.2. To validate the FDTD simulation, Mie theory for a spherical particle immersed in an absorbing medium is introduced in Section 4.3. We will show the numerical simulation results in Section 4.4. Summary and conclusions are given in Section 4.5.

4.2 The total-field/scattered-field formulation

Historically, there have been several methods for the plane wave source in the FDTD such as the insertion of the incident wave as an initial condition (Yee 1966), the hard source (Taflove 1975) and the total-field/scattered-field formulation (Mur 1981; Umashankar and Taflove 1982). The total-field/scattered-field formulation was the first compact plane wave source that succeeded in all aspects. This approach is based on the equivalence theorem (Schelkunoff 1943; Merewether *et al.* 1980), the linearity of Maxwell's equations, and the decomposition of the total electric and magnetic fields into incident and scattered fields. If a plane wave source is implemented on a locus within the region between the scatterer and the absorbing boundary, the interior fields will be the total fields (incident and scattered) and the fields outside the locus are only the scattered fields.

Following Taflove (1995), Fig. 4.1 illustrates the coordinates used to define the propagation direction and polarization of the incident plane wave. Using standard spherical coordinates, the incident unit wavevector $\hat{k}_{inc}$ is oriented with an angle θ relative to the $+z$-axis of the lattice (where $0^o < \theta < 180^o$), and with an angle ϕ relative to the $+x$-axis of the lattice (where $0^o \leq \phi < 360^o$). To specify the incident-wave polarization, we first define a reference vector $\hat{k}_{inc} \times \hat{z}$ in the wavefront plane (the plane of constant phase) of the incident wave. We then specify an orientation angle Ψ of the incident-electric-field vector $\vec{E}_{inc}$ relative to this reference vector (where $0^o \leq \Psi < 360^o$). This way of specifying the electric field polarization is useful for all wave incidence cases except $\theta = 0^o$ and $\theta = 180^o$, where ϕ can be used to describe the orientation of $\vec{E}_{inc}$ relative to the $+x$-axis.

Figure 4.2 shows the total-field/scattered-field interface in three dimensions which provides eight possible points of initial contact with the incident wavefront as the wavevector angles θ and ϕ are varied through their angles. As shown in Fig. 4.2, for the numerical simulation of the incident plane wave, we assume that an auxiliary one-dimensional source FDTD grid is placed along the incident wavevector so that the origin O_2 of the tatal-field/scattered-field interface coincides with one of the electric

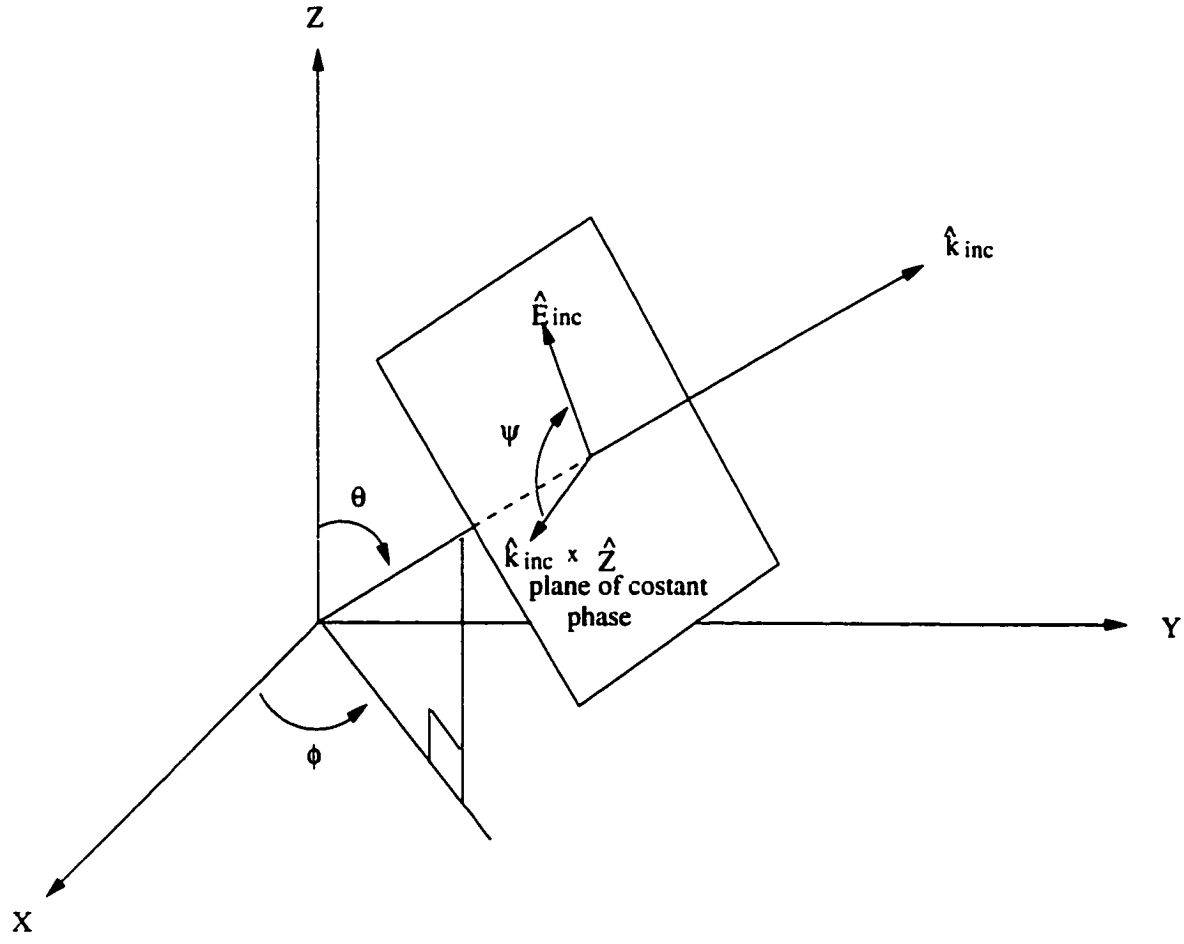

Figure 4.1: Definitions of propagation direction and polarization of incident wave (Taflove 1995)

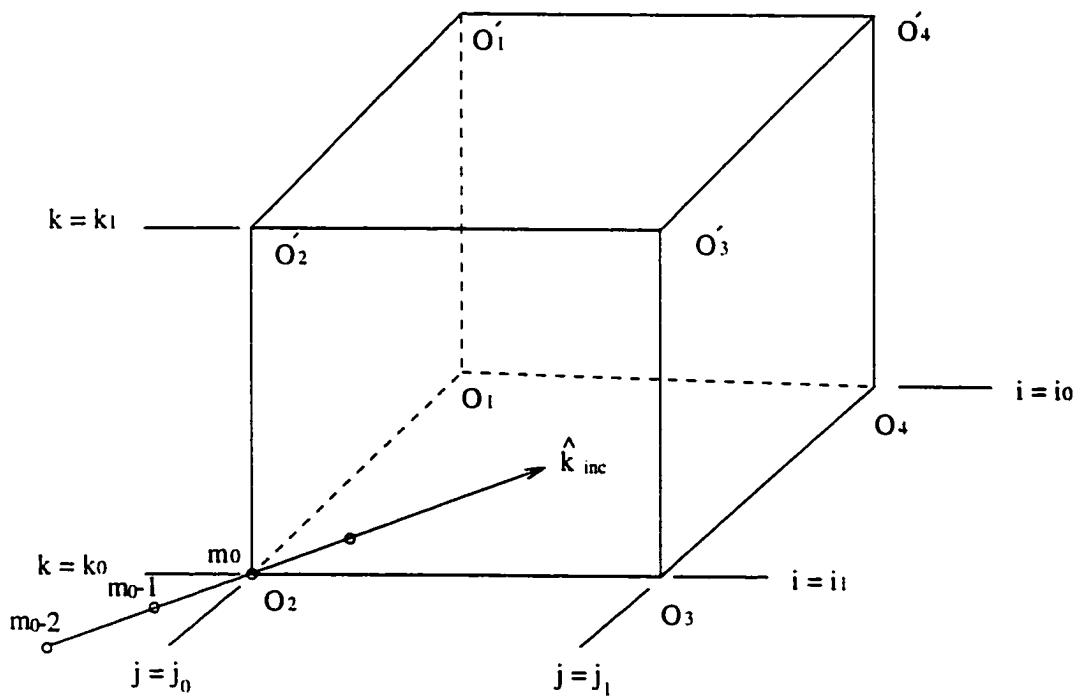

Figure 4.2: The total-field/scattered-field wave source interface for the FDTD grid. Also shown are the coordinate origins and the wavevector for calculation of incident field.

field components of the source grid $E_{inc}(m_0)$ (Taflove 1995), where m_0 denotes one grid point of the auxiliary one-dimensional source FDTD grid. The goal is to time-step the one-dimensional source grid to model the propagation of the desired incident plane wave in the given medium. Note here that the same spatial increment Δs, temporal increment Δt and time step number n as those for the main 3D FDTD grid are used for the one-dimensional source FDTD grid. With the delay distance d known for a particular location of interest in the main 3D FDTD grid. the incident field at this location can be obtained by linearly interpolating like field values adjacent to point $m_0 + d$ on the one-dimensional grid. This procedure requires computation of the incident-wave time dependence at only a single point on the source grid, i.e., at $m_0 - 2$ the hard source $E^n_{inc}(m_0 - 2) = E_0 f(n\Delta t)$, where $f(n\Delta t)$ is an arbitrary time function (Taflove 1995).

Now we consider the situation when the space in which the wave source is implemented is filled with a dielectric medium other than a free space. The system of finite-difference equations for the source grid can be derived using Eq. (2.8). The permittivity and permeability of the medium are given as $\acute{\epsilon}$ and $\acute{\mu}$, respectively. Here, we assume $\acute{\epsilon}$ has a real part $\acute{\epsilon}_r$ and an imaginary part $\acute{\epsilon}_i$. We have

$$H^{n+1/2}_{inc}(m+1/2) = H^{n-1/2}_{inc}(m+1/2) + \frac{\Delta t}{\acute{\mu}\Delta s}[E^n_{inc}(m) - E^n_{inc}(m+1), \tag{4.1a}$$

$$E^{n+1}_{inc}(m) = exp[-\acute{\tau}\Delta t]E^n_{inc}(m) + exp[-\acute{\tau}\Delta t/2]\frac{\Delta t}{\acute{\epsilon}_r \Delta s}[H^{n+1/2}_{inc}(m-1/2) - H^{n+1/2}_{inc}(m+1/2), \tag{4.1b}$$

where $\acute{\tau} = \omega\acute{\epsilon}_i/\acute{\epsilon}_r$.

In three dimensions, the interface of the total-field/scattered-field interface is composed of six flat planes forming a rectangular closed box as shown in Fig. 4.2. The

vector components of the incident wave is added to the main 3D FDTD grid points on the interface as follows (Taflove 1995). For electric fields,

$j = j_0$ face: $E_x(i = i_0 + 1/2, ..., i_1 - 1/2; j = j_0; k = k_0, ..., k_1)$

$$E_x^{n+1}(i, j_0, k) \leftarrow E_x^{n+1}(i, j_0, k) - exp[-\acute{\tau}\Delta t/2]\frac{\Delta t}{\acute{\epsilon}_r \Delta s} H_{z,inc}^{n+1/2}(i, j_0 - 1/2, k), \quad (4.2a)$$

$j = j_0$ face: $E_z(i = i_0, ..., i_1; j = j_0; k = k_0 + 1/2, ..., k_1 - 1/2)$

$$E_z^{n+1}(i, j_0, k) \leftarrow E_z^{n+1}(i, j_0, k) + exp[-\acute{\tau}\Delta t/2]\frac{\Delta t}{\acute{\epsilon}_r \Delta s} H_{x,inc}^{n+1/2}(i, j_0 - 1/2, k), \quad (4.2b)$$

$j = j_1$ face: $E_x(i = i_0 + 1/2, ..., i_1 - 1/2; j = j_1; k = k_0, ..., k_1)$

$$E_x^{n+1}(i, j_1, k) \leftarrow E_x^{n+1}(i, j_1, k) + exp[-\acute{\tau}\Delta t/2]\frac{\Delta t}{\acute{\epsilon}_r \Delta s} H_{z,inc}^{n+1/2}(i, j_1 + 1/2, k), \quad (4.2c)$$

$j = j_1$ face: $E_z(i = i_0, ..., i_1; j = j_1; k = k_0 + 1/2, ..., k_1 - 1/2)$

$$E_z^{n+1}(i, j_1, k) \leftarrow E_z^{n+1}(i, j_1, k) - exp[-\acute{\tau}\Delta t/2]\frac{\Delta t}{\acute{\epsilon}_r \Delta s} H_{x,inc}^{n+1/2}(i, j_1 + 1/2, k), \quad (4.2d)$$

$k = k_0$ face: $E_x(i = i_0 + 1/2, ..., i_1 - 1/2; j = j_0, ..., j_1; k = k_0)$

$$E_x^{n+1}(i, j, k_0) \leftarrow E_x^{n+1}(i, j, k_0) + exp[-\acute{\tau}\Delta t/2]\frac{\Delta t}{\acute{\epsilon}_r \Delta s} H_{y,inc}^{n+1/2}(i, j, k_0 - 1/2), \quad (4.2e)$$

$k = k_0$ face: $E_y(i = i_0, ..., i_1; j = j_0 + 1/2, ..., j_1 - 1/2; k = k_0)$

$$E_y^{n+1}(i, j, k_0) \leftarrow E_y^{n+1}(i, j, k_0) - exp[-\acute{\tau}\Delta t/2]\frac{\Delta t}{\acute{\epsilon}_r \Delta s} H_{x,inc}^{n+1/2}(i, j, k_0 - 1/2), \quad (4.2f)$$

$k = k_1$ face: $E_x(i = i_0 + 1/2, ..., i_1 - 1/2; j = j_0, ..., j_1; k = k_1)$

$$E_x^{n+1}(i, j, k_1) \leftarrow E_x^{n+1}(i, j, k_1) - exp[-\acute{\tau}\Delta t/2]\frac{\Delta t}{\acute{\epsilon}_r \Delta s} H_{y,inc}^{n+1/2}(i, j, k_1 + 1/2), \quad (4.2g)$$

$k = k_1$ face: $E_y(i = i_0, ..., i_1; j = j_0 + 1/2, ..., j_1 - 1/2; k = k_1)$

$$E_y^{n+1}(i, j, k_1) \leftarrow E_y^{n+1}(i, j, k_1) + exp[-\acute{\tau}\Delta t/2]\frac{\Delta t}{\acute{\epsilon}_r \Delta s} H_{x,inc}^{n+1/2}(i, j, k_1 + 1/2), \quad (4.2h)$$

$i = i_0$ face: $E_y(i = i_0; j = j_0 + 1/2, ..., j_1 - 1/2; k = k_0, ..., k_1)$

$$E_y^{n+1}(i_0, j, k) \leftarrow E_y^{n+1}(i_0, j, k) + exp[-\acute{\tau}\Delta t/2]\frac{\Delta t}{\acute{\epsilon}_r \Delta s} H_{z,inc}^{n+1/2}(i_0 - 1/2, j, k), \quad (4.2i)$$

$i = i_0$ face: $E_z(i = i_0; j = j_0, ..., j_1; k = k_0 + 1/2, ..., k_1 - 1/2)$

$$E_z^{n+1}(i_0, j, k) \leftarrow E_z^{n+1}(i_0, j, k) - exp[-\acute{\tau}\Delta t/2]\frac{\Delta t}{\acute{\epsilon}_r \Delta s} H_{y,inc}^{n+1/2}(i_0 - 1/2, j, k), \quad (4.2j)$$

$i = i_1$ face: $E_y(i = i_1; j = j_0 + 1/2, ..., j_1 - 1/2; k = k_0, ..., k_1)$

$$E_y^{n+1}(i_1, j, k) \leftarrow E_y^{n+1}(i_1, j, k) - exp[-\acute{\tau}\Delta t/2]\frac{\Delta t}{\acute{\epsilon}_r \Delta s} H_{z,inc}^{n+1/2}(i_1 + 1/2, j, k), \quad (4.2k)$$

$i = i_1$ face: $E_z(i = i_1; j = j_0, ..., j_1; k = k_0 + 1/2, ..., k_1 - 1/2)$

$$E_z^{n+1}(i_1, j, k) \leftarrow E_z^{n+1}(i_1, j, k) + exp[-\acute{\tau}\Delta t/2]\frac{\Delta t}{\acute{\epsilon}_r \Delta s} H_{y,inc}^{n+1/2}(i_1 + 1/2, j, k). \quad (4.2l)$$

The wave sources for magnetic field, located one-half grid cell outside the total-field/scattered-field interface, are implemented at the 3D FDTD magnetic field locations by

$j = j_0 - 1/2$ face: $H_z(i = i_0 + 1/2, ..., i_1 - 1/2; j = j_0 - 1/2; k = k_0, ..., k_1)$

$$H_z^{n+1/2}(i, j_0 - 1/2, k) \leftarrow H_z^{n+1/2}(i, j_0 - 1/2, k) - \frac{\Delta t}{\acute{\mu}\Delta s} E_{x,inc}^{n}(i, j_0, k), \quad (4.3a)$$

$j = j_0 - 1/2$ face: $H_x(i = i_0, ..., i_1; j = j_0 - 1/2; k = k_0 + 1/2. ...., k_1 - 1/2)$

$$H_x^{n+1/2}(i, j_0 - 1/2, k) \leftarrow H_x^{n+1/2}(i, j_0 - 1/2, k) + \frac{\Delta t}{\acute{\mu}\Delta s} E_{z,inc}^{n}(i, j_0, k), \quad (4.3b)$$

$j = j_1 + 1/2$ face: $H_z(i = i_0 + 1/2, ..., i_1 - 1/2; j = j_1 + 1/2; k = k_0, ..., k_1)$

$$H_z^{n+1/2}(i, j_1 + 1/2, k) \leftarrow H_z^{n+1/2}(i, j_1 + 1/2, k) + \frac{\Delta t}{\acute{\mu}\Delta s} E_{x,inc}^{n}(i, j_1, k), \quad (4.3c)$$

$j = j_1 + 1/2$ face: $H_x(i = i_0, ..., i_1; j = j_1 + 1/2; k = k_0 + 1/2. ...., k_1 - 1/2)$

$$H_x^{n+1/2}(i, j_1 + 1/2, k) \leftarrow H_x^{n+1/2}(i, j_1 + 1/2, k) - \frac{\Delta t}{\acute{\mu}\Delta s} E_{z,inc}^{n}(i, j_1, k), \quad (4.3d)$$

$k = k_0 - 1/2$ face: $H_y(i = i_0 + 1/2, ..., i_1 - 1/2; j = j_0, ..., j_1; k = k_0 - 1/2)$

$$H_y^{n+1/2}(i, j, k_0 - 1/2) \leftarrow H_y^{n+1/2}(i, j, k_0 - 1/2) + \frac{\Delta t}{\acute{\mu}\Delta s} E_{x,inc}^{n}(i, j, k_0), \quad (4.3e)$$

$k = k_0 - 1/2$ face: $H_x(i = i_0, ..., i_1; j = j_0 + 1/2, ..., j_1 - 1/2; k = k_0 - 1/2)$

$$H_x^{n+1/2}(i, j, k_0 - 1/2) \leftarrow H_x^{n+1/2}(i, j, k_0 - 1/2) - \frac{\Delta t}{\acute{\mu}\Delta s} E_{y,inc}^{n}(i, j, k_0), \quad (4.3f)$$

$k = k_1 + 1/2$ face: $H_y(i = i_0 + 1/2, ..., i_1 - 1/2; j = j_0, ..., j_1; k = k_1 + 1/2)$

$$H_y^{n+1/2}(i, j, k_1 + 1/2) \leftarrow H_y^{n+1/2}(i, j, k_1 + 1/2) - \frac{\Delta t}{\acute{\mu}\Delta s} E_{x,inc}^n(i, j, k_1), \tag{4.3g}$$

$k = k_1 + 1/2$ face: $H_x(i = i_0, ..., i_1; j = j_0 + 1/2, ..., j_1 - 1/2; k = k_1 + 1/2)$

$$H_x^{n+1/2}(i, j, k_1 + 1/2) \leftarrow H_x^{n+1/2}(i, j, k_1 + 1/2) + \frac{\Delta t}{\acute{\mu}\Delta s} E_{y,inc}^n(i, j, k_1), \tag{4.3h}$$

$i = i_0 - 1/2$ face: $H_z(i = i_0 - 1/2; j = j_0 + 1/2, ..., j_1 - 1/2; k = k_0, ..., k_1)$

$$H_z^{n+1/2}(i_0 - 1/2, j, k) \leftarrow H_z^{n+1/2}(i_0 - 1/2, j, k) + \frac{\Delta t}{\acute{\mu}\Delta s} E_{y,inc}^n(i_0, j, k), \tag{4.3i}$$

$i = i_0 - 1/2$ face: $H_y(i = i_0 - 1/2; j = j_0, ..., j_1; k = k_0 + 1/2, ..., k_1 - 1/2)$

$$H_y^{n+1/2}(i_0 - 1/2, j, k) \leftarrow H_y^{n+1/2}(i_0 - 1/2, j, k) - \frac{\Delta t}{\acute{\mu}\Delta s} E_{z,inc}^n(i_0, j, k), \tag{4.3j}$$

$i = i_1 + 1/2$ face: $H_z(i = i_1 + 1/2; j = j_0 + 1/2, ..., j_1 - 1/2; k = k_0, ..., k_1)$

$$H_z^{n+1/2}(i_1 + 1/2, j, k) \leftarrow H_z^{n+1/2}(i_1 + 1/2, j, k) - \frac{\Delta t}{\acute{\mu}\Delta s} E_{y,inc}^n(i_1, j, k), \tag{4.3k}$$

$i = i_1 + 1/2$ face: $H_y(i = i_1 + 1/2; j = j_0, ..., j_1; k = k_0 + 1/2, ..., k_1 - 1/2)$

$$H_y^{n+1/2}(i_1 + 1/2, j, k) \leftarrow H_y^{n+1/2}(i_1 + 1/2, j, k) + \frac{\Delta t}{\acute{\mu}\Delta s} E_{z,inc}^n(i_1, j, k). \tag{4.3l}$$

Note here that the "$\leftarrow$" in Eqs. (4.2) and (4.3) denotes the assignment of the values at its right side to the field components at its left side on the total-field/scattered-field interface in the FDTD computational domain.

The delay distance d for a location in the main computational domain is given by

$$d = \hat{k}_{inc} . \vec{r}_{comp}, \tag{4.4}$$

where $\hat{k}_{inc}$ is the unit incident wavevector given by

$$\hat{k}_{inc} = \hat{x} sin\theta cos\phi + \hat{y} sin\theta sin\phi + \hat{z} cos\theta. \tag{4.5}$$

and $\vec{r}_{comp}$ is the position vector from the appropriate origin to the field vector component of interest.

For $0^o < \theta \leq 90^o$, origins O_1, O_2, O_3 and O_4 in Fig. 4.1 are the points of the total-field/scattered-field interface that can make initial contact with the incident wavefront. For this angle of θ, we have the following possibilities for $\vec{r}_{comp}$:

(1) $0^o \leq \phi \leq 90^o$. Origin O_1 at (i_0, j_0, k_0)

$$\vec{r}_{comp} = \hat{x}(i_{comp} - i_0) + \hat{y}(j_{comp} - j_0) + \hat{z}(k_{comp} - k_0), \tag{4.6a}$$

(2) $90^o < \phi \leq 180^o$. Origin O_2 at (i_1, j_0, k_0)

$$\vec{r}_{comp} = \hat{x}(i_{comp} - i_1) + \hat{y}(j_{comp} - j_0) + \hat{z}(k_{comp} - k_0), \tag{4.6b}$$

(3) $180^o < \phi \leq 270^o$. Origin O_3 at (i_1, j_1, k_0)

$$\vec{r}_{comp} = \hat{x}(i_{comp} - i_1) + \hat{y}(j_{comp} - j_1) + \hat{z}(k_{comp} - k_0), \tag{4.6c}$$

(4) $270^o < \phi \leq 360^o$. Origin O_4 at (i_0, j_1, k_0)

$$\vec{r}_{comp} = \hat{x}(i_{comp} - i_0) + \hat{y}(j_{comp} - j_1) + \hat{z}(k_{comp} - k_0). \tag{4.6d}$$

For $90^o < \theta < 180^o$, origins $\acute{O}_1$, $\acute{O}_2$, $\acute{O}_3$ and $\acute{O}_4$ in Fig. 4.1 are the points of the total-field/scattered-field interface that can make initial contact with the incident wavefront. For this angle of θ, we have the following possibilities for $\vec{r}_{comp}$:

(5) $0^o \leq \phi \leq 90^o$. Origin $\acute{O}_1$ at (i_0, j_0, k_1)

$$\vec{r}_{comp} = \hat{x}(i_{comp} - i_0) + \hat{y}(j_{comp} - j_0) + \hat{z}(k_{comp} - k_1), \tag{4.6e}$$

(6) $90^o < \phi \leq 180^o$. Origin $\acute{O}_2$ at (i_1, j_0, k_1)

$$\vec{r}_{comp} = \hat{x}(i_{comp} - i_1) + \hat{y}(j_{comp} - j_0) + \hat{z}(k_{comp} - k_1), \tag{4.6f}$$

(7) $180^o < \phi \leq 270^o$. Origin $\acute{O}_3$ at (i_1, j_1, k_1)

$$\vec{r}_{comp} = \hat{x}(i_{comp} - i_1) + \hat{y}(j_{comp} - j_1) + \hat{z}(k_{comp} - k_1), \tag{4.6g}$$

(8) $270^o < \phi \leq 360^o$. Origin O_4 at (i_0, j_1, k_1)

$$\vec{r}_{comp} = \hat{x}(i_{comp} - i_0) + \hat{y}(j_{comp} - j_1) + \hat{z}(k_{comp} - k_1). \tag{4.6h}$$

Given the delay distance d and the source grid FDTD values, the incident-field values $E_{inc}|^n$ and $H_{inc}|^{n+1/2}$ at a given location can be obtained by linear interpolation of the like field values adjacent to point $m_0 + d$ on the one-dimensional grid. The required vector components of the incident field can then be obtained using

$$H_{x,inc}^{n+1/2} = H_{inc}^{n+1/2}(sin\Psi sin\phi + cos\Psi cos\theta cos\phi), \tag{4.7a}$$

$$H_{y,inc}^{n+1/2} = H_{inc}^{n+1/2}(-sin\Psi cos\phi + cos\Psi cos\theta sin\phi), \tag{4.7b}$$

$$H_{z,inc}^{n+1/2} = H_{inc}^{n+1/2}(-cos\Psi sin\theta), \tag{4.7c}$$

$$E_{x,inc}^{n} = E_{inc}^{n}(cos\Psi sin\phi - sin\Psi cos\theta cos\phi). \tag{4.7d}$$

$$E_{y,inc}^{n} = E_{inc}^{n}(-cos\Psi cos\phi - sin\Psi cos\theta sin\phi). \tag{4.7e}$$

$$E_{z,inc}^{n} = E_{inc}^{n}(sin\Psi sin\theta), \tag{4.7f}$$

where $H_{inc}^{n+1/2}$ and E_{inc}^{n} are the interpolated magnetic and electric fields at that given location, respectively.

It is noted here that if the medium in which the wave source condition is implemented, is free space, all the formulae discussed in this chapter should go back to those documented in Taflove (1995).

4.3 Mie theory for light scattering by spheres in absorbing media

In order to provide validation for the FDTD simulation of electromagnetic wave propagation in absorbing dielectric media with particles embedded, we will briefly introduce Mie theory for light scattering by spherical particles in an absorbing medium in this section

Light scattering by particles immersed in an absorbing host medium has already been solved by different authors in far field (Mundy *et al.* 1974; Chýlek 1977; Bohren and Gilra 1979). However, the absorption in the host medium restricts the solution of the problem either to very weakly absorbing media or to finite distance from the encapsulated particle (Quinten and Rostalski 1996). And due to the absorption in the host medium, the extinction cross-section and absorption cross-section depend on the radius of the conceptual integrating sphere around the scatterer. Therefore the extinction and absorption efficiencies calculated in the far-field region cannot represent the scattering and absorption by the scatterer only. To avoid this problem, Quinten and Rostalski (1996) derived a solution which generalizes the far-field solutions on arbitrary sizes of the conceptual integrating sphere around the scatterer. In particular, they considered the $\vec{E}_i \times \vec{H}_i^*$ term in the definition of extinction as suggested by Chýlek (1977), which was overlooked in Mundy *et al.*(1974). Here $\vec{E}_i$ and $\vec{H}_i$ are incident electric and magnetic vectors, respectively. In this study, we derive the expressions for light scattering by spheres immersed in absorbing media using near fields.

The problem with which we are concerned is scattering of a plane x-polarized wave by an sphere with a radius of a immersed in an absorbing medium. In spherical coordinates (Fig. 4.3), the incident (i), internal (t) and scattered (s) fields can be expressed in spherical harmonics as (Bohren and Huffman 1983)

$$\vec{E}_i = \sum_{n=1}^{\infty} E_n(\vec{M}_{oln}^{(1)} - i\vec{N}_{eln}^{(1)}), \tag{4.8a}$$

$$\vec{H}_i = \frac{-k}{\omega\mu} \sum_{n=1}^{\infty} E_n(\vec{M}_{eln}^{(1)} + i\vec{N}_{oln}^{(1)}), \tag{4.8b}$$

$$\vec{E}_t = \sum_{n=1}^{\infty} E_n(c_n\vec{M}_{oln}^{(1)} - id_n\vec{N}_{eln}^{(1)}), \tag{4.9a}$$

$$\vec{H}_t = \frac{-k_t}{\omega\mu_t} \sum_{n=1}^{\infty} E_n(d_n\vec{M}_{eln}^{(1)} + ic_n\vec{N}_{oln}^{(1)}), \tag{4.9b}$$

$$\vec{E}_s = \sum_{n=1}^{\infty} E_n(ia_n\vec{N}_{eln}^{(3)} - b_n\vec{M}_{oln}^{(3)}), \tag{4.10a}$$

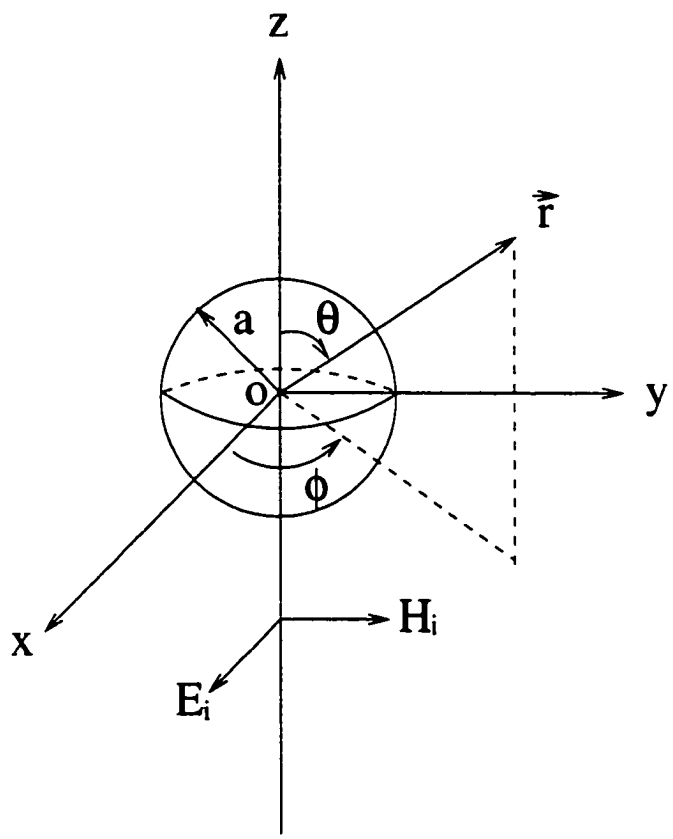

Figure 4.3: Geometry of x-polarized light incident on a spherical particle of radius a. The origin of the spherical polar coordinate system is at the particle center. The direction of scattered light is defined by angles θ and ϕ.

$$\vec{H}_s = \frac{k}{\omega\mu}\sum_{n=1}^{\infty} E_n(ib_n\vec{N}_{oln}^{(3)} + a_n\vec{M}_{eln}^{(3)}), \tag{4.10b}$$

where $E_n = i^n E_0(2n+1)/(n(n+1))$ with E_0 as the amplitude of the incident electric field at the origin of the coordinate system when the particle is removed; ω is the angular frequency; k and k_t are complex wavenumbers in the host medium and inside the scatterer, respectively; μ and μ_t are the permeabilities of the host medium and the scatterer, respectively.

The vector spherical harmonics in Eqs.(4.8)-(4.10) can be expressed in a form:

$$\vec{M}_{oln} = cos\phi\pi_n(cos\theta)z_n(\rho)\hat{e}_\theta - sin\phi\tau_n(cos\theta)z_n(\rho)\hat{e}_\phi, \tag{4.11a}$$

$$\vec{M}_{eln} = -sin\phi\pi_n(cos\theta)z_n(\rho)\hat{e}_\theta - cos\phi\tau_n(cos\theta)z_n(\rho)\hat{e}_\phi, \tag{4.11b}$$

$$\vec{N}_{oln} = sin\phi n(n+1)sin\theta\pi_n(cos\theta)\frac{z_n(\rho)}{\rho}\hat{e}_r +$$

$$sin\phi\tau_n(cos\theta)\frac{[\rho z_n(\rho)]'}{\rho}\hat{e}_\theta + cos\phi\pi_n(cos\theta)\frac{[\rho z_n(\rho)]'}{\rho}\hat{e}_\phi, \tag{4.11c}$$

$$\vec{N}_{eln} = cos\phi n(n+1)sin\theta\pi_n(cos\theta)\frac{z_n(\rho)}{\rho}\hat{e}_r +$$

$$cos\phi\tau_n(cos\theta)\frac{[\rho z_n(\rho)]'}{\rho}\hat{e}_\theta - sin\phi\pi_n(cos\theta)\frac{[\rho z_n(\rho)]'}{\rho}\hat{e}_\phi, \tag{4.11d}$$

where ρ denotes kr or $k_t r$, corresponding to the fields outside or inside the scatterer, respectively. Superscripts appended to $\vec{M}$ and $\vec{N}$ in Eqs.(4.8)-(4.10) denote the kind of spherical Bessel function z_n: $^{(1)}$ denotes $j_n(kr)$ or $j_n(k_t r)$, which is spherical Bessel function; and $^{(3)}$ denotes $h_n^{(1)}(kr)$, which is spherical Hankel function. The angle-dependent functions $\pi_n = P_n^1/sin\theta$ and $\tau_n = dP_n^1/d\theta$, where P_n^1 is the associated Legendre polynomial, can be computed by upward recurrence (Bohren and Huffman 1983).

Using the boundary conditions at the particle-medium interface ($E_{i\theta} + E_{s\theta} = E_{t\theta}$, $H_{i\theta} + H_{s\theta} = H_{t\theta}$; or $E_{i\phi} + E_{s\phi} = E_{t\phi}$, $H_{i\phi} + H_{s\phi} = H_{t\phi}$, at $r = a$), we can finally solve out a_n, b_n, c_n and d_n in the form:

$$a_n = \frac{m_t\psi_n'(\alpha)\psi_n(\beta) - m\psi_n(\alpha)\psi_n'(\beta)}{m_t\xi_n'(\alpha)\psi_n(\beta) - m\xi_n(\alpha)\psi_n'(\beta)}, \tag{4.12a}$$

$$b_n = \frac{m_t\psi_n(\alpha)\psi_n'(\beta) - m\psi_n'(\alpha)\psi_n(\beta)}{m_t\xi_n(\alpha)\psi_n'(\beta) - m\xi_n'(\alpha)\psi_n(\beta)}, \tag{4.12b}$$

$$c_n = \frac{m_t\xi_n(\alpha)\psi_n'(\alpha) - m_t\xi_n'(\alpha)\psi_n(\alpha)}{m_t\xi_n(\alpha)\psi_n'(\beta) - m\xi_n'(\alpha)\psi_n(\beta)}. \tag{4.12c}$$

$$d_n = \frac{m_t\xi_n'(\alpha)\psi_n(\alpha) - m_t\xi_n(\alpha)\psi_n'(\alpha)}{m_t\xi_n'(\alpha)\psi_n(\beta) - m\xi_n(\alpha)\psi_n'(\beta)}, \tag{4.12d}$$

where m_t and m are the complex refractive indices of the scatterer and the host medium, respectively; $\alpha = mx$, $\beta = m_t x$, and $x = 2\pi a/\lambda_0$, with λ_0 as the wavelength in free space; Riccati-Bessel functions $\psi_n(\rho) = \rho j_n(\rho)$ and $\xi_n(\rho) = \rho h_n^{(1)}(\rho)$.

Once a_n, b_n, c_n and d_n are obtained, the internal and scattered fields can be calculated simply by using Eqs.(4.9)-(4.11).

If the host medium is nonabsorbing, the far-field approximation for the electromagnetic field is usually used to calculate scattering and extinction cross-sections. However, for an absorbing host medium, it is not suitable to calculate the scattering and extinction efficiencies in the far field. In this study, we derive the scattering and absorption efficiencies of a sphere embedded in an absorbing host medium by using the exact near-field expressions. Here the conceptual integrating sphere is simply the surface of the scatterer. It is shown that the scattered energy W_s and the energy absorbed by the scatterer W_a are given by

$$W_s = \frac{1}{2}Re\int\int_s (\vec{E}_s \times \vec{H}_s^*).\hat{n}ds$$

$$= \frac{\pi|E_0|^2}{c\mu(2\pi/\lambda_o)^2}\sum_{n=1}^{\infty}(2n+1)Im(\frac{|a_n|^2\xi_n'\xi_n^* - |b_n|^2\xi_n\xi_n'^*}{m}), \tag{4.13}$$

$$W_a = -\frac{1}{2}Re\int\int_s (\vec{E}_t \times \vec{H}_t^*).\hat{n}ds$$

$$= \frac{\pi|E_0|^2}{c\mu_t(2\pi/\lambda_o)^2}\sum_{n=1}^{\infty}(2n+1)Im(\frac{|c_n|^2\psi_n\psi_n'^* - |d_n|^2\psi_n'\psi_n^*}{m_t}), \tag{4.14}$$

where the integral is taken over the surface s of the scatterer; $\hat{n}$ is an outward unit vector normal to the surface of the scatterer; c is the wave speed in vacuum; $\xi_n = \xi_n(mx)$ and $\psi_n = \psi_n(m_t x)$. In the derivation of Eqs.(4.13) and (4.14), we have used Eqs.(4.9)-(4.11) and we have used Eq.(4.24) in Bohren and Huffman (1983) and the relation

$$\int_0^{\pi} (\pi_n \pi_m + \tau_n \tau_m) sin\theta d\theta = \delta_{nm} \frac{2n^2(n+1)^2}{2n+1}. \tag{4.15}$$

Following Mundy *et al.* (1974), the mean energy flow incident on the scatterer is

$$\begin{aligned} I &= \frac{2\pi a^2}{(4\pi a m_i/\lambda_0)^2} I_0[1 + (4\pi a m_i/\lambda_0 - 1)exp(4\pi a m_i/\lambda_0)] \\ &= \frac{2\pi a^2}{(4\pi a m_i/\lambda_0)^2} \frac{m_r}{2c\mu} |E_0|^2 [1 + (4\pi a m_i/\lambda_0 - 1)exp(4\pi a m_i/\lambda_0)], \end{aligned} \tag{4.16}$$

where m_r and m_i are the real and imaginary parts of the complex refractive index m of the host medium.

The scattering and absorption efficiencies are $Q_s = W_s/I$ and $Q_a = W_a/I$, respectively. Therefore, the extinction efficiency is $Q_e = Q_s + Q_a$.

The extinction can also be calculated using the fields outside the particle. Following Chýlek (1977), the extinction energy is given by

$$W_e = -\frac{1}{2} Re \int\int_s (\vec{E}_i \times \vec{H}_i^* + \vec{E}_i \times \vec{H}_s^* + \vec{E}_s \times \vec{H}_i^*).\hat{n} ds. \tag{4.17}$$

Similar to the derivation of Eqs.(4.13) and (4.14), we can obtain

$$\begin{aligned} W_e = &\frac{\pi |E_0|^2}{c\mu(2\pi/\lambda_o)^2} \sum_{n=1}^{\infty} (2n+1) Im(\frac{\psi_n \psi_n'^* - \psi_n' \psi_n^*}{m}) + \\ &\frac{\pi |E_0|^2}{c\mu(2\pi/\lambda_o)^2} \sum_{n=1}^{\infty} (2n+1) Im(\frac{a_n^* \xi_n^* \psi_n' + a_n \xi_n' \psi_n^* - b_n \xi_n \psi_n'^* - b_n^* \xi_n'^* \psi_n}{m}), \end{aligned} \tag{4.18}$$

where $\xi_n = \xi_n(mx)$ and $\psi_n = \psi_n(mx)$. The first term in last equation corresponds

to the $\vec{E}_i \times \vec{H}_i^*$ term in Eq.(4.17). This term is not zero even when the conceptual integrating sphere is the surface of the scatterer. Our numerical experiment shows that, for the calculation of extinction efficiency, there is no difference between the method using Eq.(4.18) and that using Eqs.(4.13) and (4.14).

In this study, we define the amplitude functions s_1 and s_2 following Kerker (1969) in the form

$$s_1 = \sum_{n=1}^{\infty} \frac{2n+1}{n(n+1)}[a_n \pi_n(cos\theta) + b_n \tau_n(cos\theta)], \tag{4.19a}$$

$$s_2 = \sum_{n=1}^{\infty} \frac{2n+1}{n(n+1)}[a_n \tau_n(cos\theta) + b_n \pi_n(cos\theta)]. \tag{4.19b}$$

For unpolarized incident light, the normalized scattering phase function can be derived in a form

$$P(cos\theta) = \frac{|s_1|^2 + |s_2|^2}{\sum_{n=1}^{\infty}(2n+1)(|a_n|^2 + |b_n|^2)}. \tag{4.20}$$

Another frequently used parameter in the radiative transfer calculation is the asymmetry factor which is defined as

$$g = \frac{1}{2}\int_{-1}^{1} P(cos\theta) cos\theta dcos\theta. \tag{4.21}$$

Using Eq.(4.20), the asymmetry factor can be expressed in an analytic form

$$g = \frac{2\sum_{n=1}^{\infty}[\frac{n(n+2)}{n+1} Re(a_n a_{n+1}^* + b_n b_{n+1}^*) + \frac{2n+1}{n(n+1)} Re(a_n b_n^*)]}{\sum_{n=1}^{\infty}(2n+1)(|a_n|^2 + |b_n|^2)}. \tag{4.22}$$

4.4 Numerical results

In the FDTD simulation, the computational domain is still terminated with the perfectly matched layer (PML) absorbing boundary condition (ABC). Because the medium between the particle and the PML is not free space here, the PML which has an impedance of free space does not match the medium perfectly. Therefore,

there may be some numerical reflection happening at the medium-PML interface. However, when the total field/scattered field FDTD formulation is used, together with the absorption of the scattered light by the surrounding medium, the scattered waves arriving at the medium-PML interface is weak, and thus the reflection at the medium-PML interface due to the imperfect match should not be significant. So it is expected that using the PML in this case would still give a good simulation, though more errors are involved.

Figure 4.4 shows the energy density within a spherical air bubble simulated using the FDTD technique. The air bubble is submerged in an infinite dielectric medium with a refractive index of $1.0893 + 0.18216i$. The size parameter of the air bubble is 6. The incident direction is along the -x direction. Only the energy density on a plane crossing the center of the sphere is shown. The incident electric field is linearly polarized in the direction perpendicular to the plane. The result is normalized by the incident field at the location of the bubble center when the bubble is removed from the medium. In the FDTD calculation, a grid cell size of $\lambda/60$ is used, where λ is the incident wavelength in free space. The exact result for this case calculated by Mie theory is shown in Fig. 4.5. We can see that the interference pattern inside the air bubble simulated by the FDTD technique is very close to the exact result. However, comparing the pattern in Fig. 4.4 with that shown in Fig. 4.5, we can see that the FDTD has some numerical errors at the bubble boundary, particularly at the part facing the incident wave.

Figure 4.6 illustrates the extinction, scattering, and absorption efficiencies and asymmetry factors as functions of size parameters calculated by Mie theory for spherical particles immersed in a host medium. A refractive index of 1.4 + 0.05i is used for the particles. The real refractive index of the medium is 1.2, and the imaginary refractive index of the medium is 0.0, 0.001, 0.01 and 0.05. We can see that, with the increase of absorption in the host medium, both the extinction efficiency and scattering efficiency decrease significantly, but absorption efficiency decreases little. For large size parameters, the scattering efficiency can be reduced to zero, which means

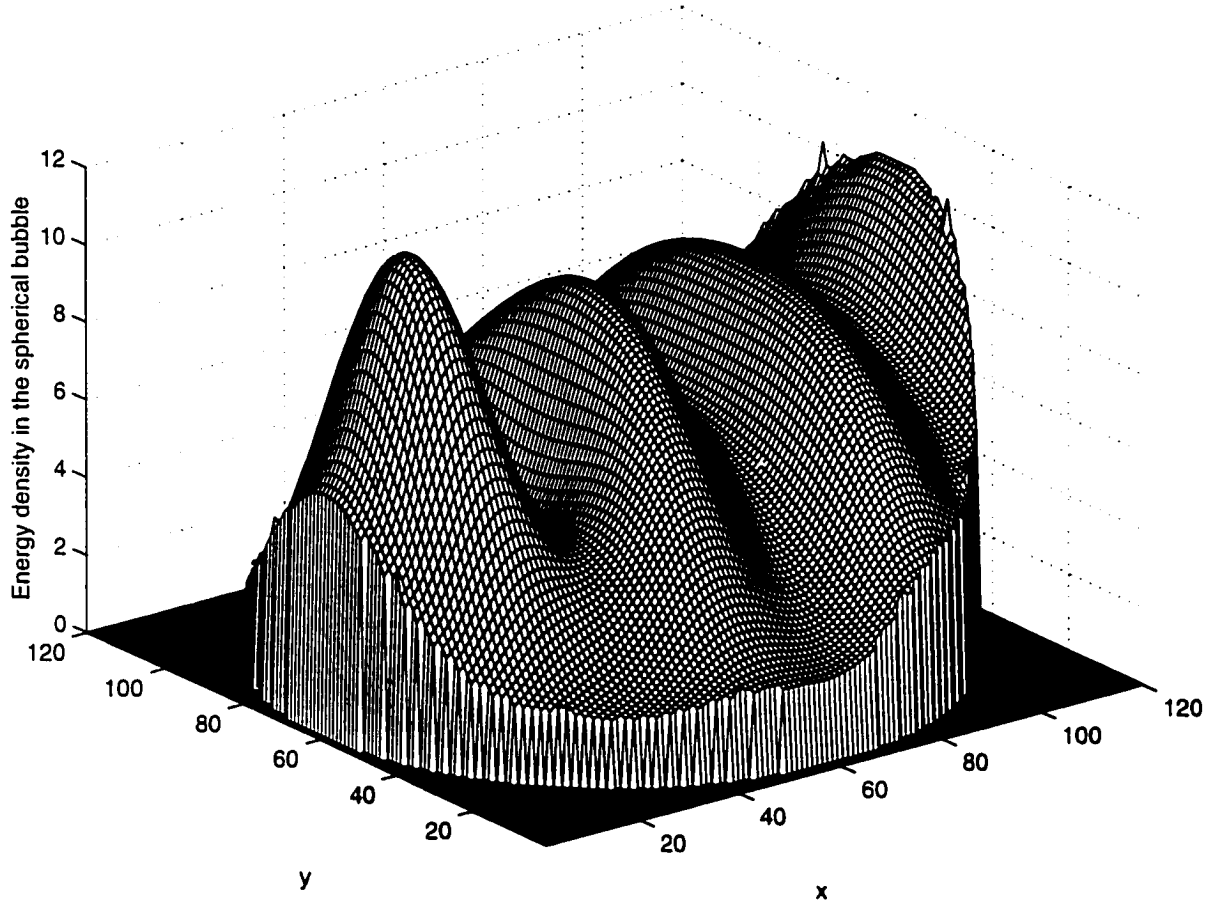

Figure 4.4: Electric energy density within a spherical air bubble simulated using the FDTD technique. The air bubble is submerged in an infinite dielectric medium with a refractive index of $1.0891 + 0.18216i$. The size parameter of the air bubble is 6.The light is incident along $-x$ direction. The incident electric field is polarized in z direction.

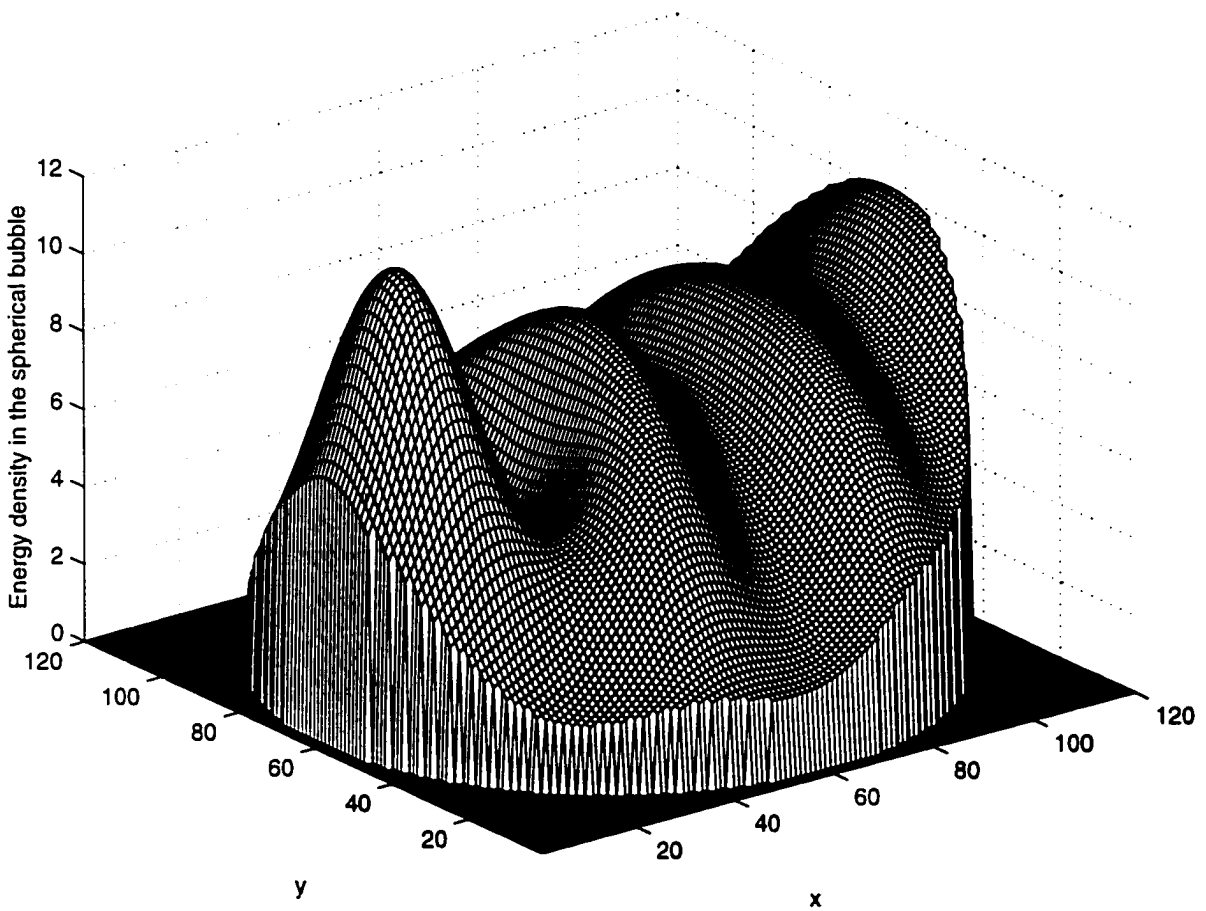

Figure 4.5: Same as Fig.4.4, but for electric energy density within a spherical air bubble simulated using Mie theory.

that the extinction by the particle is solely due to the absorption, which is close to one for large size parameters. For size parameters smaller than 10, the asymmetry factors change very little. However, when size parameter is larger than 10, the asymmetry factors decrease dramatically with the increase of absorption in the host medium.

Figure 4.7 shows the scattering phase function versus scattering angle for spheres with a refractive index of 1.4 + 0.05i, immersed in a medium with a real refractive of 1.2 and an imaginary refractive index of 0.0, 0.001, 0.01 and 0.05. The size parameters are 5, 25. and 100. We can see that, with the increase of the imaginary refractive index of the host medium, for small size parameters, the phase function has little change; however, for large size parameters, the forward scattering decreases and the backward scattering increases dramatically.

4.5 Summary and conclusions

For the applications of the FDTD technique to the study of light scattering and propagation in dielectric media with embedded particles, we have extended the implementation of the incident wave source conditions in the FDTD to general surrounding dielectric media. A numerical simulation result is shown. This extension makes the FDTD suitable for the solution of light scattering and propagation problems when the scatterer is embedded in surrounding dielectric media as well as in free space. However, when the surrounding medium is no longer air or free space, one cannot use the volume integration method to calculate scattering properties. Using the surface integration in the near field to calculate the scattering properties is difficult by using the electric fields from the numerical model. Therefore, only internal field and absorption can be calculated at current time by using the FDTD for particles immersed in a dielectric medium.

Here in order to provide validation for the FDTD simulation. exact solution for light scattering by spherical particles immersed in absorbing media is developed in this study. The internal field is calculated and compared with the FDTD simulation.

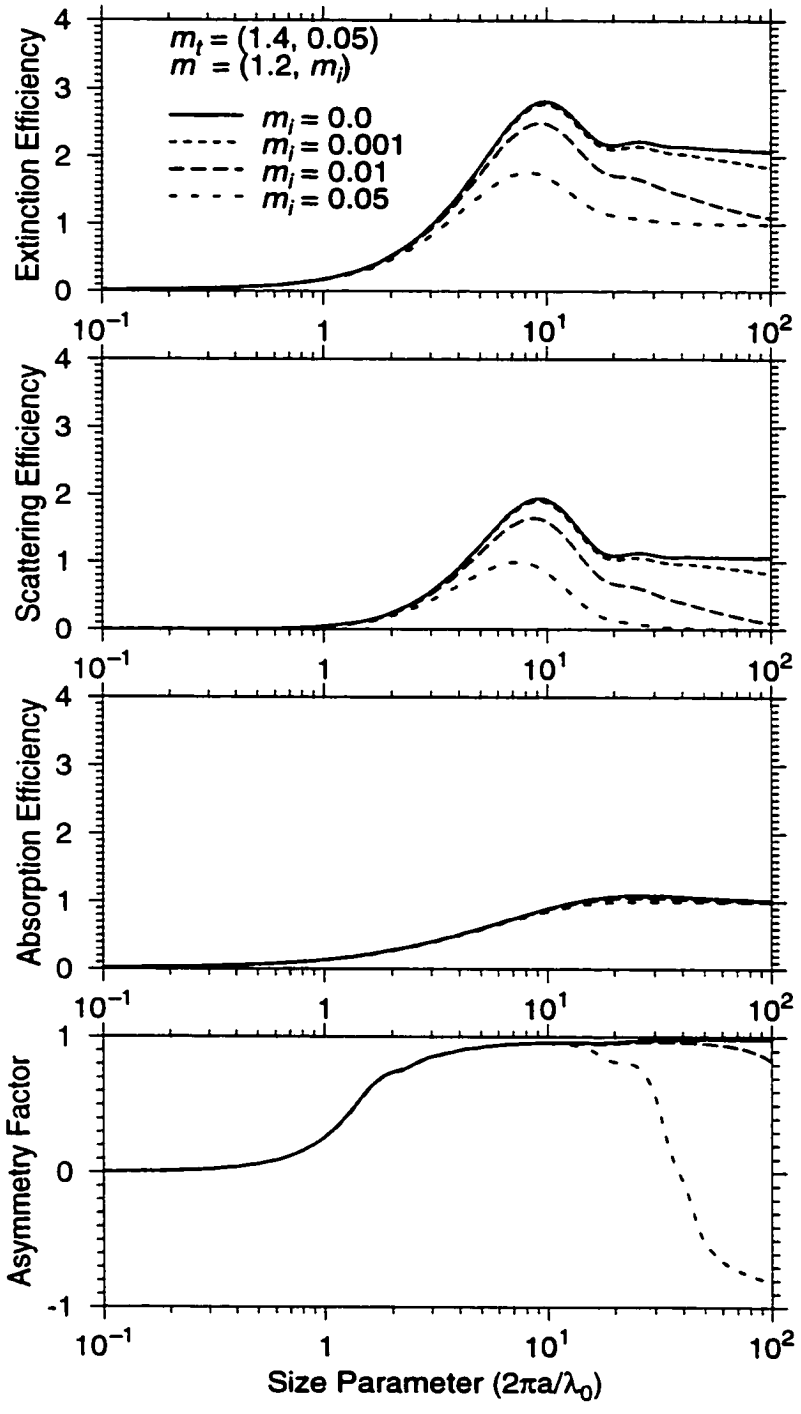

Figure 4.6: Extinction, scattering, and absorption efficiencies and asymmetry factors as functions of size parameters for spherical particles immersed in a medium. A refractive index of 1.4 + 0.05i is used for the particles. The real refractive index of the medium is 1.2, and the imaginary refractive index of the medium is 0.0, 0.001, 0.01 and 0.05.

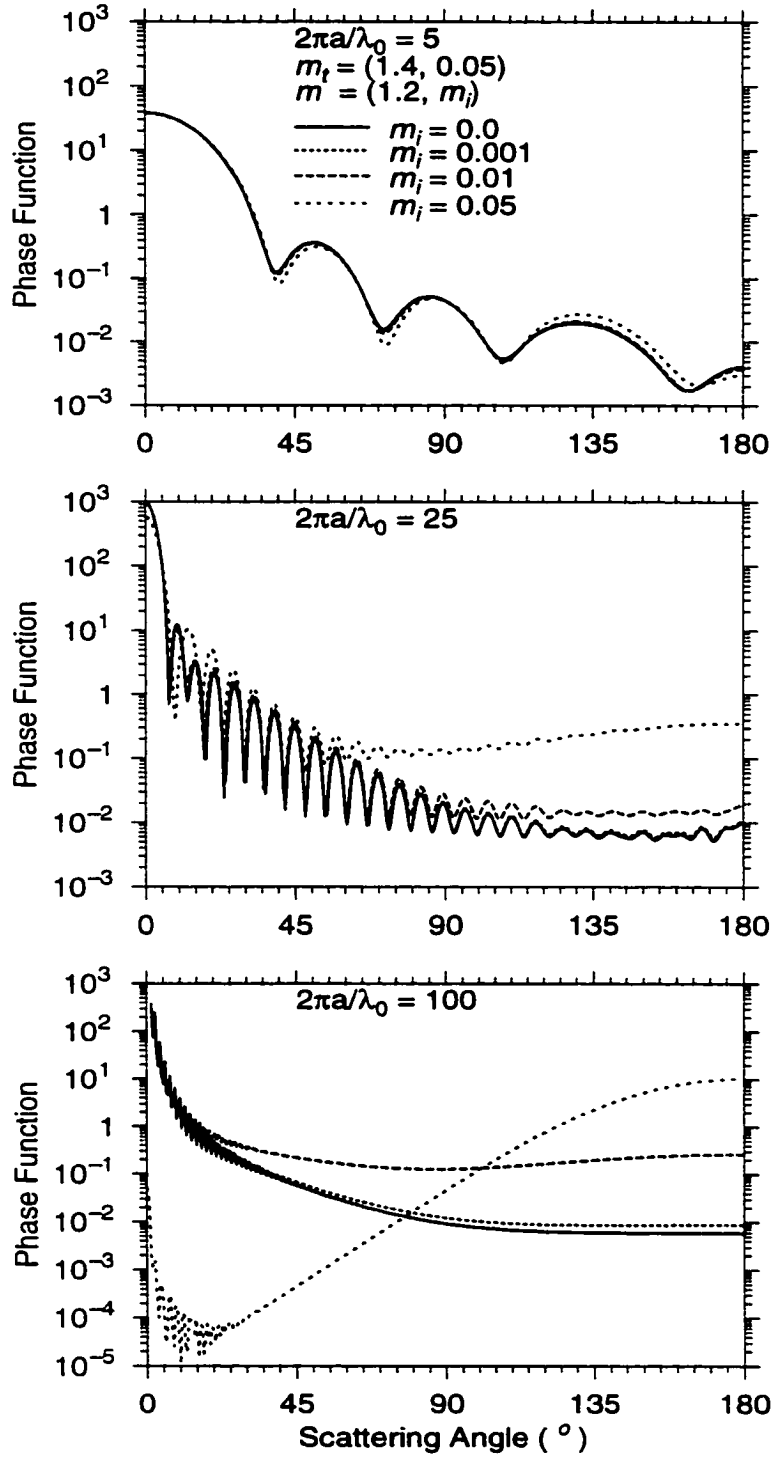

Figure 4.7: Scattering phase function versus scattering angle for spheres with a refractive index of 1.4 + 0.05i, immersed in a medium with a real refractive of 1.2 and an imaginary refractive index of 0.0, 0.001, 0.01 and 0.05. The size parameters are 5, 25 and 100.

The extinction, scattering, and absorption efficiencies, and the phase function and asymmetry factor of the scatterer are derived by using the conceptual integrating sphere to be the surface of the scatterer. Exemplary results show that, the absorbing host medium can reduce the scattering efficiency to as small as zero. So, for a particle with large size parameter in an absorbing medium, the extinction by the particle is mostly due to the absorption and close to one when size parameter is very large. This development offsets the drawbacks in several earlier models and is suitable for the application in related research fields.

Chapter 5

Anomalous diffraction theory for light scattering by arbitrarily oriented hexagonal and cylindrical crystals

5.1 Introduction

The anomalous diffraction theory (ADT) is often used to investigate the scattering and absorption by nonspherical particles (e.g., Chýlek and Klett 1991a). The ADT was first discussed by van de Hulst (1957). The premise of the ADT is that the extinction of light by a particle is primarily the result of the interference between the rays that pass through the particle with those that do not pass through it (Ackerman and Stephens 1987). The ADT can calculate the scattering and absorption cross-sections. However, it cannot be used to calculate phase functions. Therefore, one cannot calculate asymmetry factors using the ADT.

The ADT requires that $x = \pi d/\lambda \gg 1$ and $\mid m - 1 \mid \ll 1$, where d is the size of the particle, λ is the wavelength, and m denotes the complex refractive index. The

first assumption states that we can trace a ray path completely through a particle, while the second assumption implies that the refraction and reflection of rays passing through the particle are negligible and that the absorption is not very strong. Thus the ADT becomes more accurate as m approaches one. For very soft particles ($| m-1 | \ll 1$), the ADT is an efficient and effective approximation to the light scattering problem by a particle even when the particle size is not very large (Chýlek and Klett 1991a; 1991b).

The ADT can be applied analytically to nonspherical particles of various shapes. van de Hulst (1957) derived analytical expressions using the ADT for the scattering by spheres and infinitely long circular cylinders oriented perpendicular to the incident light. Scattering by cubes was considered by Napper (1967) for the normal incidence case. Stephens (1984) treated the scattering of obliquely incident light by long circular cylinders. Chýlek and Klett (1991a; 1991b) obtained a simple analytical form for absorption and extinction cross-sections of prismatic columns and plates oriented perpendicular to the incident rays. Anomalous diffraction theory for arbitrarily oriented ellipsoids was studied by Streekstra *et al.* (1994). In this study, we derive the ADT solutions for the light scattering and absorption problems of arbitrarily oriented hexagonal and cylindrical particles. Because the basic geometrical structure of ice crystals in cirrus clouds is hexagonal, this research has its practical applications (Fu *et al.* 1998; 1999).

In the application to a randomly oriented nonspherical particle, the ADT is often highly simplified because of the difficulty in obtaining the general analytical or numerical solutions based on the original notation of the ADT. Bryant and Latimer (1969) suggested that a randomly oriented particle with a volume of V and a projected area of $\hat{P}$ was first converted to a cylinder with the same volume but a thickness of $V/\hat{P}$. Then the extinction and absorption cross-sections of this randomly oriented particle were approximated by applying the ADT to the cylinder with the incident radiation normal to the base of the cylinder. This simplified ADT (SADT) is often used in the studies related to the climate and remote sensing applications (Mitchell

and Arnott 1994; Arnott *et al.* 1994), but its difference from the original notation of the ADT has not been checked. In this chapter, the SADT is compared with the ADT for different particle shapes. In Section 5.2, the general formulation of the ADT is reviewed. In Section 5.3, the ADT for light scattering and absorption by randomly oriented finite cylinders (discs) and randomly oriented hexagonal columns (plates) are introduced. The simplified ADT is reviewed in Section 5.4. In Section 5.5, the extinction and absorption efficiencies calculated using the ADT and the SADT are compared. Summary and conclusions are given in Section 5.6.

5.2 General formulation of the ADT

Following Chýlek and Klett (1991b), let l_d be a geometrical path of a given ray through the particle (Fig. 5.1). Then the phase delay suffered by this ray relative to a parallel ray traversing the same distance outside the particle is

$$\psi = kl_d(m-1), \tag{5.1}$$

where $k = 2\pi/\lambda$, and the complex refractive index of the particle can be written as $m = m_r - im_i$. Therefore, the phase delay ψ is a function of the ray location on the projected area p of the particle onto a plane perpendicular to the incident radiation.

Using ADT, the forward-scattering amplitude $s(0)$ can be expressed as

$$s(0) = \frac{k^2}{2\pi}\int\int_p (1 - e^{-i\psi})\, dp, \tag{5.2}$$

where p is the projected area of the scatterer.

Let $\rho = kl_d(m_r - 1)$, $r = kl_d m_i$, then

$$s(0) = \frac{k^2}{2\pi}\int\int_p (1 - e^{-i\rho}e^{-r})\, dp. \tag{5.3}$$

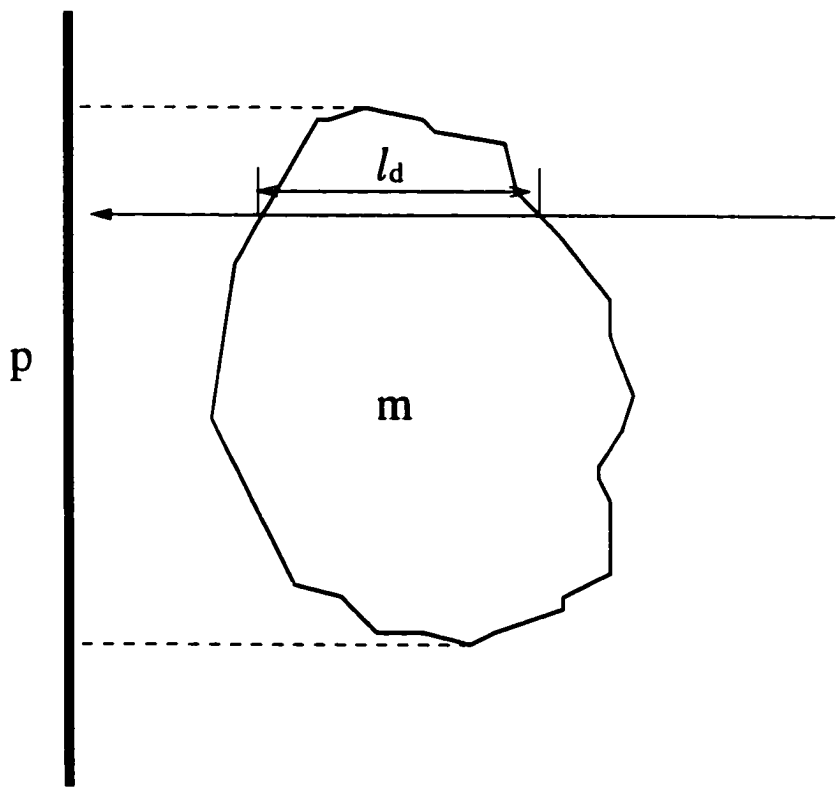

Figure 5.1: Geometry of the anomalous diffraction theory (ADT). The path of an individual ray within a particle is denoted by l_d. P and m are projected area and refractive index, respectively.

Therefore, the extinction, absorption and scattering cross-sections can be expressed in the forms

$$\sigma_e = (\frac{4\pi}{k^2}) Re[s(0)] = 2 \int \int_p (1 - e^{-r} cos\rho)\, dp. \tag{5.4}$$

$$\sigma_a = \int \int_p (1 - e^{-2r})\, dp, \tag{5.5}$$

$$\sigma_s = \sigma_e - \sigma_a. \tag{5.6}$$

5.3 The ADT for arbitrarily oriented hexagonal and cylindrical particles

In this section, we apply the ADT to arbitrarily oriented hexagonal and cylindrical columns of finite length. Note that the formulae presented here can be applied to hexagonal and cylindrical plates as well as columns.

5.3.1 Analytical formulation of the ADT for arbitrarily oriented hexagonal particles

Figure 5.2 shows the geometry of a hexagonal column of length l and side a in a rectangular coordinate system. The symmetric axis of the column is in the η direction; the ζ axis of the coordinate system is perpendicular to one of the 6 side planes of the column. The arbitrary incident direction is denoted by the azimuth angle α and the elevation angle β. Because of the symmetry of the hexagonal crystal, α is from 0 to $\pi/6$ and β is from 0 to $\pi/2$.

For given obliquely incident ray with azimuth angle α, we can divide the base of the hexagonal column into three areas, as shown in Fig. 5.3. The path from one side to another side of the base in each area, along the direction of the cut, is denoted as l_1, l_2 and l_3, respectively. This path is a function of its position in each area. Here,

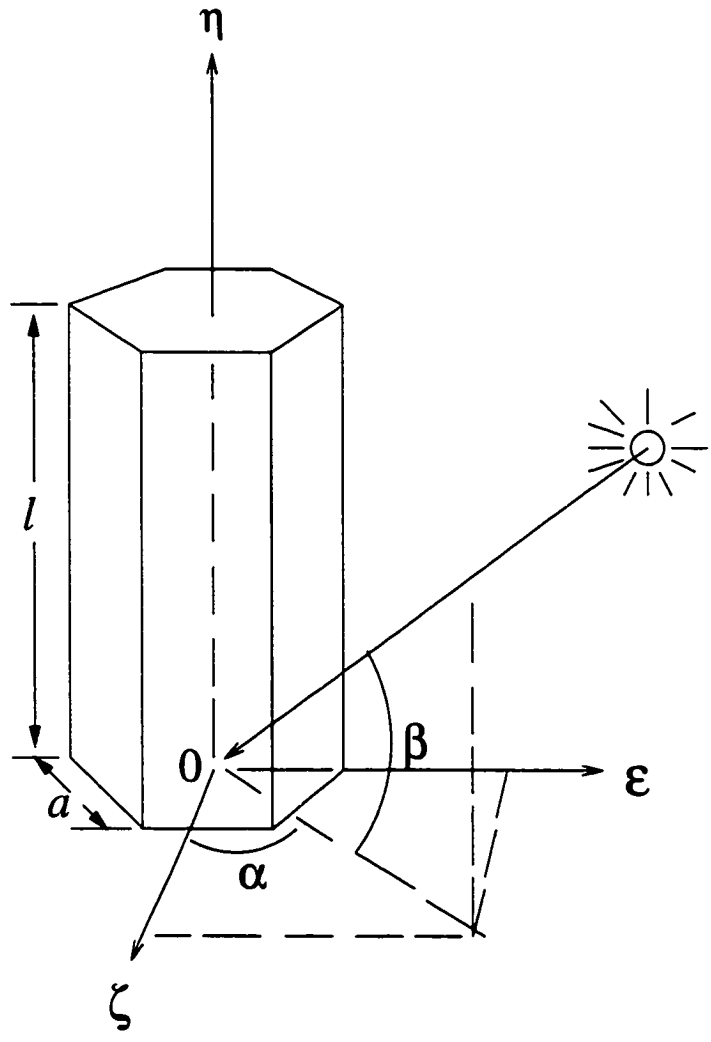

Figure 5.2: Geometry of a hexagonal particle with obliquely incident ray.

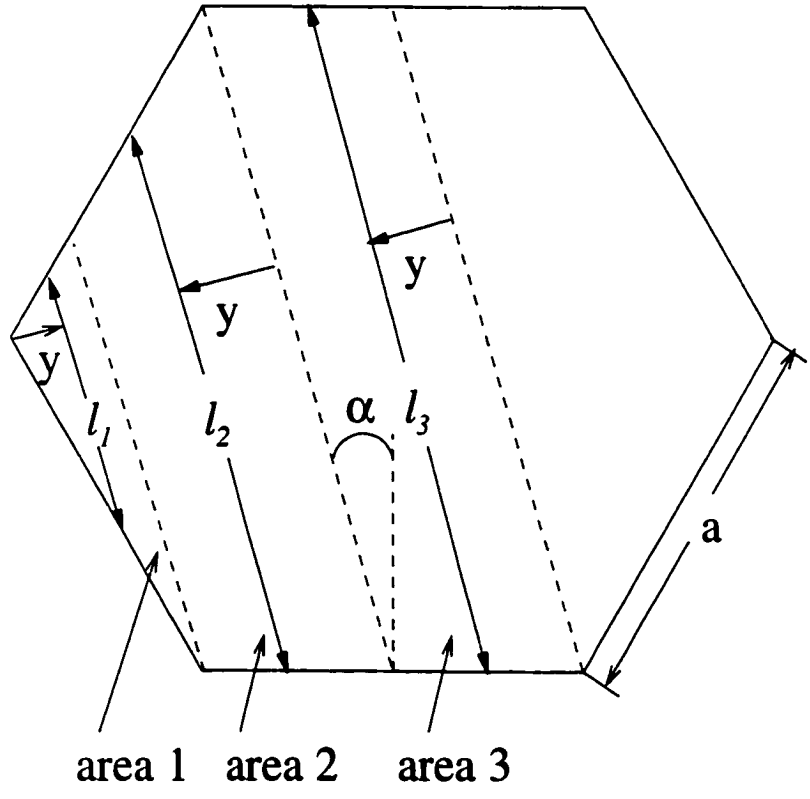

Figure 5.3: Geometry of cuts on the base of a hexagonal column.

we introduce a length variable y to denote the path positions in each area, and y is in the direction perpendicular to the cuts. In Fig. 5.3, we show how y is measured in each area. Therefore, we have

$$l_1 = \frac{\sqrt{3}y}{2sin(\pi/6-\alpha)sin(\pi/6+\alpha)}, \quad 0 \le y \le a\,sin(\pi/6-\alpha), \tag{5.7}$$

$$l_2 = \frac{\sqrt{3}a}{cos\alpha} - \frac{\sqrt{3}y}{2sin(\pi/6+\alpha)cos\alpha}, \quad 0 \le y \le \sqrt{3}asin\alpha, \tag{5.8}$$

$$l_3 = \frac{\sqrt{3}a}{cos\alpha}, \quad 0 \le y \le a\,(cos\alpha - \sqrt{3}sin\alpha). \tag{5.9}$$

In the following, we denote l_1, l_2, and l_3 defined in Eqs.(5.7)-(5.9) as l_n with $n = 1, 2,$ and 3.

To apply the ADT, we cut the hexagonal particle into infinitely thin slices with thickness dy; these slices are parallel both to the symmetric axis of the particle and to the incident direction. So for each slice, we can derive its contribution to the forward-scattering amplitude. For obliquely incident rays with angle β as shown in Fig. 5.4, the slice is divided into 3 areas by $ray1$, $ray2$, $ray3$ and $ray4$. The ray path in the triangular area between $ray1$ and $ray2$ is $z/(sin\beta cos\beta)$. The ray path in the area between $ray2$ and $ray3$ is $l_n/cos\beta$. Therefore, the contribution of each area can be derived by doing the integration in Eq. (5.2) over z for a given dy. Note that the integration in the area between $ray3$ and $ray4$ is the same as that in the area between $ray1$ and $ray2$. So, for obliquely incident rays when $l_n \le lctg\beta$ as shown in Fig. 5.4, the contribution from the slice to $\frac{2\pi}{k^2}s(0)$ is

$$amp^1(l_n) = [2\int_0^{l_n sin\beta}(1 - e^{-\frac{ikz(m-1)}{sin\beta cos\beta}})dz + \int_0^{lcos\beta - l_n sin\beta}(1 - e^{-\frac{ikl_n(m-1)}{cos\beta}})dz]dy. \tag{5.10}$$

So we have

$$amp^1(l_n) = [A + l_n sin\beta - Ae^{Bl_n} + l_n sin\beta e^{Bl_n}]dy, \tag{5.11}$$

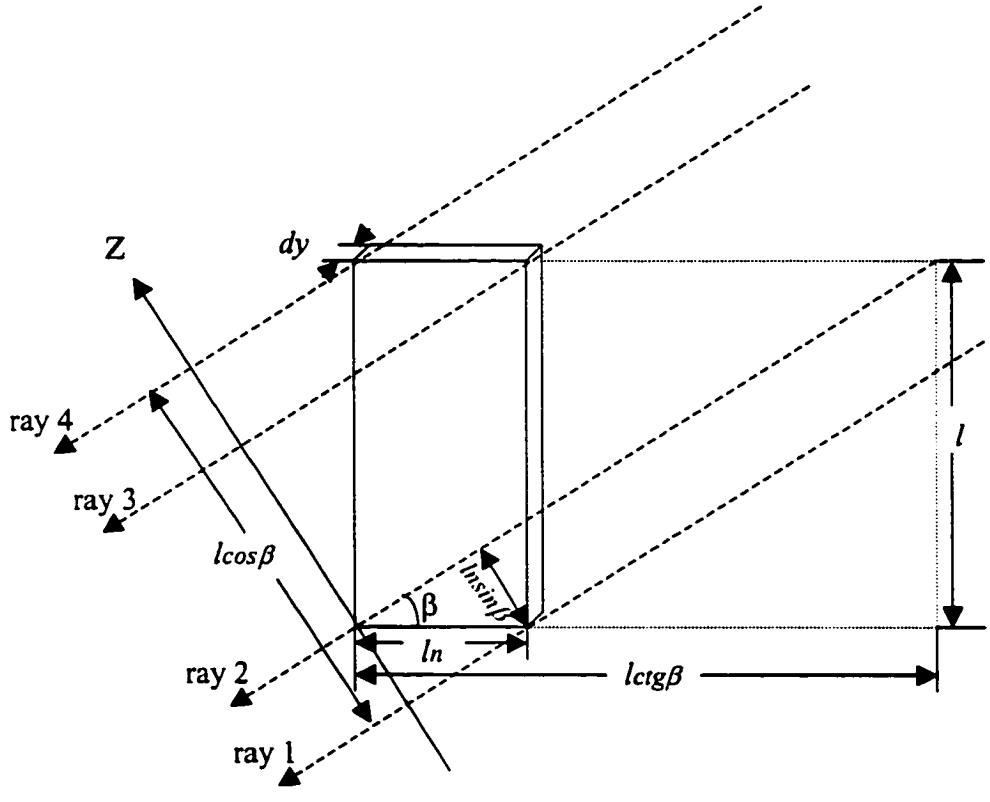

Figure 5.4: Geometry of the ADT for a slice of hexagonal particle. The slice is parallel both to the symmetrical axis of the hexagonal particle and to the incident rays. l_n(n = 1, 2, 3) and y are defined in Fig. 5.3.

where $n = 1, 2, 3$, $B = -\frac{ik(m-1)}{cos\beta}$, and $A = lcos\beta + \frac{2isin\beta cos\beta}{k(m-1)} = lcos\beta + \frac{2sin\beta}{B}$.

For obliquely incident rays when $l_n > lctg\beta$, the contribution from the slice to $\frac{2\pi}{k^2}s(0)$ can be derived as

$$amp^2(l_n) = [2\int_0^{lcos\beta}(1 - e^{-\frac{ikz(m-1)}{sin\beta cos\beta}})dz + \int_0^{l_n sin\beta - lcos\beta}(1 - e^{-\frac{ikl(m-1)}{sin\beta}})dz]dy. \quad (5.12)$$

So we have

$$amp^2(l_n) = [C + l_n D]dy, \quad (5.13)$$

where $n = 1, 2, 3$. $D = sin\beta(1 - e^{-\frac{ikl(m-1)}{sin\beta}})$, and $C = lcos\beta + \frac{2isin\beta cos\beta}{k(m-1)} + lcos\beta e^{-\frac{ikl(m-1)}{sin\beta}}$ - $\frac{2isin\beta cos\beta}{k(m-1)}e^{-\frac{ikl(m-1)}{sin\beta}}$.

Integrating the contributions from all slices over y, we have the forward scattering amplitude s(0) in the form

$$s(0) = \begin{cases} \frac{k^2}{2\pi}[\ 2\ (\ A_1 + A_2\ )\ + A_3\ ], & 0 \le \beta \le arctg[\frac{l}{\sqrt{3}a/cos\alpha}] \\ \frac{k^2}{2\pi}[2A_1 + B_3 + 2(a_2 + b_2)], & arctg[\frac{l}{\sqrt{3}a/cos\alpha}] < \beta \le arctg[\frac{l}{\frac{(\sqrt{3}/2)a}{sin(\pi/6+\alpha)}}] \\ \frac{k^2}{2\pi}[2B_2 + B_3 + 2(a_1 + b_1)], & arctg[\frac{l}{\frac{(\sqrt{3}/2)a}{sin(\pi/6+\alpha)}}] < \beta \end{cases} \quad (5.14)$$

where $A_1, A_2, A_3, B_2, B_3, a_1, a_2, b_1$ and b_2 are given by

$$A_1 = \int_0^{a\,sin(\pi/6-\alpha)} amp^1(l_1), \quad (5.15a)$$

$$A_2 = \int_0^{\sqrt{3}asin\alpha} amp^1(l_2), \quad (5.15b)$$

$$A_3 = \int_0^{a\,(cos\alpha - \sqrt{3}sin\alpha)} amp^1(l_3), \tag{5.15c}$$

$$a_1 = \int_0^{(2/\sqrt{3})lctg\beta sin(\pi/6+\alpha)sin(\pi/6-\alpha)} amp^1(l_1), \tag{5.15d}$$

$$a_2 = \int_{-acos\alpha+(2l/\sqrt{3})ctg\beta sin(\pi/6+\alpha)cos\alpha}^{\sqrt{3}asin\alpha} amp^1(l_2), \tag{5.15e}$$

$$B_2 = \int_0^{\sqrt{3}asin\alpha} amp^2(l_2), \tag{5.15f}$$

$$B_3 = \int_0^{a\,(cos\alpha - \sqrt{3}sin\alpha)} amp^2(l_3), \tag{5.15g}$$

$$b_1 = \int_{(2/\sqrt{3})lctg\beta sin(\pi/6+\alpha)sin(\pi/6-\alpha)}^{asin(\pi/6-\alpha)} amp^2(l_1), \tag{5.15h}$$

$$b_2 = \int_0^{-acos\alpha+(2l/\sqrt{3})ctg\beta sin(\pi/6+\alpha)cos\alpha} amp^2(l_2). \tag{5.15i}$$

The integration results of $A_1, A_2, A_3, B_2, B_3, a_1, a_2, b_1$, and b_2 can be expressed in analytical formulae in the forms

$$A_1 = Aasin(\pi/6-\alpha) + \frac{\sqrt{3}}{4}a^2 sin\beta \frac{sin(\pi/6-\alpha)}{sin(\pi/6+\alpha)} + AE(1 - e^{\frac{\sqrt{3}aB}{2sin(\pi/6+\alpha)}})$$
$$+\frac{sin\beta}{B}[asin(\pi/6-\alpha)e^{\frac{\sqrt{3}aB}{2sin(\pi/6+\alpha)}} + E(1 - e^{\frac{\sqrt{3}aB}{2sin(\pi/6+\alpha)}})], \tag{5.16a}$$

$$A_2 = (A + Msin\beta)\sqrt{3}asin\alpha + 1.5Na^2 sin\beta sin^2\alpha$$
$$+\frac{e^{BM}}{BN}(A - Msin\beta)(1 - e^{BN\sqrt{3}asin\alpha}) + G. \tag{5.16b}$$

$$A_3 = [A + \sqrt{3}a\frac{sin\beta}{cos\alpha} - (A - \sqrt{3}a\frac{sin\beta}{cos\alpha})e^{\frac{B\sqrt{3}a}{cos\alpha}}]a(cos\alpha - \sqrt{3}sin\alpha), \tag{5.16c}$$

$$B_2 = (C + DM)\sqrt{3}asin\alpha + 1.5DNa^2sin^2\alpha. \tag{5.16d}$$

$$B_3 = (Ccos\alpha + \sqrt{3}aD)a(1 - \sqrt{3}tg\alpha), \tag{5.16e}$$

$$a_1 = AJ + \frac{\sqrt{3}}{3}l^2\frac{cos\beta}{tg\beta}sin(\pi/6 - \alpha)sin(\pi/6 + \alpha)$$
$$+AE(1 - e^{Blctg\beta}) + \frac{sin\beta}{B}[Je^{Blctg\beta} + E(1 - e^{Blctg\beta})], \tag{5.16f}$$

$$b_1 = C[asin(\pi/6 - \alpha) - J] + \frac{\sqrt{3}}{4}Da^2\frac{sin(\pi/6 - \alpha)}{sin(\pi/6 + \alpha)}[1 - \frac{4l^2sin^2(\pi/6 + \alpha)}{3a^2tg^2\beta}], \tag{5.16g}$$

$$a_2 = (A + Msin\beta)(\sqrt{3}asin\alpha - I) + 0.5Nsin\beta(3a^2sin^2\alpha - I^2)$$
$$+(A - Msin\beta)\frac{e^{BM}}{BN}(e^{BNI} - e^{BN\sqrt{3}asin\alpha}) + F. \tag{5.16h}$$

$$b_2 = CI + DMI + 0.5DNI^2, \tag{5.16i}$$

where I, J, E, F, M, N and G are given by

$$I = -acos\alpha + \frac{2lcos\alpha sin(\pi/6 + \alpha)}{\sqrt{3}tg\beta}, \tag{5.17a}$$

$$J = \frac{2lsin(\pi/6 + \alpha)sin(\pi/6 - \alpha)}{\sqrt{3}tg\beta}, \tag{5.17b}$$

$$E = \frac{2sin(\pi/6 - \alpha)sin(\pi/6 + \alpha)}{\sqrt{3}B}, \tag{5.17c}$$

$$F = \frac{sin\beta e^{BM}}{B}[(\sqrt{3}asin\alpha - \frac{1}{BN})e^{BN\sqrt{3}asin\alpha} - (I - \frac{1}{BN})e^{BNI}], \tag{5.17d}$$

$$M = \frac{\sqrt{3}a}{cos\alpha}, \tag{5.17e}$$

$$N = -\frac{\sqrt{3}}{2cos\alpha sin(\pi/6+\alpha)}, \tag{5.17f}$$

$$G = sin\beta\frac{e^{BM}}{B}[(\sqrt{3}asin\alpha - \frac{1}{BN})e^{BN\sqrt{3}asin\alpha} + \frac{1}{BN}]. \tag{5.17g}$$

For the calculation of the absorption cross-section σ_a, the previous process is repeated, but $\frac{2\pi}{k^2}s(0)$ is replaced by σ_a, and the A, B, C, D in the previous formulae are replaced by the following expressions:

$$A = lcos\beta - \frac{sin\beta cos\beta}{km_i}, \tag{5.18a}$$

$$B = -\frac{2km_i}{cos\beta}, \tag{5.18b}$$

$$C = 2lcos\beta - (lcos\beta + \frac{sin\beta cos\beta}{km_i})(1 - e^{-\frac{2klm_i}{sin\beta}}), \tag{5.18c}$$

$$D = sin\beta(1 - e^{-\frac{2klm_i}{sin\beta}}). \tag{5.18d}$$

To calculate the extinction, scattering and absorption efficiencies of the particle, one needs to calculate the geometrical projected area of the particle. The projected area of the hexagonal column is given by

$$P = \frac{3\sqrt{3}}{2}a^2 sin\beta + 2alcos\beta cos\alpha. \tag{5.19}$$

For randomly oriented hexagonal particles, the extinction, scattering and absorption cross-sections and the projected area are given respectively by

$$\hat{\sigma}_{e,s,a} = \frac{\pi}{6}\int_0^{\pi/6}\int_0^{\pi/2}\sigma_{e,s,a}cos\beta d\beta d\alpha, \tag{5.20a}$$

and

$$\hat{P} = \frac{\pi}{6}\int_0^{\pi/6}\int_0^{\pi/2} P cos\beta d\beta d\alpha. \tag{5.20b}$$

Therefore, the extinction, scattering and absorption efficiencies for randomly oriented hexagonal particles are: $\hat{Q}_{e,s,a} = \hat{\sigma}_{e,s,a}/\hat{P}$.

5.3.2 The ADT solution for arbitrarily oriented cylindrical particles

For circular cylinders (discs) as shown in Fig. 5.5, Liu *et al.*(1998) introduced an ADT solution by using the analytic geometry. In this section, similar to our study for arbitrarily oriented hexagonal crystals, we derive the ADT solution for finite circular cylinders by using the the geometric arguments. Herein, we cut the particle into very thin slices; these slices are parallel both to the symmetric axis of the particle and to the incident direction. The height of the slice is that of the finite circular cylinder. The width of the slice is a function of its position. In Fig. 5.5, it is clear that the width of the slice $l_y = 2\sqrt{a^2 - y^2}$. So for each slice, we can derive its contribution to the extinction and absorption cross-sections following similar processes as we derive Eqs.(5.11) and (5.13).

For obliquely incident rays, when $l_y \leq htg\theta$, the contribution from the slice to $\frac{2\pi}{k^2}s(0)$ can be derived as

$$\frac{2\pi}{k^2}ds(0) = [A + l_y cos\theta - Ae^{Bl_y} + l_y cos\theta e^{Bl_y}]dy. \tag{5.21}$$

where $B = -\frac{ik(m-1)}{sin\theta}$, and $A = hsin\theta + \frac{2isin\theta cos\theta}{k(m-1)} = hsin\theta + \frac{2cos\theta}{B}$.

When $l_y > htg\theta$, the contribution from the slice to $\frac{2\pi}{k^2}s(0)$ can be derived as

$$\frac{2\pi}{k^2}ds(0) = [C + l_y D]dy, \tag{5.22}$$

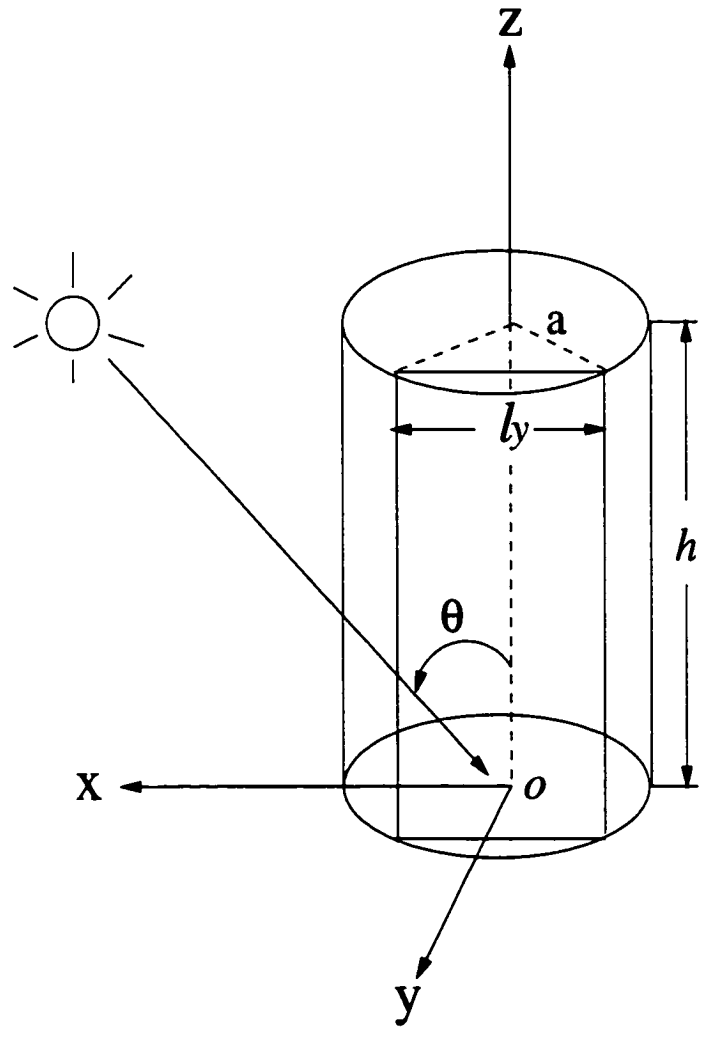

Figure 5.5: Geometry of a finite circular cylinder with obliquely incident ray.

where $D = cos\theta(1 - e^{-\frac{ikh(m-1)}{cos\theta}})$, and $C = hsin\theta + \frac{2isin\theta cos\theta}{k(m-1)} + hsin\theta e^{-\frac{ikh(m-1)}{cos\theta}} - \frac{2isin\theta cos\theta}{k(m-1)} e^{-\frac{ikh(m-1)}{cos\theta}}$.

For the calculation of the absorption cross-section σ_a, the previous process is repeated, but $\frac{2\pi}{k^2}s(0)$ is replaced by σ_a, and the A, B, C, D in the previous formulae are replaced by the following expressions:

$$A = hsin\theta - \frac{sin\theta cos\theta}{km_i}, \tag{5.23a}$$

$$B = -\frac{2km_i}{sin\theta}, \tag{5.23b}$$

$$C = 2hsin\theta - (hsin\theta + \frac{sin\theta cos\theta}{km_i})(1 - e^{-\frac{2khm_i}{cos\theta}}), \tag{5.23c}$$

$$D = cos\theta(1 - e^{-\frac{2khm_i}{cos\theta}}). \tag{5.23d}$$

For circular cylinders, the integration for all slices are done numerically, which requires that each slice be thin enough until the result is convergent. The extinction, scattering and absorption cross-sections for randomly oriented cases can be obtained from the integration of σ_e, σ_s and σ_a over incident angles, so that

$$\hat{\sigma}_{e,s,a} = \int_0^{\pi/2} \sigma_{e,s,a} sin\theta \, d\theta, \tag{5.24}$$

Again, in numerical calculations, the resolution of the incident angles should be high enough to get a convergent solution.

It is known that for a randomly oriented convex particle with a surface area of S, the projected area $\hat{P} = S/4$. Therefore, the extinction, scattering and absorption efficiencies for the randomly oriented convex particles are $\hat{Q}_e = 4\hat{\sigma}_e/S$, $\hat{Q}_s = 4\hat{\sigma}_s/S$ and $\hat{Q}_a = 4\hat{\sigma}_a/S$, respectively.

5.4 The simplified ADT for randomly oriented particles

Bryant and Latimer (1969) suggested a simplified ADT which is often used for simulating the light scattering and absorption by nonspherical particles (Mitchell and Arnott 1994; Arnott *et al.* 1994). In this method, a randomly oriented particle with a volume of V and projected area of $\hat{P}$ is first converted into a cylinder with a thickness of $d_e = V/\hat{P}$. Then the extinction and absorption efficiencies of this randomly oriented particle can be approximated by applying the ADT to the cylinder with the incident radiation normal to the base in the forms

$$\hat{Q}_e = 2 - 2exp(-kd_e m_i)cos[kd_e(m_r - 1)], \tag{5.25}$$

$$\hat{Q}_a = 1 - exp(-2kd_e m_i). \tag{5.26}$$

Here the extinction and absorption efficiencies are defined as the extinction and absorption cross-sections divided by the particle projected area.

From Eqs.(5.25) and (5.26), we can see that in the SADT, the extinction and absorption efficiencies depend only on the d_e which can be considered as the effective distance of the light passing through the particle. Therefore, for particles with arbitrary shapes, once we know their volume and the projected area for randomly oriented situation, we can get the effective distance d_e and thus $\hat{Q}_e$ and $\hat{Q}_a$ can be calculated. For a sphere with a radius of a, the effective distance $d_e = (4/3)a$. For a randomly oriented circular cylinder with a base radius of a and a thickness of h, $d_e = 2ah/(a + h)$. For a randomly oriented hexagonal column with a base side of a and a thickness of h, $d_e = 2\sqrt{3}ah/(\sqrt{3}a + 2h)$.

The SADT provides the simplest way to apply the ADT to randomly oriented particles with different shapes. However, since the light scattering and absorption processes also depend on the particle shape when the particle size parameter is in the intermediate region, this simple approximation may introduce significant differences

from the original ADT. In the following section, we will show the results from both the SADT and ADT for randomly oriented finite circular cylinders and hexagonal columns to justify the notation here.

5.5 Results

Figure 5.6 shows the extinction and absorption efficiencies of hexagonal ice crystals calculated by the ADT at a wavelength of 3.969 μm ($m = 1.3645 + 0.01112i$). l, a, β and α are defined in Fig. 5.2. The aspect ratio l/a is 6 in this case. We can see that the extinction and absorption efficiencies of hexagonal particles depend on the orientation of the particles. For normal incident light (i.e., $\beta = 0$), when $\alpha = 0$ and $\alpha = \pi/6$, these are simply the special cases of flat incidence and edge-on incidence shown by Chýlek and Klett (1991a). We can see that the extinction and absorption curves for $\alpha = \pi/12$ are between those for $\alpha = 0$ and $\alpha = \pi/6$. When $\beta = \pi/2$, i.e., the incident direction is perpendicular to the base plane of the hexagonal particle, there is no difference between curves for different α.

Using the ADT for arbitrarily oriented hexagonal columns or plates, we can calculate the scattering and absorption efficiencies of randomly oriented hexagonal particles. The ADT results for randomly-oriented hexagonal ice crystals have been used in the studies by Fu *et al.* (1998; 1999).

To compare the ADT with the SADT for different particle shapes, we use the analytical solutions presented in sections 5.3.1 and 5.3.2 for hexagonal and cylindrical particles, respectively. For spherical particles, Eqs.(5.4) and (5.5) can be integrated analytically so that

$$Q_e = 2Re[1 - 2exp(L)/L - 2[1 - exp(L)]/L^2], \tag{5.27}$$

$$Q_a = 1 - 2exp(H)/H - 2[1 - exp(H)]/H^2. \tag{5.28}$$

where $L = -2ka(m-1)i$, $H = -4kam_i$, and a is the radius of the sphere.

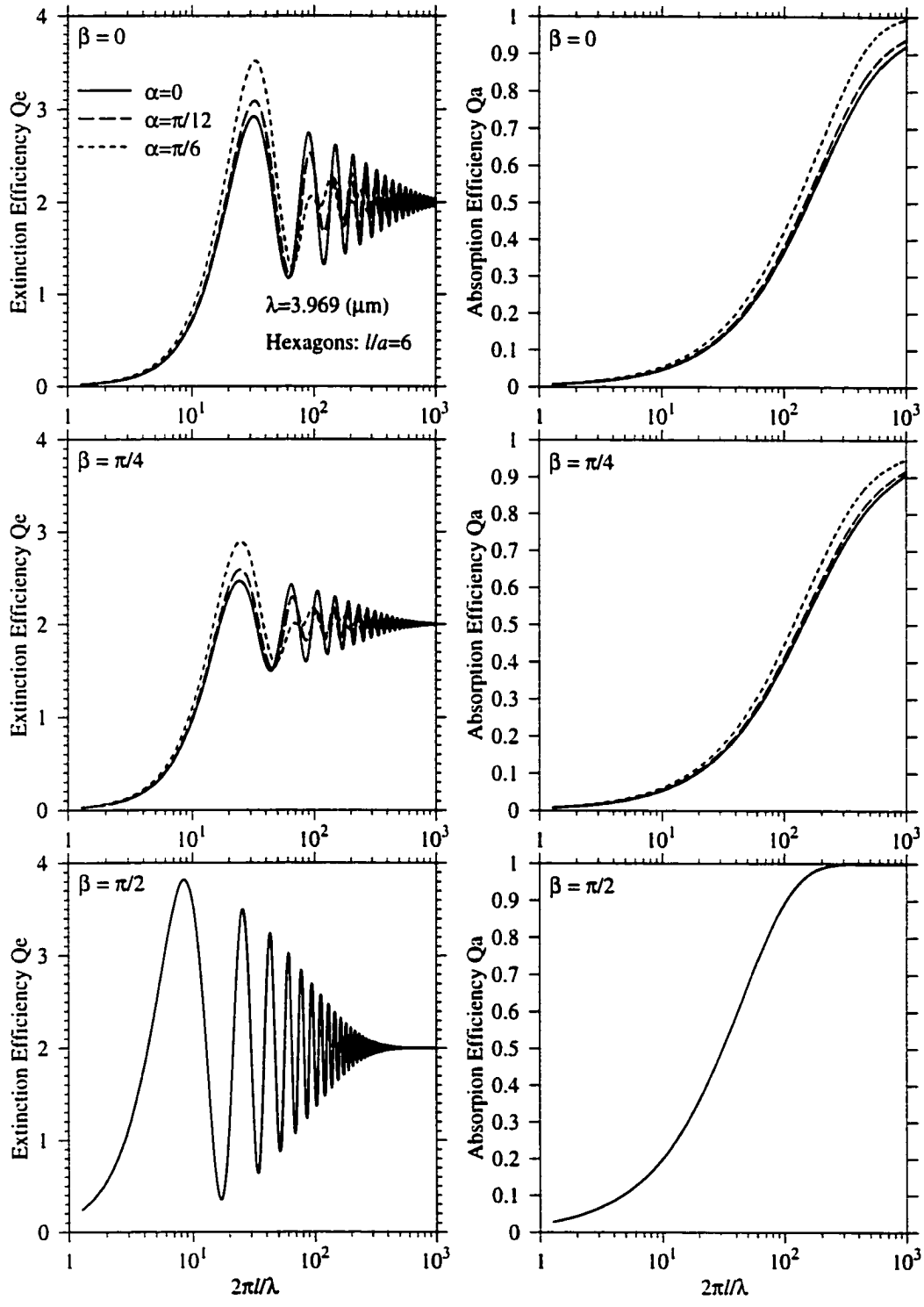

Figure 5.6: Extinction and absorption efficiencies of hexagonal ice crystals calculated by the ADT at a wavelength of 3.969 μm ($m = 1.3645 + 0.01112i$). l, a, α and β are shown in Fig. 5.2. The aspect ratio l/a is 6.

Figure 5.7 shows the extinction and absorption efficiencies of spheres with the refractive indices of 1.1+0.01i, 1.1+0.10i and 1.1+0.20i as functions of size parameter ($\pi d_e/\lambda$), calculated using the ADT and the SADT. Only small real refractive index is used here to satisfy the requirement of the ADT. Three different imaginary refractive indices are chosen to show the difference between the ADT and the SADT under different absorption conditions. We find that in the intermediate size parameter region, the absorption efficiency from the SADT is systematically larger than that from the ADT. When the absorption is weak, we can see that the extinction curve from the SADT is very different from that of the ADT. The SADT shows an extinction pattern which is particular for disc-like particle shapes with normally incident light. Thus, using the SADT to calculate the extinction efficiency may result in erroneous solutions if the absorption is not strong enough. However, when the absorption is strong, because the interference at the far field is very weak due to the absorption of the rays passing through the particle volume, the SADT extinction curve becomes much closer to that from the ADT, though the difference is still significant in the resonance region where the particle dimension is close to the incident wavelength.

Figure 5.8 shows the extinction and absorption efficiencies of randomly oriented finite circular cylinders with the refractive indices of 1.1+0.01i, 1.1+0.10i and 1.1+0.20i as functions of size parameter ($\pi d_e/\lambda$), calculated using the ADT and the SADT. An aspect ratio $h/a = 2$ is used in this calculation. In the ADT calculations, we set the thickness of each slice as $0.01a$, where a is the radius of the cylinder base. For the randomly orientation treatment, we use an angle resolution of $\pi/180$ for the integration. We can see that the absorption efficiencies from the SADT are larger than those from the ADT in the intermediate size parameter region for all of the three different refractive indices. The difference between the extinction efficiencies also becomes more significant than that for spherical particles. It is noted here that by using $\pi d_e/\lambda$ as the size parameter, the extinction and absorption curves from the SADT for any particle shapes are same; they are simply those for discs with normally incident light. Using a larger aspect ratio $h/a = 6$ for the randomly oriented finite circular

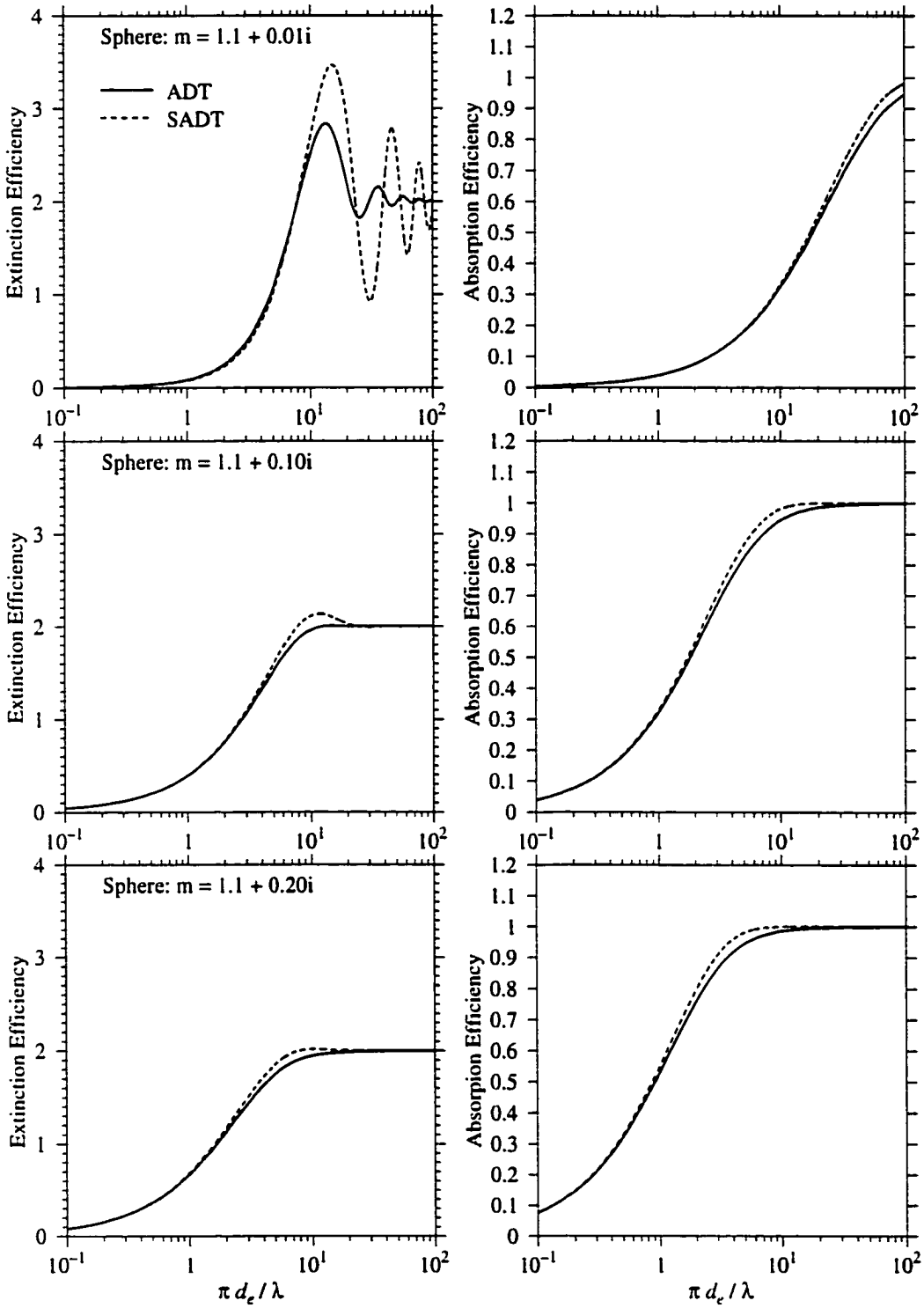

Figure 5.7: Extinction and absorption efficiencies of spheres with refractive indices 1.1+0.01i, 1.1+0.10i and 1.1+0.20i as functions of size parameters ($\pi d_e/\lambda$), calculated using the ADT and the SADT.

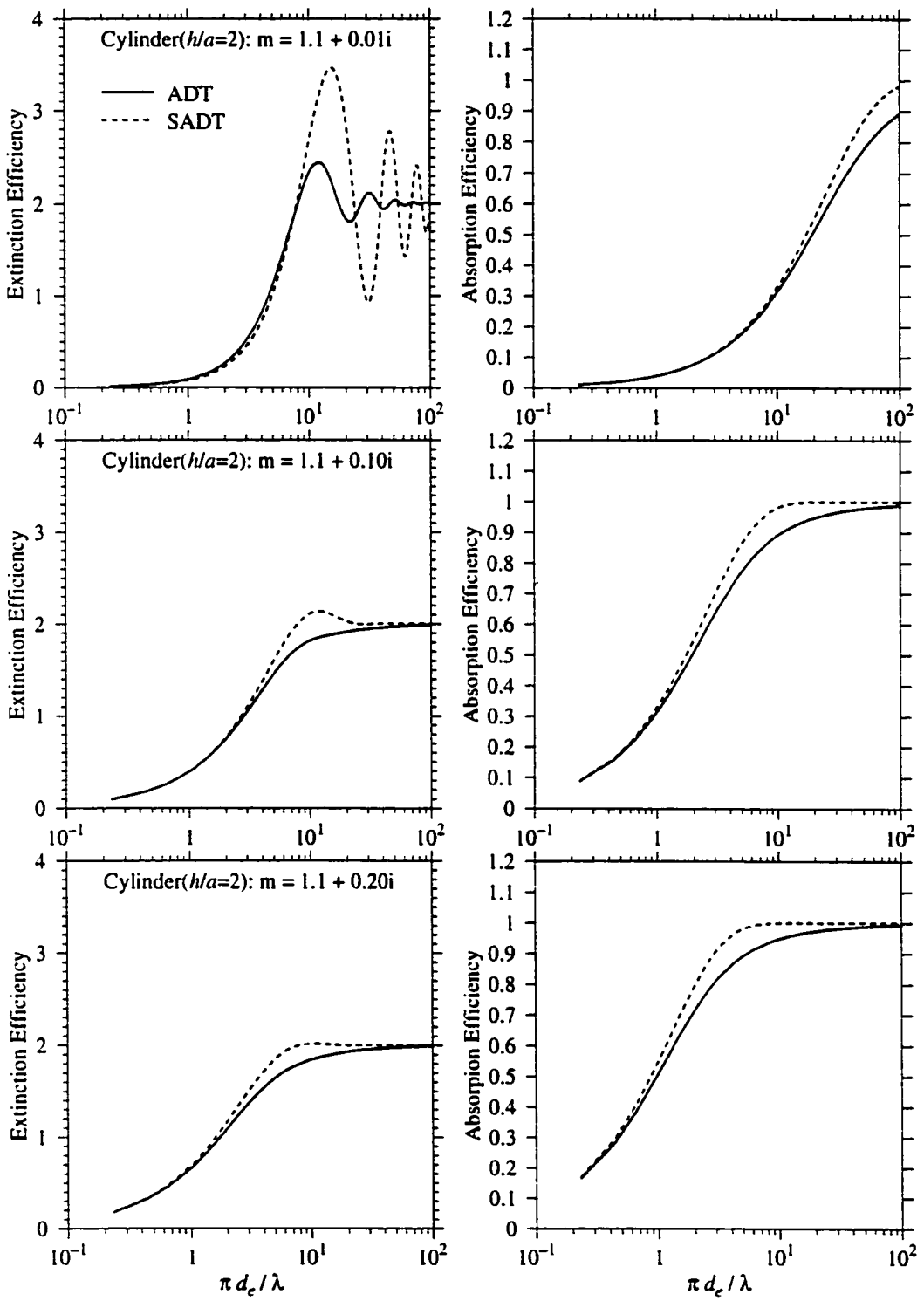

Figure 5.8: Same as Fig. 5.7, but for randomly oriented finite circular cylinders with an aspect ratio (h/a) of 2.

cylinders, as shown in Fig. 5.9, we can see that the difference between the ADT and the SADT results becomes smaller but still significant. By comparing Figs. 5.8 and 5.9 with Fig. 5.7, we can see that the differences between the ADT and the SADT for randomly oriented finite circular cylinders are larger than those for spheres.

For randomly oriented finite hexagonal columns, as shown in Figs. 5.10 and 5.11, we can see similar situations as those for randomly oriented finite circular cylinders. However, the differences between the ADT and the SADT results for hexagonal columns become slightly larger. It can be concluded that, using the SADT to calculate the single scattering and absorption properties for randomly oriented nonspherical particles may cause the results very different from those based on the original notation of the ADT. Because the refractive indices used here are very small, the ADT may be considered as a good approximation. However, by comparing with the exact theory (Fu *et al.* 1999), the ADT may still underestimate the absorption efficiencies due to neglecting the tunneling effects. Since the absorption efficiencies from the simplified ADT are larger than those from the ADT, the SADT results may agree better with the exact theory. But this better agreement is fortunate because the errors in the ADT and those related to the simplifications in the SADT partly cancel each other.

5.6 Summary and conclusions

In this study, the anomalous diffraction theory is applied to arbitrarily oriented hexagonal and cylindrical particles. The analytical formulae are derived for the extinction and absorption cross-sections of arbitrarily oriented hexagonal and cylindrical particles, which makes the calculation very efficient. The accuracy of these solutions is determined by the conditions under which the ADT is valid, i.e., the conditions for refractive index m and size parameter x. If the ADT conditions are satisfied, the current solutions would give reliable results for the scattering and absorption by arbitrarily oriented hexagonal and cylindrical particles. However, if the particle is not "very soft", the ADT cannot be used to simulate the scattering and absorption by

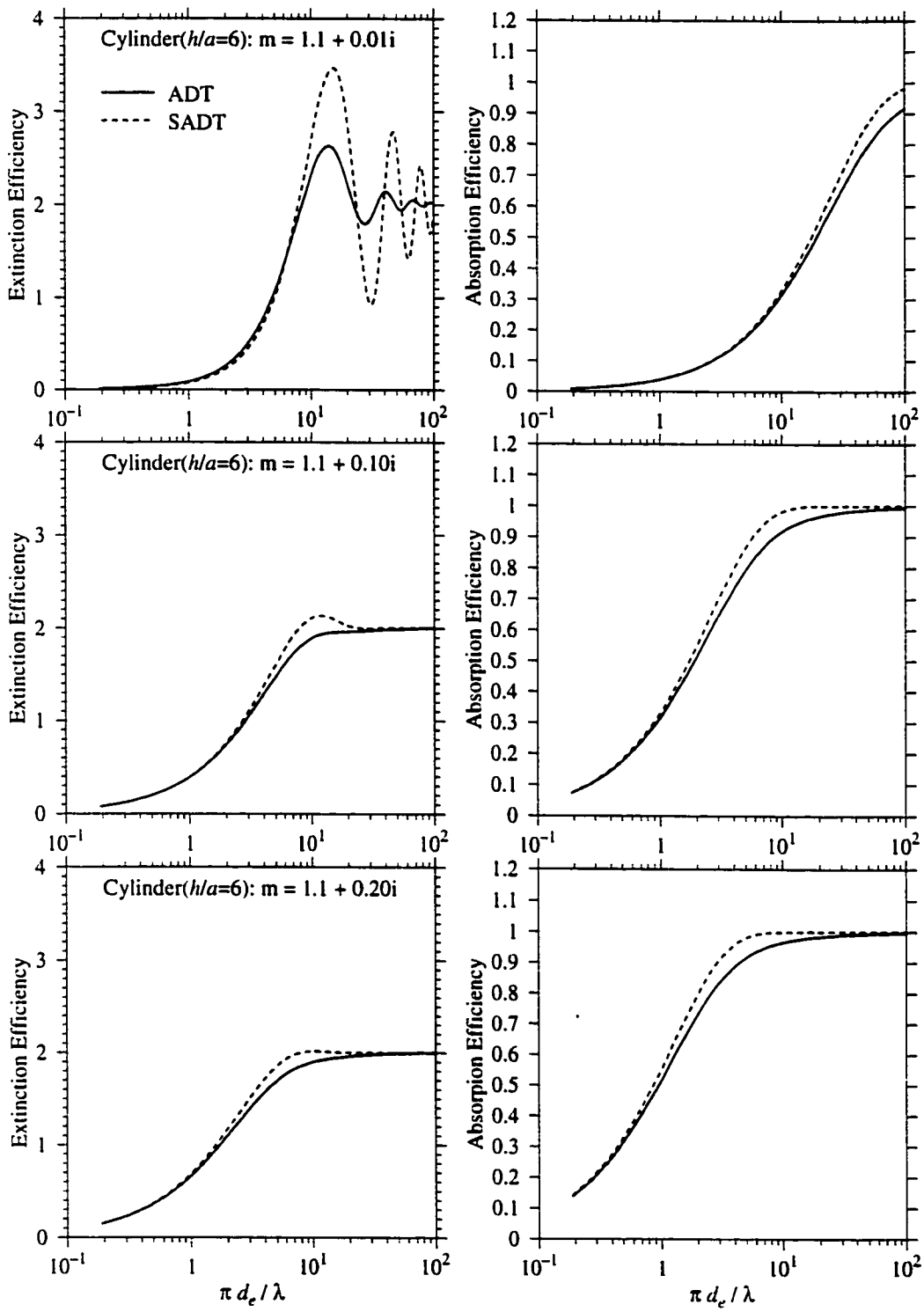

Figure 5.9: Same as Fig. 5.7, but for randomly oriented finite circular cylinders with an aspect ratio (h/a) of 6.

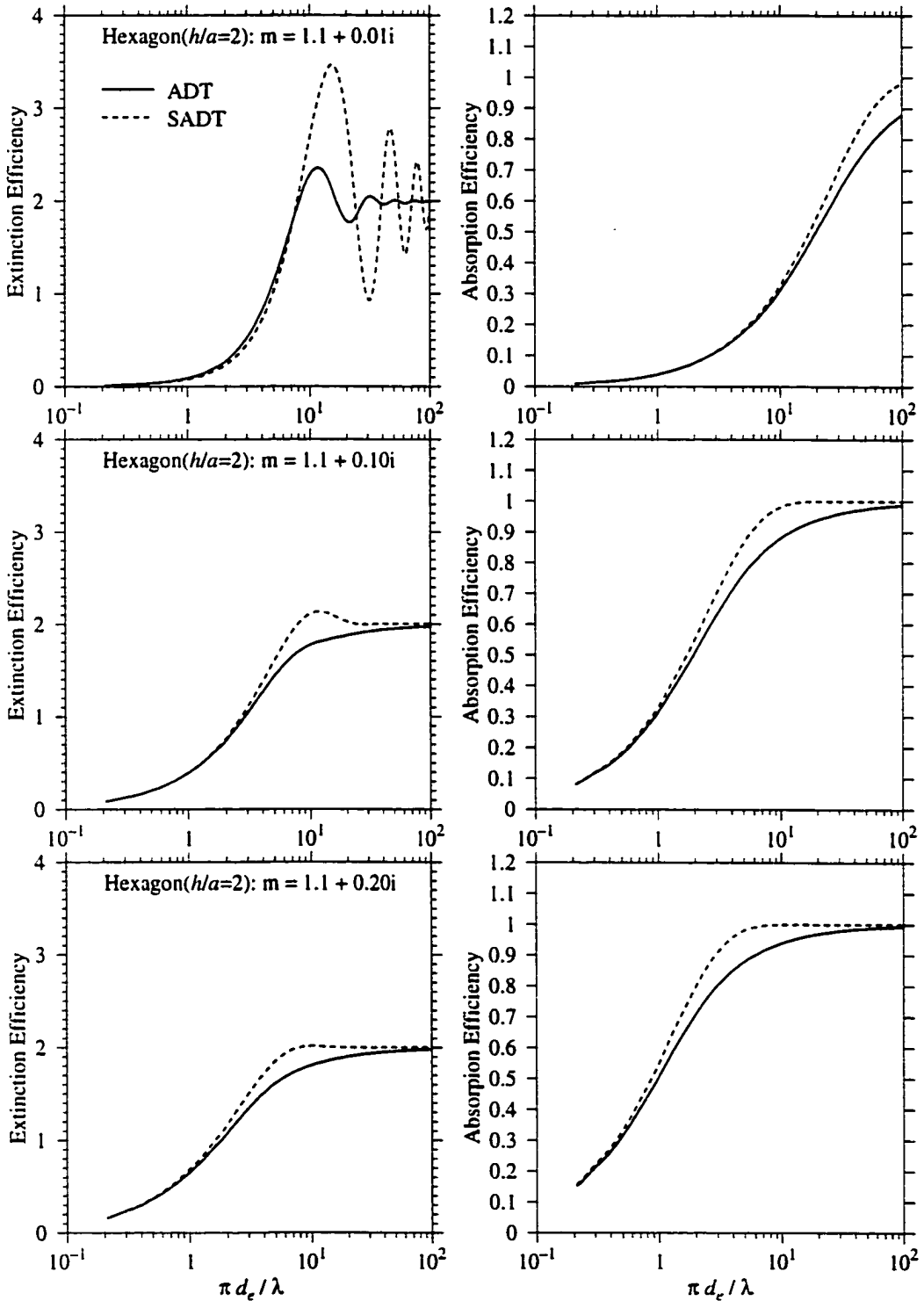

Figure 5.10: Same as Fig. 5.7, but for randomly oriented finite hexagonal columns with an aspect ratio (h/a) of 2.

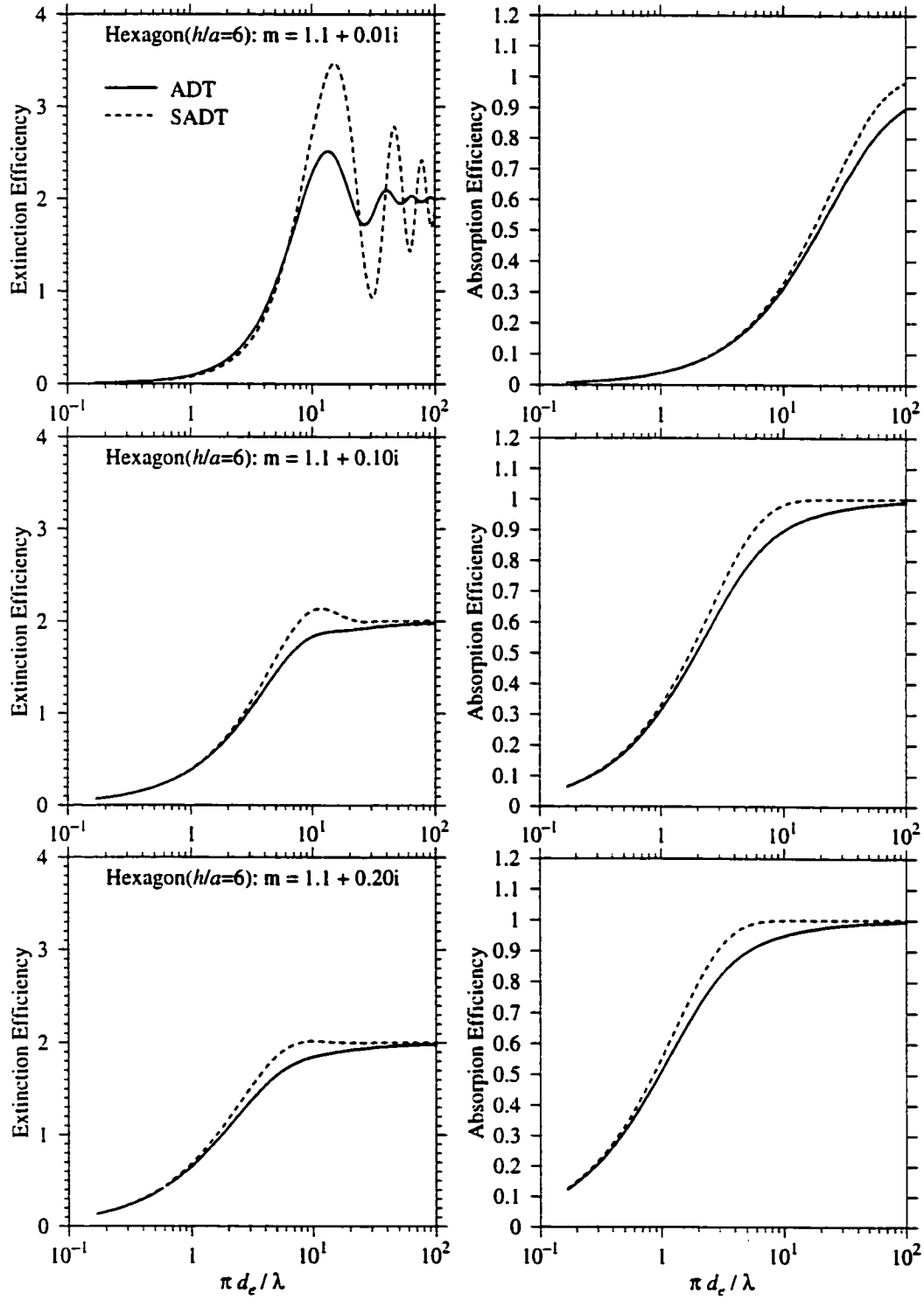

Figure 5.11: Same as Fig. 5.7, but for randomly oriented finite hexagonal columns with an aspect ratio (h/a) of 6.

nonspherical particles without verification using rigorous methods (Maslowska *et al.* 1994).

Additionally, the simplified ADT is compared with the ADT using the original notation for finite circular cylinders and hexagonal columns. In the resonance region of size parameters, significant differences are found in both extinction and absorption efficiencies. Using the simplified ADT for randomly oriented particles may introduce a difference as large as ~15% in the absorption efficiency and ~100% in the extinction efficiency.

Chapter 6

On the retrieval of cirrus particle size using infrared channels in the 8-12 μm window: Reliability and implications

6.1 Introduction

Cirrus cloud is one of the most important, yet least understood components in the climate system (Liou 1986). A successful retrieval of cirrus cloud properties from aircraft or satellite data requires accurate methodologies for the calculation of light scattering and absorption by nonspherical cirrus ice crystals. Since there are observational and computational difficulties in determining the radiative properties of nonspherical ice crystals in cirrus clouds, it is common practice to approximate nonspherical ice crystals by spherical particles (e.g., Stephens *et al.* 1990; Ackerman *et al.* 1990; Sun and Shine 1995) so that the exact theories can be used. Unfortunately, this approach does not account for the hexagonal structure of ice crystals with finite length. The cirrus radiative properties in the infrared are dominated by absorption,

although the effects of scattering cannot be neglected (Fu *et al.* 1999). For this reason, the use of Mie theory to evaluate the scattering coefficient and asymmetry factor for ice crystals may not present a serious problem for the calculation of the emissivity of cirrus clouds at infrared wavelengths. However, using Mie theory to specify the absorption coefficient may result in significant errors.

The absorption and extinction cross-section of a sphere can be substantially greater than what is predicted from its physical cross-section. Mitchell (1995) pointed out that for irregular ice particles, grazing photons might not be captured as surface waves. So only the physical cross-section of the particle needs to be considered when predicting scattering and absorption. It has been suggested that the anomalous diffraction theory (ADT) would be an appropriate method to calculate the single scattering properties of nonspherical particles (Mithcell *et al.* 1996). Because of the simplicity of the ADT, it is often used to calculate the absorption coefficients of ice crystals for the remote sensing of cirrus clouds (Baran *et al.* 1998; Holz *et al.* 1998). However, the validity of the ADT for the retrieval of the microphysical properties of cirrus clouds need to be checked since the ADT is an approximate method (Van de Hulst 1957).

To get accurate solutions for the radiative properties of nonspherical particles, a finite-difference time domain (FDTD) program with a perfectly matched layer (PML) absorbing boundary condition (ABC) has been developed in Chapter 2. In this chapter, for randomly oriented hexagonal ice crystals, the accuracy of approximate methods including Mie theory, the ADT and the GOM in the calculation of single-scattering properties for nonspherical particles are first examined for the application to remote sensing. Here the reference results are based on the FDTD calculations for hexagonal particles with small size parameters and the GOM for large size parameters. We then consider 30 size distributions from *in-situ* measurements to simulate the single-scattering properties of cirrus clouds. The spectral brightness temperatures in the 8-12 μm window from the cirrus clouds is calculated using the discrete-ordinate radiative transfer model (Stamnes *et al.* 1988). Here we focus on

the wavelengths of 8.333, 11.155 and 12.0 μm since the differences in cirrus emissivity between these wavelengths are often used to detect cirrus clouds and retrieve the ice crystal size based on the observed brightness temperatures (Strabala and Ackerman (1994); Stubenrauch *et al.* 1999). Here, the errors in the simulated brightness temperatures due to the approximate single-scattering models and their effects on the retrieved particle sizes are addressed. We also discuss the implication of our results to the retrieval of cirrus particle size using infrared channels in the 8-12 μm window.

The single-scattering models used are reviewed in Section 6.2. The calculation of the single-scattering properties of cirrus clouds is documented in Section 6.3. The brightness temperatures at top of atmosphere (TOA) calculated by using different single-scattering models are discussed in Section 6.4. The retrieval of mean effective size of cirrus clouds is addressed in Section 6.5. Summary and conclusions are given in Section 6.6.

6.2 Single-scattering models

In the present study, we assume that the nonspherical ice crystals are randomly oriented hexagonal columns. The aspect ratio of the columns follows those used in Fu (1996). The refractive indices for ice from Warren (1984) are used. The single-scattering properties of randomly oriented hexagonal ice columns are calculated at wavelengths of 8.333, 11.155 and 12.0 μm, which are often used for remote sensing of cirrus clouds. Different scattering models including the anomalous diffraction theory (ADT), Mie theory, the geometric optics method (GOM) (Yang and Liou 1996b), and the finite-difference time domain (FDTD) technique are used. The FDTD model used is developed in Chapter 2. The ADT model used is the analytical solution for hexagonal crystals documented in Chapter 5. Mie theory and the GOM for nonspherical particles are introduced as follows.

6.2.1 Mie theory

To apply Mie theory, nonspherical particles are usually converted into spheres of either equivalent surface area or equivalent volume. Letting S and V be the surface area and volume of a nonspherical convex particle, the radius of the equivalent sphere is given by

$$r_s = \frac{1}{2}(S/\pi)^{1/2}, \tag{6.1}$$

or

$$r_v = (3V/4\pi)^{1/3}, \tag{6.2}$$

where r_s and r_v are the radii for spheres with equivalent surface area and equivalent volume, respectively.

For a nonspherical particle, spheres with both equivalent surface area and volume can also be defined by letting $S = n4\pi r_{vs}^2$ and $V = n\frac{4}{3}\pi r_{vs}^3$, where n is the number of spheres. So we have the radius r_{vs} as (Fu *et al.* 1998)

$$r_{vs} = 3V/S. \tag{6.3}$$

In this case, the particle size distribution is no longer preserved. However, the ratio of volume V to projected area P is conserved for each particle. Since this ratio is simply the effective distance as discussed in Chapter 5, it is a fundamental parameter in determining the absorption efficiency of a nonspherical particle. It can be shown that $r_{vs} \leq r_v \leq r_s$. In the present study, we denote Mie theory applied to these spheres as MieS, MieV or MieVS, corresponding to r_s, r_v and r_{vs}. The size parameter x for nonspherical particles is defined here as

$$x = 2\pi r_{vs}/\lambda. \tag{6.4}$$

6.2.2 Geometric optics method

Based on the laws of geometric optics, the geometric optics method (GOM) assumes that light consists of separate localized rays that travel along straight paths. It is an asymptotic approach that becomes accurate when a locally smooth surface is much larger than the incident wavelength. The GOM has been used to derive the scattering, absorption and polarization properties of nonspherical ice crystals. Computation of the angular scattering patterns for hexagonal ice crystals based on the GOM were first reported by Jacobowitz (1971), where infinity hexagonal columns were assumed. Cai and Liou (1982) developed a ray-tracing model for arbitrarily oriented hexagonal ice crystals, which took into account internal absorption and polarization. Along the same line, Takano and Jayaweera (1985), and Muinonen (1989) also carried out numerical computations for the scattering of hexagonal particles. Takano and Liou (1989) developed a geometric optics program that accounted for the ice crystal size distribution and orientation.

In this study, a geometric optics model developed by Yang and Liou (1996b) is used for the calculation of the single-scattering properties for arbitrarily oriented hexagonal ice crystals. The new GOM model uses the ray-tracing technique to solve the near-field on the ice crystal surface, which is then transformed to far-field on the basis of the electromagnetic equivalence theorem. By performing the exact mapping from the near-field to the far-field, the only approximation in this novel geometric optics model is confined to the calculation of the surface field by means of geometric optics.

Though the new geometric optics model removes some of the shortcomings of the conventional geometric optics approach, it still cannot circumvent the large errors for small size parameters. However, for size parameters larger than about 40, the calculation of the surface field and the field inside the particle by means of geometric

optics becomes increasingly accurate as the particle size parameter becomes larger. Therefore, for large size parameters, the GOM is still an accurate model for the calculation of the single-scattering properties of nonspherical particles.

6.2.3 A composite method

Because the FDTD can be applied only to particles with small size parameters, due to its requirement for large CPU time and memory size, a composite methodology (CMP) (Fu *et al.* 1998, 1999), which employs a linear combination of single-scattering properties from Mie theory, the ADT, and the GOM, is applied to fit the FDTD results for small size parameters and the GOM results for large size parameters. Therefore, the CMP is valid for a wide range of size parameters. Following Fu *et al.* (1998, 1999), the scattering efficiency from the CMP is simply derived as the mean value of those from the ADT and the MieVS for hexagonal ice crystals. The asymmetry factor can be obtained from the MieV for size parameters ($x = 2\pi r_{vs}/\lambda$) smaller than 10. For size parameters larger than 10, the asymmetry factor from the GOM is used. The absorption efficiency $\hat{Q}_a$ can be obtained by a linear combination of results from the GOM and Mie theory for the wavelengths of 8.333, 11.155 and 12.0 μm in the form

$$\begin{aligned}
\hat{Q}_a &= 2/3\hat{Q}_a GOM + 1/3\hat{Q}_a MieVS(\lambda = 8.333\mu m), \\
\hat{Q}_a &= 1/2\hat{Q}_a GOM + 1/2\hat{Q}_a MieV\ (\lambda = 11.155\mu m), \\
\hat{Q}_a &= 5/12\hat{Q}_a GOM + 7/12\hat{Q}_a MieV(\lambda = 12.0\mu m),
\end{aligned} \tag{6.5}$$

where $\hat{Q}_a GOM$, $\hat{Q}_a MieVS$ and $\hat{Q}_a MieV$ are the absorption efficiencies from the GOM, the MieVS and the MieV, respectively, for randomly oriented hexagonal particles. The coefficients for different wavelengths are empirically determined with the FDTD and the GOM results.

6.3 Single-scattering properties of cirrus clouds

In order to resolve the cirrus ice crystal size distributions, 38 size bins are used in single-scattering calculations. The length (L) and half width ($D/2$) of ice crystals, along with the length limits (L_1 and L_2) of each bin, are shown in Table 6.1. The single-scattering properties of hexagonal ice crystals at the 38 bins are calculated using different methodologies, including Mie theory, the ADT, the GOM, and the composite method at the 3 infrared wavelengths.

Figures 6.1, 6.2 and 6.3 show the extinction efficiency, absorption efficiency and asymmetry factor for randomly oriented hexagonal ice crystals, calculated using different scattering models at the wavelengths of 8.333 μm ($m = 1.2993 + 0.0370i$), 11.155 ($m = 1.1139 + 0.2910i$) and 12.0 μm ($m = 1.2798 + 0.4133i$), respectively. We can see that the CMP results are very close to the FDTD results. For the absorption efficiency which dominates the IR radiative transfer, Mie theory overestimates this quantity, while the ADT and the GOM usually underestimate it.

Using these single-scattering properties and cirrus ice crystal size distributions, we can obtain the extinction coefficient, absorption coefficient and asymmetry factor of cirrus clouds. The extinction coefficient β, absorption coefficient β_a, and asymmetry factor g of the cirrus clouds for each wavelength can be expressed by

$$\beta = \int_{L_{min}}^{L_{max}} \hat{Q}_e(L, D)\hat{P}(L, D)\, n(L)dL, \tag{6.6}$$

$$\beta_a = \int_{L_{min}}^{L_{max}} \hat{Q}_a(L, D)\hat{P}(L, D)\, n(L)dL, \tag{6.7}$$

$$g = \frac{\int_{L_{min}}^{L_{max}} \hat{g}(L, D)\hat{Q}_s(L, D)\hat{P}(L, D)\, n(L)dL}{\int_{L_{min}}^{L_{max}} \hat{Q}_s(L, D)\hat{P}(L, D)\, n(L)dL}. \tag{6.8}$$

where $n(L)$ is the size distribution of the cirrus ice crystals. L_{min} and L_{max} are the minimum and maximum lengths of ice crystals, respectively. $\hat{P}$, $\hat{Q}_e$, $\hat{Q}_a$, $\hat{Q}_s$ and $\hat{g}$ are

Table 6.1: Discretization of ice crystal sizes in the single-scattering calculations.

$L(\mu m)$	$D/2(\mu m)$	$L_1(\mu m)$	$L_2(\mu m)$
0.20000E+01	0.10000E+01	0.10000E+01	0.30000E+01
0.40000E+01	0.20000E+01	0.30000E+01	0.50000E+01
0.60000E+01	0.30000E+01	0.50000E+01	0.70000E+01
0.87500E+01	0.43750E+01	0.70000E+01	0.90000E+01
0.10000E+02	0.50000E+01	0.90000E+01	0.11000E+02
0.12000E+02	0.60000E+01	0.11000E+02	0.13000E+02
0.16000E+02	0.80000E+01	0.13000E+02	0.19000E+02
0.20000E+02	0.10000E+01	0.19000E+02	0.21000E+02
0.25000E+02	0.12500E+02	0.21000E+02	0.33500E+02
0.37500E+02	0.18750E+02	0.33500E+02	0.37500E+02
0.50000E+02	0.20000E+02	0.37500E+02	0.62500E+02
0.75000E+02	0.30000E+02	0.62500E+02	0.87500E+02
0.10000E+03	0.25000E+02	0.87500E+02	0.11250E+03
0.12500E+03	0.31250E+02	0.11250E+03	0.13750E+03
0.15000E+03	0.37500E+02	0.13750E+03	0.16250E+03
0.17500E+03	0.43750E+02	0.16250E+03	0.18750E+03
0.20000E+03	0.50000E+02	0.18750E+03	0.21250E+03
0.22500E+03	0.38250E+02	0.21250E+03	0.23750E+03
0.25625E+03	0.43562E+02	0.23750E+03	0.27500E+03
0.30000E+03	0.51000E+02	0.27500E+03	0.32500E+03
0.35000E+03	0.59500E+02	0.32500E+03	0.37500E+03
0.40000E+03	0.68000E+02	0.37500E+03	0.42500E+03
0.45000E+03	0.76500E+02	0.42500E+03	0.47500E+03
0.51250E+03	0.56375E+02	0.47500E+03	0.55000E+03
0.60000E+03	0.66000E+02	0.55000E+03	0.65000E+03
0.70000E+03	0.77000E+02	0.65000E+03	0.75000E+03
0.80000E+03	0.88000E+02	0.75000E+03	0.85000E+03
0.90000E+03	0.99000E+02	0.85000E+03	0.95000E+03
0.10000E+04	0.11000E+03	0.95000E+03	0.10500E+04
0.11000E+04	0.12100E+03	0.10500E+04	0.11500E+04
0.12000E+04	0.13200E+03	0.11500E+04	0.12500E+04
0.13000E+04	0.14300E+03	0.12500E+04	0.13500E+04
0.14250E+04	0.15675E+03	0.13500E+04	0.15000E+04
0.16000E+04	0.17600E+03	0.15000E+04	0.17000E+04
0.18000E+04	0.19800E+03	0.17000E+04	0.19000E+04
0.20500E+04	0.22550E+03	0.19000E+04	0.22000E+04
0.24500E+04	0.26950E+03	0.22000E+04	0.27000E+04
0.31000E+04	0.34100E+03	0.27000E+04	0.35000E+04

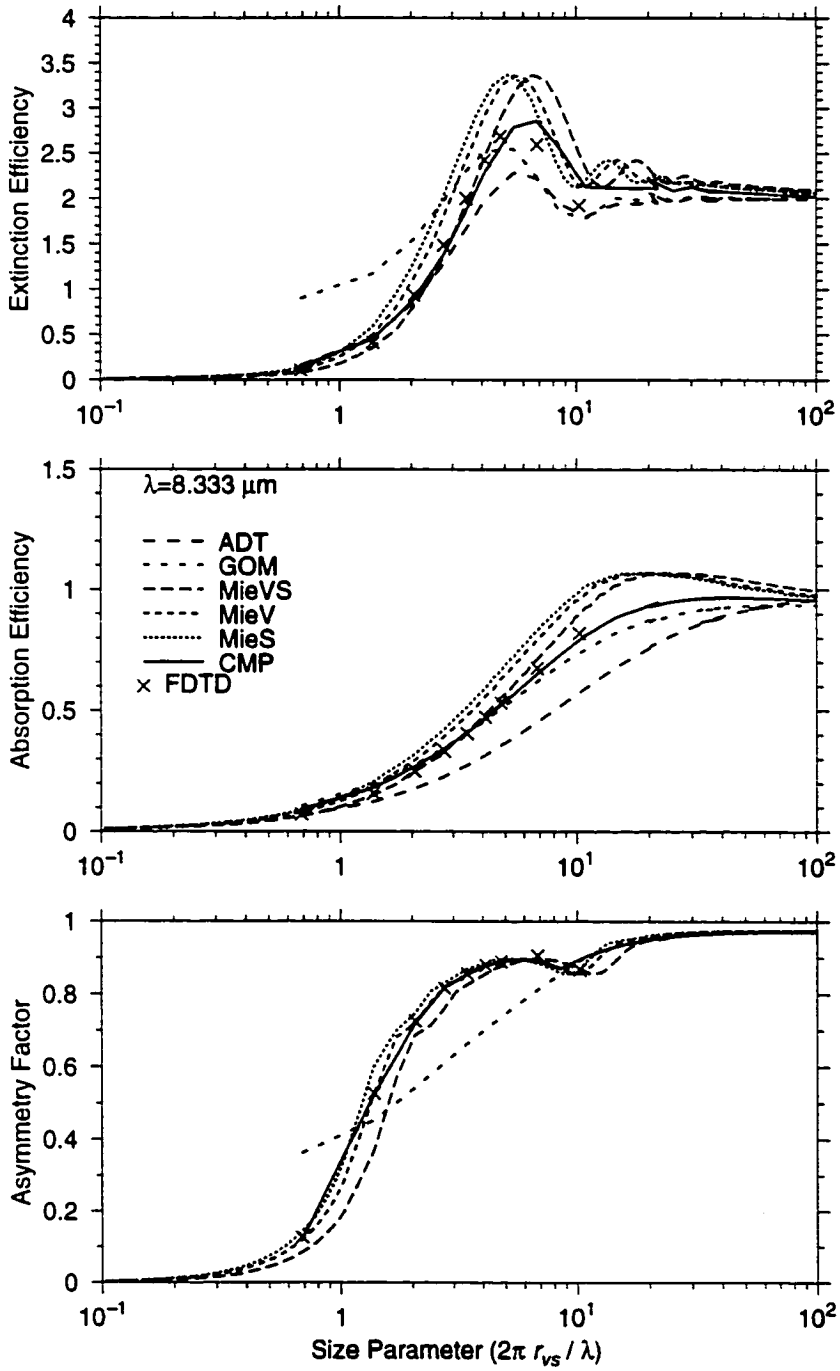

Figure 6.1: The extinction efficiency, absorption efficiency, and asymmetry factor for randomly oriented hexagonal ice crystals, calculated using different scattering models at a wavelength of 8.333 μm ($m = 1.2993 + 0.0370i$).

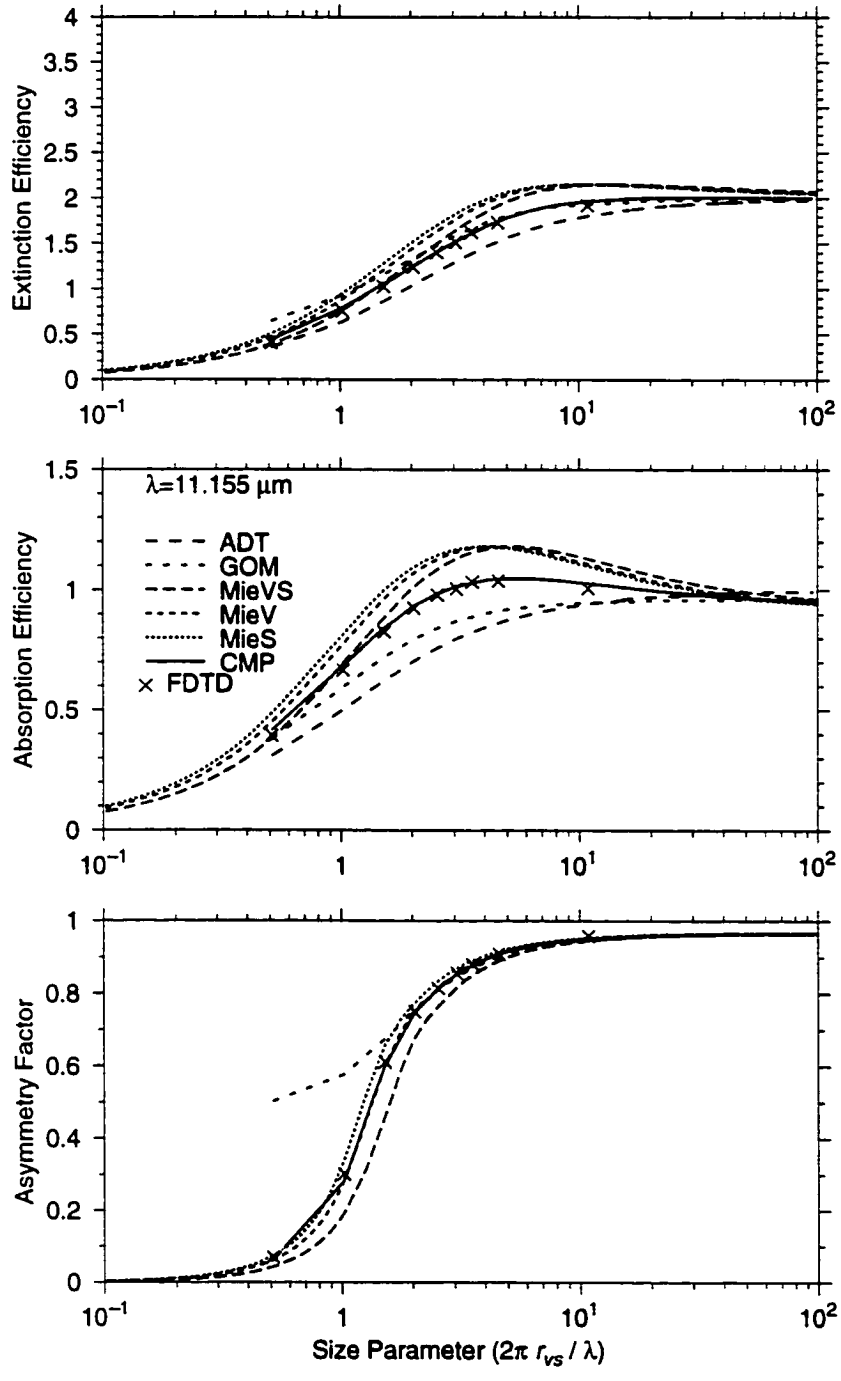

Figure 6.2: Same as Fig.6.1, but at the wavelengths of 11.155 μm ($m = 1.1139 + 0.2910i$).

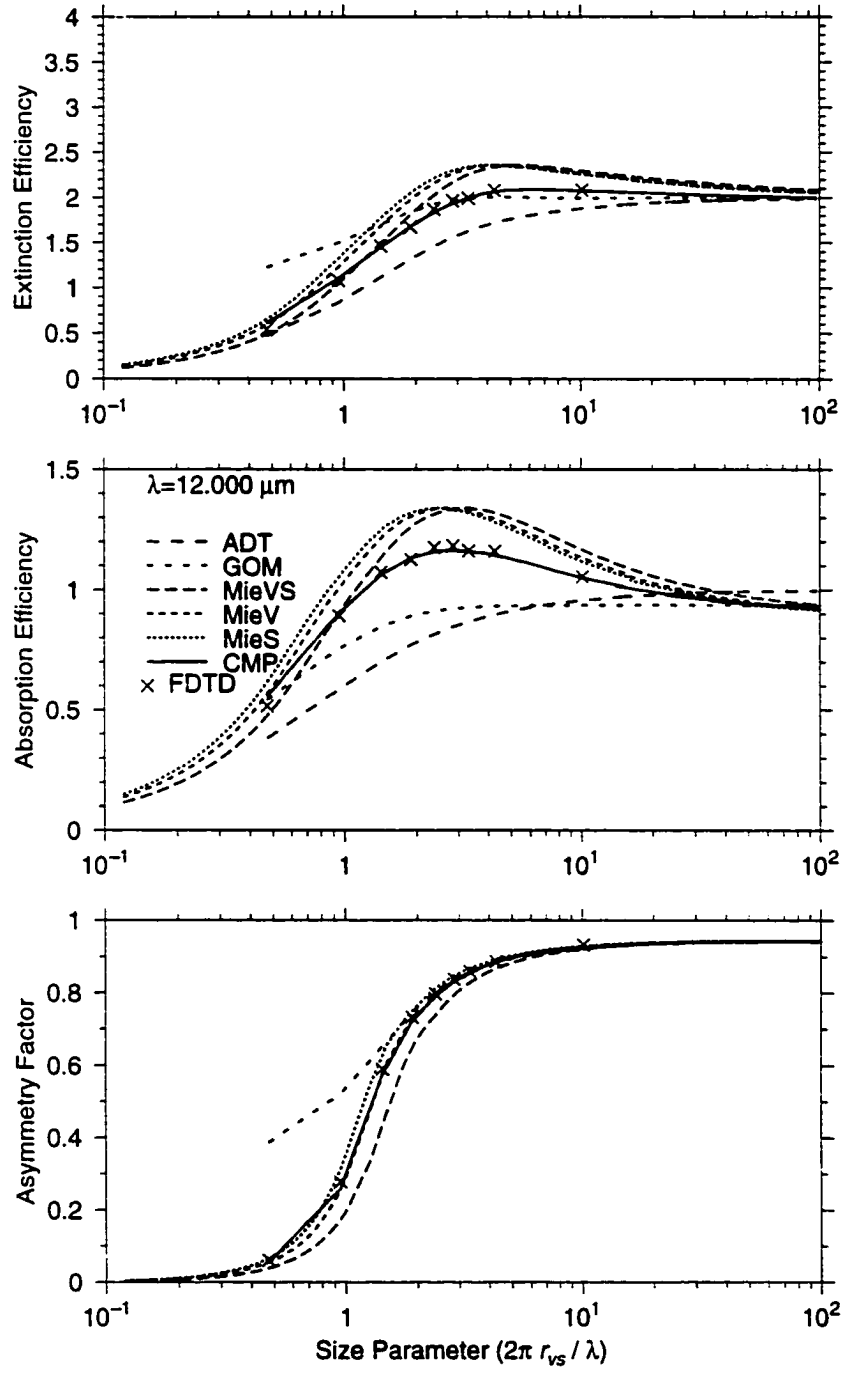

Figure 6.3: Same as Fig. 6.1, but at at the wavelengths of 12.0 μm ($m = 1.2798 + 0.4133i$).

the projected area, extinction efficiency, absorption efficiency, scattering efficiency, and asymmetry factor, respectively, for randomly oriented hexagonal ice crystals.

By assuming that the ice crystals are hexagonal, the ice water content (IWC) and generalized effective size (D_{ge}) are defined as (Fu 1996)

$$IWC = \frac{3\sqrt{3}}{8}\rho_i \int_{L_{min}}^{L_{max}} DDLn(L)dL, \tag{6.9}$$

and

$$D_{ge} = \frac{\int_{L_{min}}^{L_{max}} DDLn(L)dL}{\int_{L_{min}}^{L_{max}} (DL + \frac{\sqrt{3}}{4}D^2)n(L)dL} \tag{6.10}$$

where ρ_i is the density of pure ice, which is $0.9167 gcm^{-3}$. As shown in Fu (1996) and Fu *et al.* (1998), the radiative properties of cirrus clouds can be parameterized in terms of IWC and D_{ge} in climate models. While the IWC is a prognostic variable in most of climate models, little is known about the global distribution of D_{ge}. Therefore, it is a subject of active research to retrieve D_{ge} from satellite measurements.

6.4 Comparison of brightness temperature at TOA simulated using different scattering models

Using the single-scattering properties obtained from different scattering models, we employ a discrete ordinate radiative transfer program developed by Stamnes *et al.* (1988) to calculate the upward IR radiance at TOA. Corresponding to the 3 wavelengths at which the single-scattering properties are calculated, we use 3 spectral bandwidths (8.3-8.4, 11.06-11.25, and 11.93-12.06 μm) (Ackerman *et al.* 1990) to calculate the mean IR radiance within each band. We use 32 streams and midlatitude summer temperature profile. A single layer of cirrus cloud with different thickness and location is considered, which is put between 8.0-8.5, 8.0-9.0, 8.0-10.0, 8.0-12.0, 8.5-12.5, 10.5-12.5, 11.5-12.5 and 12.0-12.5 km.

The 28 ice crystal size distributions adopted in Fu (1996) and other 2 size distributions used by Mitchell *et al.* (1996) are used in the present study. These were based on *in situ* aircraft observations from both midlatitude and tropical regions. In order to include the potential effects of small ice crystals that may exist in cirrus clouds on the infrared, all 30 ice crystal size distributions are extrapolated to 1.0 μm following Eq. (2) of Mitchell *et al.* (1996), which is

$$N_s(L) = N_{0s} exp(-\alpha_s L) \tag{6.11}$$

where L is the maximum dimension of the ice particles (particle length), α_s is the slope parameter, and N_{0s} is a normalizing factor. The extrapolated 30 ice crystal size distributions are shown in Figs. 6.4 and 6.5. These size distributions are discretized in 38 bins as shown in Table 6.1 to resolve the structure of the spectra. The ice water content and the generalized mean effective size of these extrapolated size distributions are given in Table 6.2. Because of the extrapolation, the ice water content and the generalized mean effective size shown in Table 6.2 may be different from those in Fu (1996).

Figures 6.6 and 6.7 show the comparison of the upward brightness temperatures at TOA obtained from Mie theory, the ADT and the GOM with those from the CMP. The difference can reach as large as $7K$. Large differences usually occur when cirrus cloud particle mean effective sizes are small. We can see that the MieV, ADT, and GOM generally overestimate the upward brightness temperature but the MieS and MieVS underestimate it. This may make significant difference in the retrieved cirrus particle size. Therefore, to accurately retrieve the physical properties of cirrus clouds, nonsphericity of ice crystals must be accounted for and an accurate light scattering model is necessary.

Figure 6.8 shows the scatter diagram of brightness temperature difference (BTD) between 8.333 and 11.155 μm versus BTD between 11.155 and 12.0 μm, calculated using scattering properties from Mie theory, the ADT, the GOM and the CMP. The

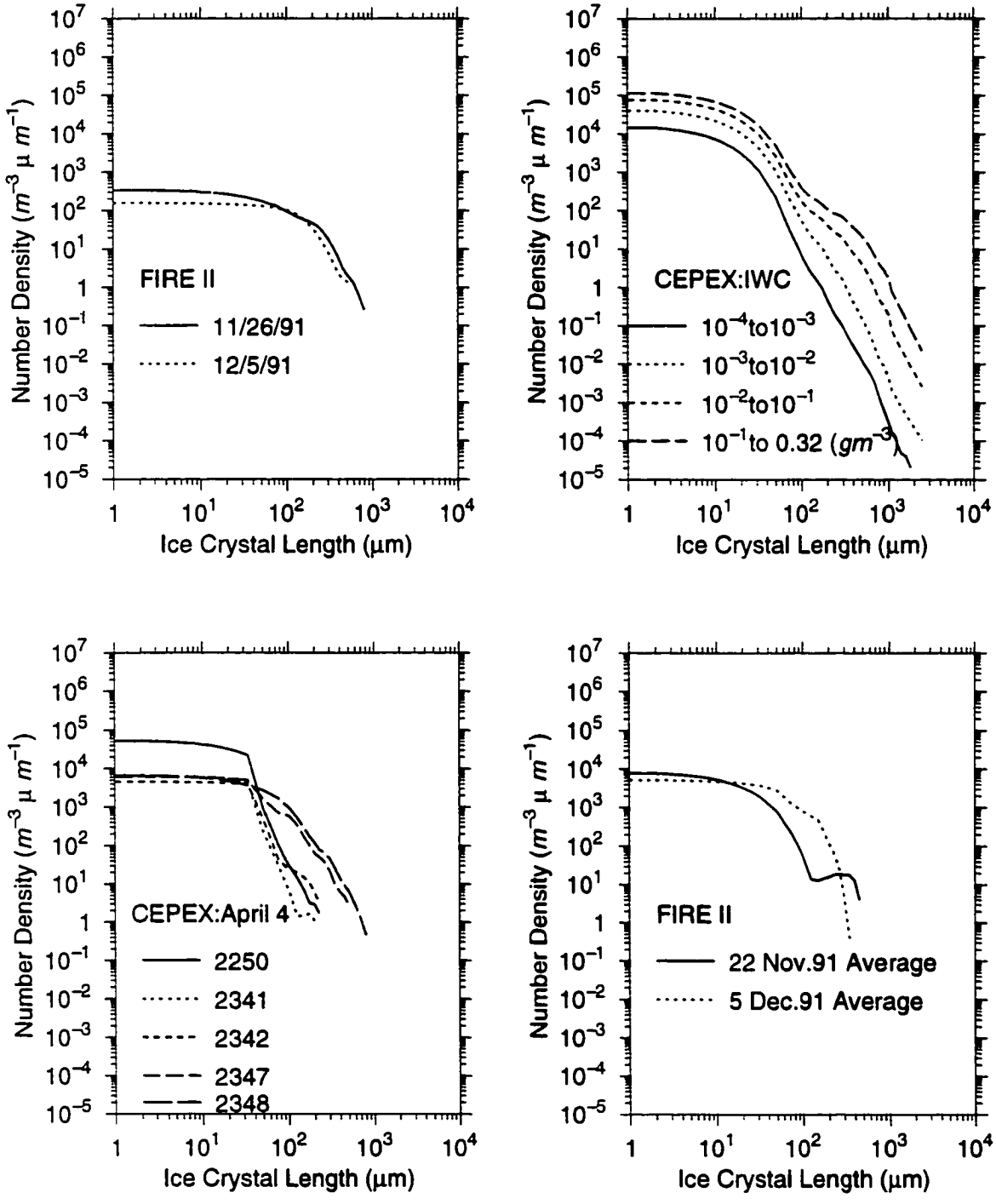

Figure 6.4: Extrapolated cirrus cloud particle size distributions based on *in situ* aircraft observations.

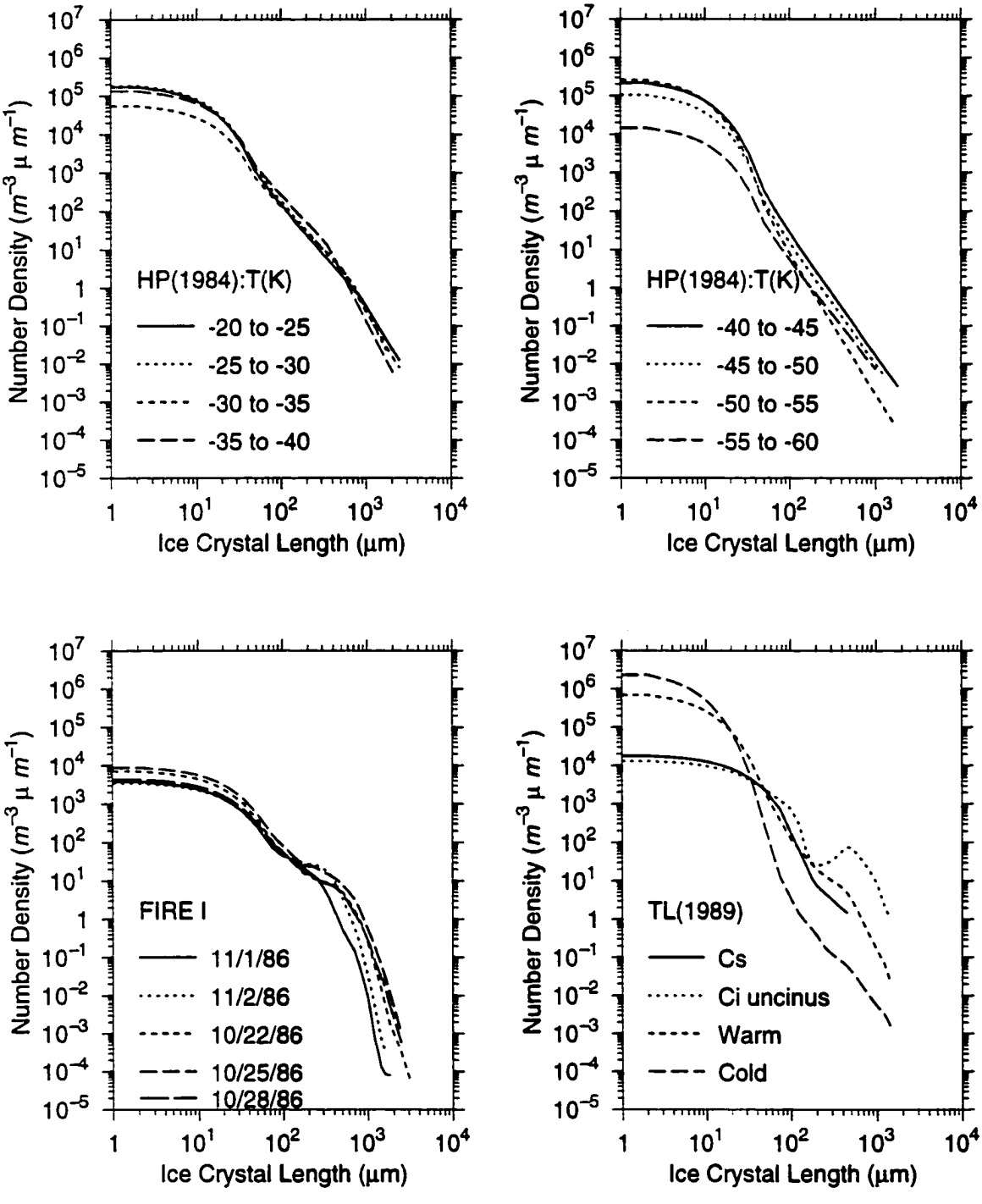

Figure 6.5: Same as Fig. 6.4, but for different size distributions.

Table 6.2: Characteristics of the 30 measured ice crystal size distributions.

Particle size distribution	IWC (gm^{-3})	D_{ge} (μm)
	HP (1984): T (K)	
-20 to -25	0.2933E-01	0.6361E+02
-25 to -30	0.2657E-01	0.5098E+02
-30 to -35	0.2567E-01	0.7772E+02
-35 t0 -40	0.2838E-01	0.5063E+02
-40 to -45	0.4362E-02	0.2116E+02
-45 to -50	0.2157E-02	0.2076E+02
-50 to -55	0.2147E-02	0.1399E+02
-55 to -60	0.6424E-03	0.2943E+02
	FIRE I	
11/01/86	0.5822E-02	0.6411E+02
11/02/86	0.1644E-01	0.8598E+02
10/22/86	0.1895E-01	0.9556E+02
10/25/86	0.3535E-01	0.1062E+03
10/28/86	0.1868E-01	0.1027E+03
	TL (1989)	
Cs	0.1066E-01	0.3638E+02
Ci uncinus	0.2848E+00	0.1297E+03
Warm	0.2656E-01	0.2926E+02
Cold	0.8551E-02	0.1072E+02
	FIRE II	
11/26/91	0.1494E-01	0.8031E+02
12/05/91	0.8362E-02	0.6984E+02
	CEPEX: IWC (gm^{-3})	
10^{-4} to 10^{-3}	0.9386E-03	0.2267E+02
10^{-3} to 10^{-2}	0.5275E-02	0.2936E+02
10^{-2} to 10^{-1}	0.2990E-01	0.5255E+02
0.1 to 0.32	0.1282E+00	0.8369E+02
	CEPEX: April 4	
2250	0.7762E-02	0.1922E+02
2341	0.1566E-02	0.2063E+02
2342	0.2542E-02	0.2798E+02
2347	0.2617E-01	0.5408E+02
2348	0.5237E-01	0.6090E+02
	FIRE II (Average)	
11/22/91	0.1308E-01	0.6681E+02
12/05/91	0.3398E-01	0.4990E+02

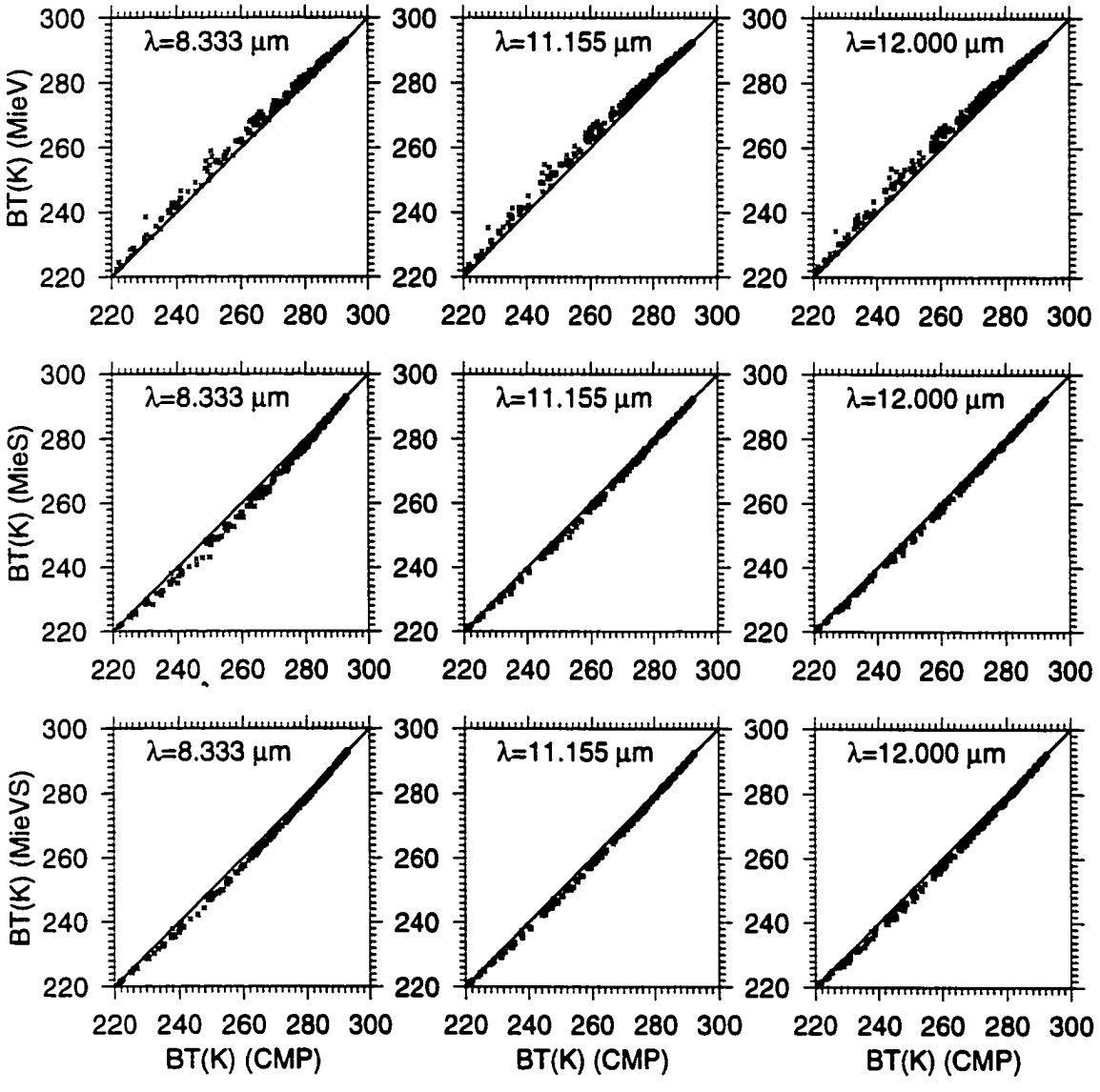

Figure 6.6: Comparisons of upward brightness temperatures using cirrus single-scattering properties derived from Mie theory with those from the CMP.

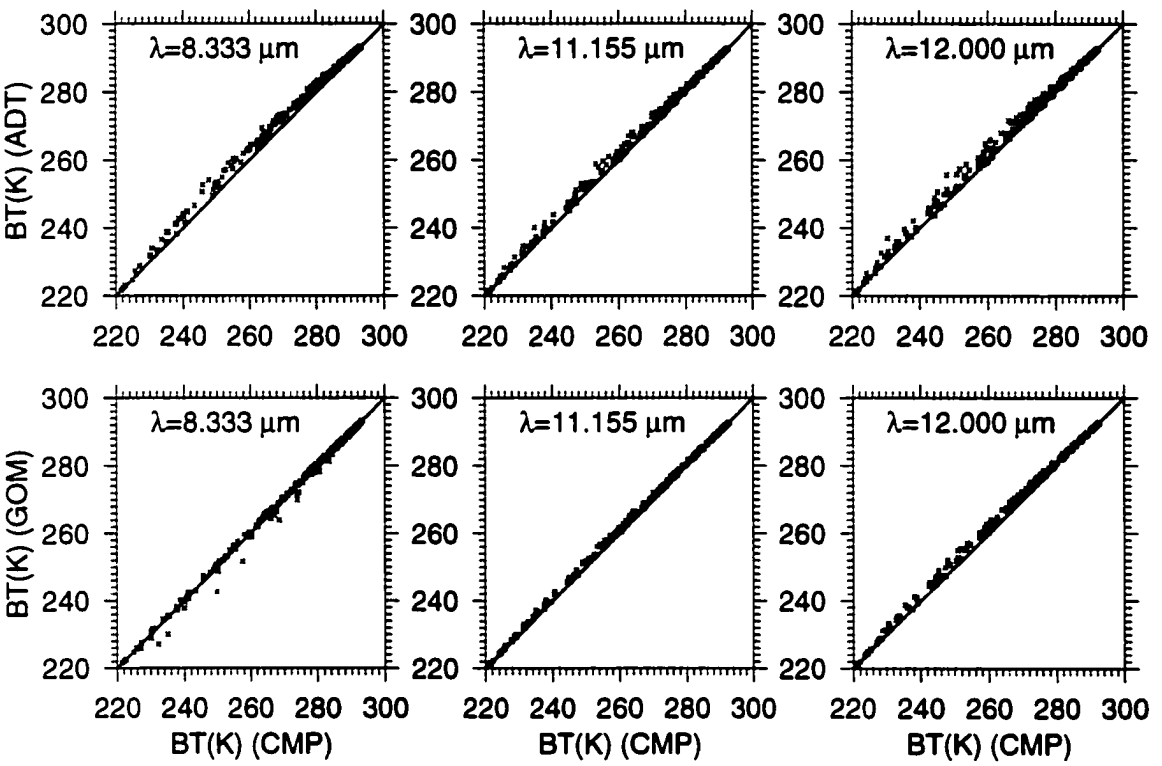

Figure 6.7: Comparisons of upward brightness temperatures using cirrus single-scattering properties derived from the ADT and the GOM with those from the CMP.

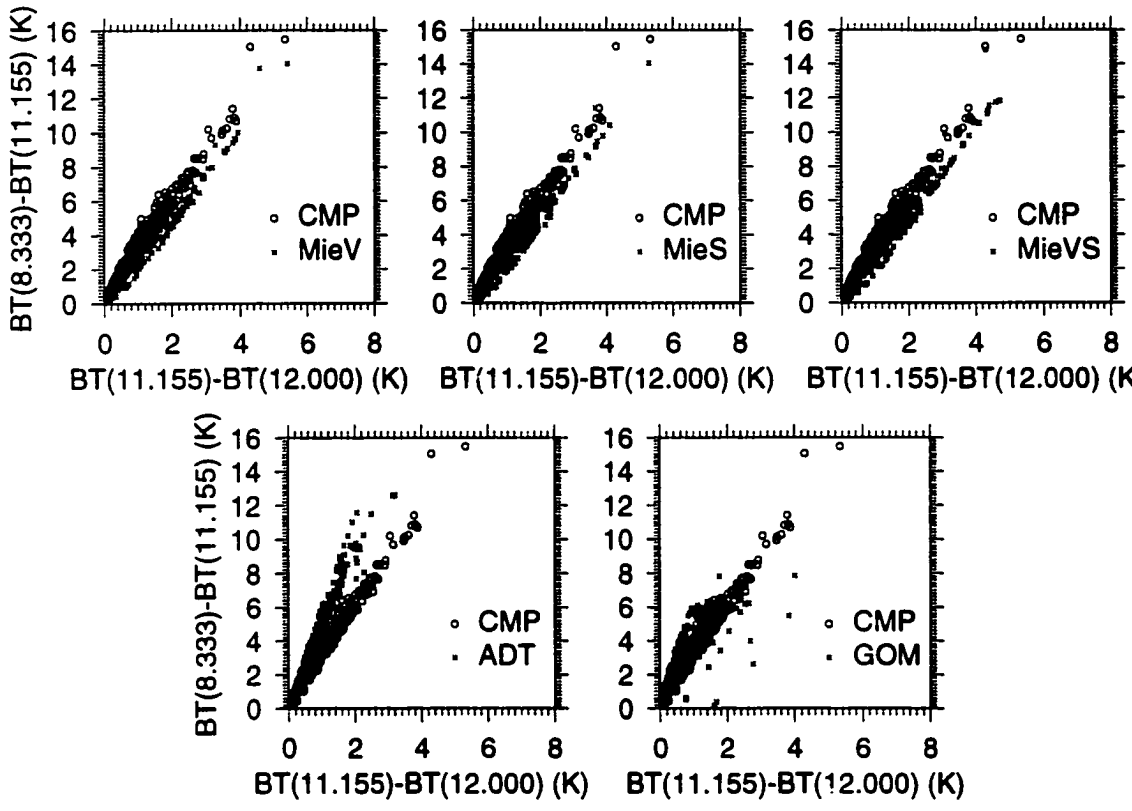

Figure 6.8: The scatter diagram of brightness temperature difference (BTD) between 8.333 and 11.155 μm versus BTD between 11.155 and 12.0 μm, calculated with scattering properties from Mie theory, the ADT, the GOM and the CMP.

BTD is used in the remote sensing for cirrus clouds to identify cloud types and cloud particle sizes and shapes (Takano *et al.* 1992). In Fig. 6.8, for 8 different cloud locations and 30 size distributions, each panel consists of 240 points corresponding to each scattering model. We can see that the results from Mie theory, the ADT and the GOM all deviate significantly from the CMP results. The CMP points are generally between those from Mie theory and the ADT. Again, we can conclude that the light scattering models used can alter the remote sensing results.

6.5 Sensitivity of retrieved cirrus particle size to the single-scattering models

Physical properties of cirrus clouds have been studied with satellite or aircraft measurements by several authors. For example, Strabala and Ackerman (1994) used a trispectral combination of observations at 8, 11 and 12 μm bands to detect cloud and cloud phase. On the remote sensing for the microphysical properties of cirrus clouds, Han *et al.* (1997) retrieved ice crystal sizes with a radiative transfer model treating ice crystals as hexagonal columns. Baran *et al.* (1998) and Holz *et al.* (1998) retrieved ice crystal sizes using the simplified anomalous diffraction theory (SADT) (Bryant and Latimer 1969) as the scattering model.

It has been claimed that the interpretation of infrared radiometric measurements based on Mie theory significantly underestimates the cirrus ice crystal sizes (Baran *et al.* 1998). By applying Mie theory to equivalent ice spheres for the calculation of the infrared absorption coefficients at wavelengths between 8 and 12 μm, the maximum ice crystal size that can be retrieved is about 30 μm (Strabala *et al.* 1994). Beyond this size range the spectral variation of the scattering and absorption properties is not significant. Therefore, if the cirrus cloud is dominated by large particles, no reliable retrieval of the size information can be obtained by using these wavelengths. To reconcile the retrieved particle size with the *in situ* measurements, people usually use the simplified ADT to calculate the scattering and absorption properties of

nonspherical particles such as hexagonal ice crystals (Baran *et al.* 1998; Holz *et al.* 1998). Due to the error of the approximation, the simplified ADT can produce much smaller absorption efficiencies than those from other scattering methods. Therefore, using the absorption efficiency from the simplified ADT, one can then obtain much larger retrieved particle size.

Reliable retrieval of microphysical properties of cirrus clouds requires accurate calculation of the single-scattering properties of nonspherical particles. Because in the calculation of single scattering properties, even for hexagonal columns, the ADT still results in significant errors, there is reason to believe that using the SADT as scattering model may also cause significant bias in the retrieved quantities. Here we first examine the sensitivity of retrieved particle size to the scattering model and then explore the limitations of the retrieval method by using the infrared window channels.

Differences in cirrus emissivity between the wavelengths 8.333 and 11.155 μm are used to retrieve ice crystal size in this study. Following Holz *et al.* (1998), the emissivity at 11.155 μm and the ratio of the emissivities at 8.333 and 11.155 μm are used to establish a lookup table. To build up a lookup table to retrieve the mean effective particle size D_{ge} of a layer of cirrus cloud, we assume a particle size distribution $n(L)$ in the form (Mitchell *et al.* 1996)

$$N_s(L) = N_{0s} exp(-\alpha_s L), \tag{6.12a}$$

$$N_l(L) = N_{0l} L^{\nu} exp(-\alpha_l L), \tag{6.12b}$$

$$n(L) = N_s(L) + N_l(L), \tag{6.12c}$$

where ν = 2-2exp[-($\bar{L}_l$/100 μm)^3], is a parameter quantifying the deviation of the distribution from exponential behavior. L denotes the maximum dimension of the particles. $\alpha_s = 1/\bar{L}_s$ and $\alpha_l = (\nu + 1)/\bar{L}_l$ define the size distribution slopes of the small- and large-particle modes. $\bar{L}_s$ denotes the mean maximum dimension from the contribution of small ice crystals and is fixed to 25.32 μm (α_s = 395 cm^{-1}) (Mitchell *et al.* 1996). $\bar{L}_l$ is the mean maximum dimension for the large ice crystal mode and

can be varied. A minimum in the bimodal size distribution exists in the region where (6.12a) and (6.12b) overlap. The L corresponding to this minimum is estimated as $L_* = 0.2927\bar{L}_s + 72.0$. Knowing $N_l(L)$ at L_* via (6.12b), $N_s(L_*)$ is estimated to be $N_l(L_*)/2$. Therefore, $N_{0s} = 0.5N_l(L_*)exp(\alpha_s L_*)$.

By varying $\bar{L}_l$ from a small value to a large value, we can obtain a series of size distributions. Using the absorption efficiency calculated by a scattering model, we can calculate the cloud emissivity ϵ in the form

$$\epsilon = 1.0 - \exp(-\beta_a z/\mu), \tag{6.13}$$

where z denotes the cloud thickness, μ denotes the cosine of the radiance zenith angle. Using Eq.(6.10), we can calculate the mean effective particle size (D_{ge}) related to each size distribution. Therefore, using the emissivity values and the corresponding D_{ge}, we can build up a lookup table corresponding to the used light scattering model. For example, shown in Fig. 6.9 are some curves in the lookup tables based on the single-scattering properties from the ADT, CMP, GOM, MieS, MieV and MieVS.

Figure 6.10 shows the comparison of the retrieved D_{ge} based on the lookup tables from the ADT, CMP, GOM, MieV, MieS and MieVS light scattering models with the D_{ge} of the simulated cirrus clouds. The clouds are simulated by using the bimodal size distributions. The cloud emissivities are calculated by using Eq.(6.13) with absorption properties from the CMP. For this retrieval, a given cloud emissivity of 0.5 at 11.155 μm is used. We can see that the retrieved particle sizes based on the ADT are generally much larger than the actual values. Both the GOM and ADT ignore the tunneling effect, but the GOM doesn't overestimate the particle sizes, because of the big differences in the absorption efficiencies between the GOM and ADT at 8.333 μm. The GOM results are close to the Mie results, which underestimate the particle sizes. We may conclude that the tunneling effect cannot explain the big differences between the retrieved particle sizes based on the ADT and other scattering models. It is the errors of the ADT in absorption which make the difference. For large particles, we

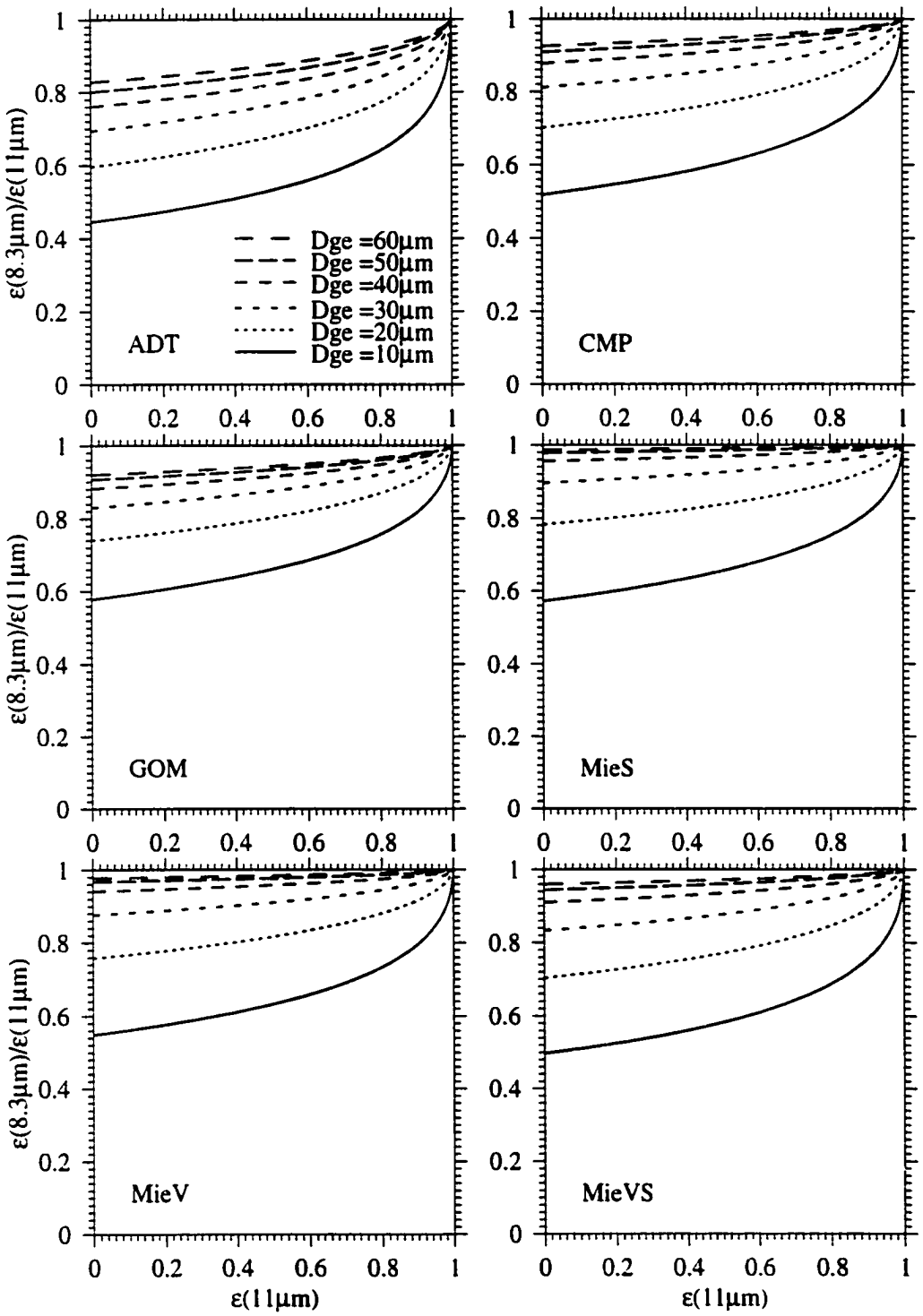

Figure 6.9: Emissivity ratio between 8.333 and 11.155 μm as a function of the emissivity at 11.155 μm for a cirrus cloud composed of hexagonal ice crystals with bimodal size distributions. The different curves correspond to various effective sizes (D_{ge}). The used light scattering models include ADT, CMP, GOM, MieS, MieV and MieVS.

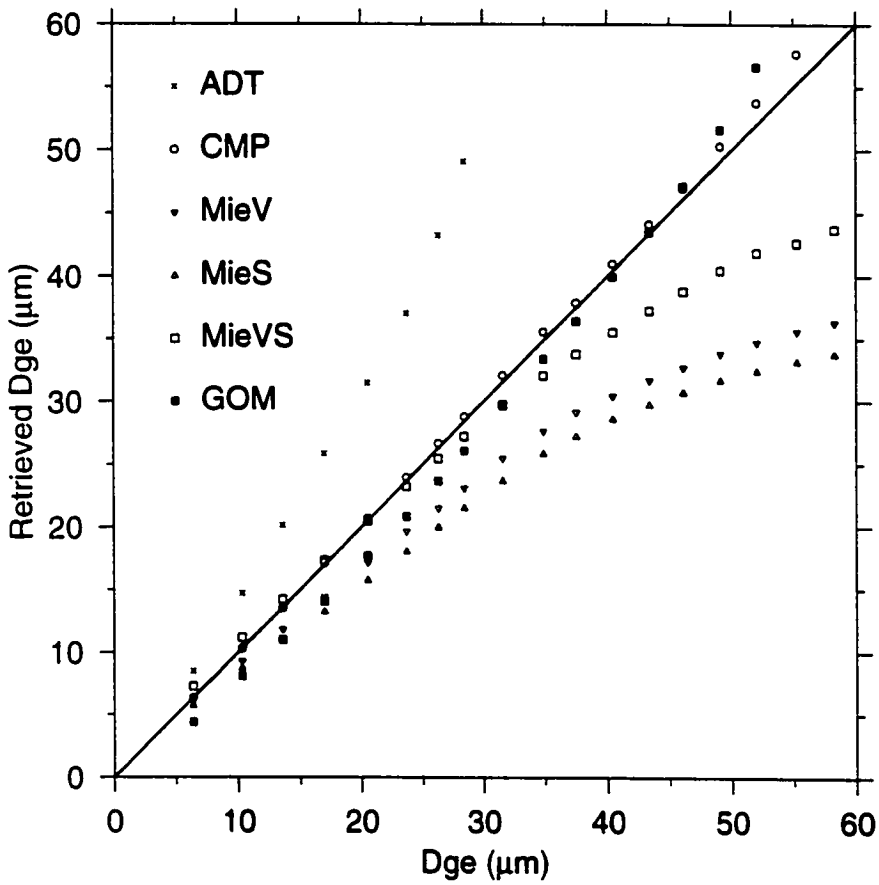

Figure 6.10: Comparisons of the retrieved D_{ge} based on the lookup tables from the ADT, CMP, GOM, MieV, MieS and MieVS light scattering models with the D_{ge} of the simulated clouds.

can see in Fig. 6.10 that the retrieval is unstable, because the emissivity difference between 8.333 and 11.155 μm is very small now.

Figure 6.11 shows the comparison of the retrieved D_{ge} based on the lookup table from the CMP light scattering model with the actual D_{ge} of the 30 measured size distributions. The emissivities of the cirrus clouds simulated by the 30 size distributions are calculated by using Eq.(6.13) with absorption properties from the CMP. The given cloud emissivity of 0.5 at 11.155 μm is also used. In this study, to avoid saturation in emissivity, the emissivity at 11.155 μm and the emissivity ratio between 8.333 and 11.155 μm are limited to be smaller than 0.95. Therefore, results from some size distributions with D_{ge} larger than 90 are not shown here. We find that the retrieved is reliable only for actual D_{ge} smaller than 30 μm. For larger D_{ge}, the retrieved are generally much smaller than the actual values. Therefore, for clouds dominated by large particles, this particle-size retrieval method does not work. Using the ADT to calculate single-scattering properties results in larger retrieved particle sizes, but this is due to the error of the ADT in the calculation of the absorption properties.

6.6 Summary and conclusions

Using the single-scattering properties derived from the ADT, Mie theory, and the CMP methods, the cirrus spectral brightness temperatures at wavelengths of 8.333, 11.155 and 12.0 μm are computed. The CMP methods are based on the FDTD for nonspherical particles with small size parameters and the GOM for particles with large size parameters, which can be considered as the reference calculation. We find that using the ADT and Mie theory can introduce significant errors in the upward brightness temperature, which can be as large as about $7K$ for some cirrus clouds. This implies that the retrieval of cirrus properties using these IR channels must accurately consider the nonsphericity of ice crystals and use accurate light scattering models for scattering property calculation.

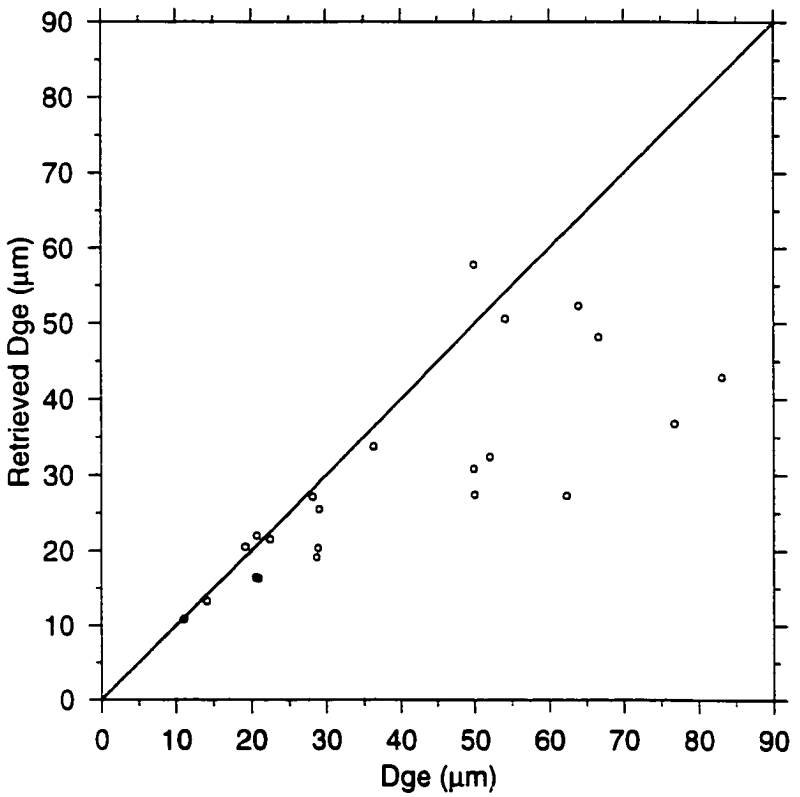

Figure 6.11: Comparisons of the retrieved D_{ge} based on the lookup table from the CMP light scattering model with the actual D_{ge} of cirrus clouds.

Using the spectral variation of the single-scattering properties in the 8-12 μm window, the mean effective size (D_{ge}) of a layer of cirrus cloud is often retrieved from the measured radiance/brightness temperature. However, the limitation of this retrieval is that when particles larger than about 30 μm dominate the cloud, the spectral variation of the single-scattering properties in the 8-12 μm window becomes insignificant. The necessary information for a successful retrieval, which is only significant for small particles, is "submerged" by the effect of large particles. Therefore, the retrieval based on the variation of the single-scattering properties will collapse under this condition. Using the anomalous diffraction theory for the retrieval may result in much larger retrieved particle sizes, but these are not reliable values.

Chapter 7

Conclusions

The major objective of this study is to develop accurate solutions for light scattering by nonspherical dielectric particles and to examine the accuracy of the approximate approaches in light scattering by cirrus ice crystals. Following these goals, a three dimensional (3D) finite-difference time domain (FDTD) program is developed to provide numerical solutions for light scattering by dielectric particles with arbitrary shapes and composition. The perfectly matched layer (PML) absorbing boundary condition (ABC) is used to truncate the computational domain. We show that the 3D PML FDTD model can work very well for particles with $m_r x$ as large as 40, where m_r denotes the real refractive index and x denotes the size parameter of the particle. For particles with large complex refractive indices, the 3D PML FDTD model also works well but with larger errors in the calculation of extinction and absorption efficiencies. The FDTD scheme is also extended to simulate light propagation in dielectric media with particles embedded. Due to the difficulties in near to far field transformation for this case, only near field is produced and compared with exact result. Moreover, the present 3D PML FDTD model not only shows very good stability and accuracy; it also requires much less computer memory. By observing the performance of this FDTD model for a wide range of size parameters, we believe that it can be applied to very large scatterers of arbitrary shapes with high accuracy when the computing resources are available in the future.

The 3D PML FDTD model is used to investigate the scattering patterns by particles with various morphologies. It is also used to examine the accuracy of the traditional approaches including Mie theory, the ADT, and the geometrical optics method (GOM), for the calculation of the light scattering and absorption properties of hexagonal ice crystals in cirrus clouds. It is found that, for randomly oriented nonspherical particles, using Mie theory for equivalent ice spheres tends to overestimate the absorption efficiency while the ADT and the GOM tend to underestimate it.

For the simulation of light scattering by nonspherical dielectric particles, a frequently used approximation is the anomalous diffraction theory (ADT). In this study, an analytical ADT model for light scattering by arbitrarily oriented hexagonal and cylindrical particles is developed. The accuracy of the ADT model is determined by the size parameter and refractive index conditions under which it is valid. Use of this method should be checked with accurate methods such as Mie theory, the T-matrix method, the discrete dipole approximation, and the finite-difference time domain technique. The differences between the ADT using the original notation and the simplified ADT are also discussed. We find significant differences between the results from the ADT using the original notation and those from the simplified ADT solutions.

Another objective of this study is to apply the accurate light scattering models to examine the methods to retrieve cirrus optical and microphysical properties by creating a data processing model for satellite remote sensing of cirrus clouds. In this study, we find that with different light scattering models, the difference in the model-simulated infrared brightness temperature can be as large as $7K$, which implies that different light scattering models may cause significant difference in the retrieved cirrus particle sizes. The validity of using two or three wavelengths in the atmospheric window to retrieve cirrus particle sizes is investigated. Unfortunately, it is found that the retrieval method is limited by the actual cirrus particle sizes. The cirrus particle sizes from the retrieval based on two or three infrared wavelengths in the atmospheric window are only reliable when D_{ge} is smaller than 30 μm.

References

Ackerman, S.A., and G.L. Stephens, 1987: The absorption of solar radiation by cloud droplets: an application of anomalous diffraction theory. J. Atmos. Sci. **44**, 1574-1588.

Ackerman, S.A., W.L. Smith, J.D. Spinhirne, and H.E. Revercomb, 1990: The 27-28 October FIRE IFO cirrus case study: Spectral properties of cirrus clouds in the 8-12 μm window. Mon. Wea. Rev. **118**, 2377-2388.

Arnott, W.P., Y.Y. Dong, J. Hallet and M.R. Poellot, 1994: Role of small ice crystals in radiative properties of cirrus: a case study, FIRE II, November 22, 1991. J. Geophys. Res. **99**, 1371-1381.

Arnott, W.P., Arnott, Y. Liu, and J. Hallet, 1997: Unreasonable effectiveness of mimicking measured infrared extinction by hexagonal ice crystals with Mie ice spheres. Optical Remote Sensing of the Atmosphere, Technical Digest Series (Optical Society of America, Washington, D.C.),**5**, 216-218.

Asano, S., and G. Yamamoto, 1975: Light scattering by a spheroidal particle. Appl. Opt. **14**, 29-49.

Auer Jr., A.H., and D.L. Veal, 1970: The dimension of ice crystals in natural clouds. J. Atmos. Sci. **27**, 919-926.

Baran, A.J., J.S. Foot, and D.L. Mitchell, 1998: Ice-crystal absorption: a comparison between theory and implications for remote sensing. Appl. Opt. **37**, 2207-2215.

Barber, P., and C. Yeh, 1975: Scattering of electromagnetic waves by arbitrarily shaped dielectric bodies. Appl. Opt. **14**, 2864-2872.

Barber, P.W., and S.C. Hill, 1990: Light scattering by particles: Computational methods. World Scientific, Singapore.

Barth, M.J., R.R. Mcleod, and R.W. Ziolkowski, 1992: A near and far-field projection algorithm for finite-difference time domain codes. J. Electromagnetic Waves and Applications **6**, 5-18.

Battan, L.J., 1973: Radar observation of the atmosphere. The University of Chicago press.

Bayliss, A., and E. Turkel, 1980: Radiation boundary conditions for wave-like equations. Commun. Pure Appl. Math. **33**, 707-725.

Berenger, J.P., 1994: A perfectly matched layer for the absorption of electromagnetic waves. J. Computational Physics **114**, 185-200.

Berenger, J.P., 1996: Three-dimensional perfectly matched layer for the absorption of electromagnetic waves. J. Computational Physics **127**, 363-379.

Bohren, C.F., and D.P. Gilra, 1979: Extinction by a spherical particle in an absorbing medium. J. Colloid and Interface Sci **72**, 215-221.

Bohren, C.F., and D.R. Huffman, 1983: Absorption and scattering of light by small particles. Wiley-interscience, New York.

Bryant, F.D., and P. Latimer, 1969: Optical efficiencies of large particles of arbitrary shape and orientation. J. Coll. Int. Sci. **30**, 291-304.

Cai, Q., and K. N. Liou, 1982: Polarized light scattering by hexagonal ice crystals: theory. Appl. Opt. **21**, 3569-3580.

Chen, H.Y., and M.F. Islander, 1990: Light scattering and absorption by fractal agglomerate and coagulations of smoke aerosols. J. Mod. Opt. **37**, 171-181.

Chiappetta, P., 1980: Multiple scattering approach to light scattering by arbitrarily shaped particles. J. Phys. A **13**, 2101-2108.

Chýlek, P., 1977: Light scattering by small particles in an absorbing medium. J. Opt. Soc. Am. **67**, 561-563.

Chýlek, P., and V. Srivastava, 1983: Dielectric constant of a composite inhomogeneous medium. Phys. Rev. B **27**, 5098-5106.

Chýlek, P., and J.D. Klett, 1991a: Absorption and scattering of electromagnetic radiation by prismatic columns: anomalous diffraction approximation. J. Opt. Soc. **8**, 1713-1720.

Chýlek, P., and J.D. Klett, 1991b: Extinction cross-sections of nonspherical particles in the anomalous diffraction approximation. J. Opt. Soc. **8**, 274-281.

Dobbie, J.S., and P. Chýlek, 1998: Evaluation of effective medium theory for large inclusions using DDA. Conference on Light Scattering by Nonspherical Particles, American Meteorology Society, New York (29 September-1 October 1998).

Draine, B. T., 1988: The discrete-dipole approximation and its application to interstellar graphite grains. Astrophys. J. **333**, 848-872.

Draine, B.T., and P.J. Flatau, 1994: Discrete-dipole approximation for calculations. J. Opt. Soc. Am. A **11**, 1491-1499.

Draine, B.T., 1998: The discrete dipole approximation for studying light scattering by irregular targets. Proceedings of Conference on Light Scattering by Nonspherical Particles (American Meteorology Society, Boston, 1998).

Engquist, B., and A. Majda, 1971: Absorbing boundary conditions for the numerical simulation of waves. Math. Comp. **31**, 629-651.

Flatau, P. J., G. L. Stephens, and B. T. Draine, 1990: Light scattering by rectangular solids in the discrete-dipole approximation: a new algorithm exploiting the block-toeplitz structure. J. Opt. Soc. Am. A **7**, 593-600.

Fu, Q., 1996: An accurate parameterization of the solar radiative properties of cirrus clouds for climate models. J. of Climate **9**, 2058-2082.

Fu, Q., P. Yang, and W.B. Sun, 1998: An accurate parameterization of the infrared radiative properties of cirrus clouds for climate models. J. Climate **11**, 2223-2237.

Fu, Q., W.B. Sun, and P. Yang, 1999: Modeling of scattering and absorption by nonspherical cirrus ice particles at thermal infrared wavelengths. J. Atmos. Sci. **56**, 2937-2947.

Goedecke, G.H., and S.G. O'Brien, 1988: Scattering by irregular inhomogeneous particles via the digitized Green's function algorithm. Appl. Opt. **15**, 2431-2437.

Han, Q., J. Chou, and R.M. Welch, 1997: Ice cloud microphysics and its temperature dependence retrieved from satellite data. SPIE proceed. **3220**, 39-47.

Harrington, R.F., 1968: Field computation by moment methods. Macmillan, New York.

Heymsfield, A.J., and C.M.R. Platt, 1984: A parameterization of the particle size spectrum of ice clouds in terms of the ambient temperature and the ice water content. J. Atmos. Sci. **41**, 846-856.

Higdon,R. L., 1986: Absorbing boundary conditions for difference approximations to the multi-dimensional wave equation. Math. Comp. **47**, 437-459.

Holland, R., and J.W. Williams, 1983: Total-field versus scattered-field finite-difference codes: A comparative assessment. IEEE Trans. Nucl. Sci. **NS-30**, 4583-4588.

Holland, R., 1994: Finite-difference time domain (FDTD) analysis of magnetic diffusion. IEEE Trans. Electromagn. Compat **36**, 32-39.

Holz, R., C.J. Stubenrauch, N.A. Scott, D.L. Mitchell, and A.J. Baran, 1998: Retrieval of cirrus cloud microphysical properties based on TOVS-3I observations. Proceedings of SPIE: conference on satellite remote sensing of clouds and the atmosphere II **3945**, Barcelona 21-24 Sept. 1998.

Jacobowitz, H., 1971: A method for computing transfer of solar radiation through clouds of hexagonal ice crystals. J. Quant. Spectrosc. Radiat. Transfer **11**, 691-695.

Katz, D. S., E. T. Thiele, and A. Taflove, 1994: Validation and extension to three dimensions of the Berenger PML absorbing boundary condition for FD-TD meshes. IEEE Microwave and Guided Wave Letters **4**, 268-270.

Kerker, M., 1969: The scattering of light and other electromagnetic radiation. Academic, New York.

Laitinen, H., and K. Lumme, 1998: T-matrix method for general star-shaped particles: first results. J. Quant. Spectrosc. Radiat. Transfer **60**, 325-334.

Liao, Z., H. L. Wong, B. Yang, and Y. Yuan, 1984: A transmitting boundary for transient wave analyses. Sci. Sin. **27**, 1063-1076.

Liou, K.N., 1972: Light scattering by ice clouds in the visible and infrared: a theoretical study. J. Atmos. Sci. **29**, 524-536.

Liou, K.N., 1986: Influence of cirrus clouds on weather and climate processes: a global perspective. Mon. Wea. Rev. **114**, 1167-1199.

Liou, K.N., and Y. Takano, 1994: Light scattering by nonspherical particles: Remote sensing and climate implications. Atmos. Res. **31**, 271-298.

Liu, Y.G., P.W. Arnott, and J. Hallett, 1998: Anomalous diffraction theory for arbitrarily-oriented finite circular cylinders and comparison with exact T-matrix results. Appl. Opt. **37**, 5019-5029.

Luebbers, R.J., K.S. Kunz, M. Schneider, and F. Hunsberger, 1991: A finite-difference time domain near zone to far zone transformation. IEEE Trans. Antennas and Propagation **AP-39**, 429-433.

Macke, A., J. Muller, and E. Raschke, 1996: Single scattering properties of atmospheric ice crystals. J. Atmos. Sci. **53**, 2813-2825.

Maslowska, A., P. J. Flatau, and G. L. Stephens, 1994: On the validity of the anomalous diffraction theory to light scattering by cubes. Optics Communications **107**, 35-40.

Merewether, D. E., R. Fisher, and F. W. Smith, 1980: On implementing a numeric Huygens's source in a finite difference program to illustrate scattering bodies. IEEE Trans. Nucl. Sci. **NS-27**, 1829-1833.

Mie, G., 1908: Beigrade zur optik truber medien, speziell kolloidaler metallosungen. Ann. Physic., **25**, 377-445.

Miloshevich, L.M., A.J. Heymsfield, and P.M. Norris, 1992: Microphysical measurements in cirrus clouds from ice crystal replicator sonders launched during FIRE II. Procedings of the 11th International Conference on Clouds and Precipitation, Elsevier Science Publishers, Montreal, 525-528 (17-21 August 1992).

Mishchenko, M.I., L.D. Travis, and A. Macke, 1996a: Scattering of light by polydisperse, randomly oriented, finite circular cylinders. Appl. Opt. **35**, 4927-4940.

Mishchenko, M.I., L.D. Travis, and D.W. Mackowski, 1996b: T-matrix computations of light scattering by nonspherical particles. A review. J. Quant. Spectrosc. Radiat. Transfer **55**, 535-575.

Mitchell, D.L., and W.P. Arnott, 1994: A model predicting the evolution of ice particle size spectra and radiative properties of cirrus clouds. Part II: dependence of absorption and extinction on ice crystal morphology. J. Atmos. Sci. **51**, 817-832.

Mitchell, D.L., 1995: How appropriate is Mie theory for predicting the radiative properties of atmospheric particles ? GEWEX News **February**, 7-11.

Mitchell, D.L., S.K. Chai, Y. Liu, A.J. Heymsfield, and Y. Dong, 1996: Modeling cirrus clouds. Part I: treatment of bimodal size spectra and case study analysis. J. Atmos. Sci. **53**, 2952-2966.

Morgan, M.A., 1981: Finite element calculation of microwave absorption by the cranial structure. IEEE Trans. Biomed. Eng. **BME-28**, 687-695.

Mugnai, A., and W.J. Wiscombe, 1986: Scattering from nonspherical Chebyshev particles. Appl. Opt. **25**, 1235-1244.

Muinonen, K., 1989: Scattering of light by crystals: a modified Kirchhoff approximation. Appl. Opt. **28**, 3044-3050.

Mundy, W.C., J.A. Roux, and A.M. Smith, 1974: Mie scattering by spheres in an absorbing medium. J. Opt. Soc. Am. **64**, 1593-1597.

Mur, G., 1981: Absorbing boundary condition for the finite-difference approximation of the time-domain electromagnetic-field equations. IEEE Trans. Electromagn. Compat. **EMC-23**, 377-382.

Nadobny, J., D. Sullivan, P. Wust, M. Seebass, P. Deuflhard, and R. Felix, 1998: A high-resolution interpolation at arbitrary interfaces for the FDTD method. IEEE Trans. Microwave Theory Tech. **46**, 1759-1766.

Napper, D.H., 1967: A diffraction theory approach to the total scattering by cubes. Kolloid Z. Z. Polym. **218**, 41-46.

Ono, A., 1969: The shape and riming properties of ice crystals in natural clouds. J. Atmos. Sci. **26**, 138-147.

Pinnick, R.G., S.C. Hill, P. Nachman, G. Videen, G. Chen, and R.K. Chang, 1998: Aerosol fluorescence spectrum analyzer for measurement of single micron-sized airborne biological particles. Aerosol Sci. and Technol. **28**, 95-104.

Plass, G.N., and G.W. Kattawa, 1968: Radiative transfer in water and ice clouds in the visible and infrared region. Appl. Opt., **10**, 738-749.

Purcell, E. M., and C. P. Pennypacker, 1973: Scattering and absorption of light by nonspherical dielectric grains. Astrophys. J. **196**, 705-714.

Quinten, M., and J. Rostalski, 1996: Lorenz-Mie theory for spheres immersed in an absorbing host medium. Part. Part. Syst. Charact. **13**, 89-96.

Rayleigh, 1871: On the light from the sky, its polarization and colour. Phil. Mag. **41**, 107-120, 274-279.

Rayleigh, 1918: The dispersal of light by a dielectric cylinder. Phil. Mag. **36**, 365-376.

Schelkunoff, S.A., 1943: Electromagnetic waves. van Nostrand, New York.

Secker, D.R., P.H. Kaye, R. Greenaway, E. Hirst, D. Bartley, and G. Videen, 2000: Light scattering from deformed droplets and droplets with inclusions: I. Experimental Results. Appl. Opt. (Submitted)

Singham, S.B., and C.F. Bohren, 1987: Light scattering by an arbitrary particle: a physical reformation of the coupled dipole method. Opt. Lett. **12**, 10-12.

Stamnes, K., S. Tsay, W. Wiscombe, and K. Jayaweera, 1988: Numerically stable algorithm for discrete-ordinate-method radiative transfer in multiple scattering and emitting layered media. Appl. Opt. **27**, 2502-2509.

Starr, D.O., 1987: A cirrus cloud experiment: Intensive field observations planned for FIRE. Bull. Amer. Meteor. Soc. **68**, 119-124.

Stephens, G.L., 1980: Radiative properties of cirrus clouds in the infrared region. J. Atmos. Sci. **37**, 435-446.

Stephens, G.L., 1984: Scattering of plane waves by soft obstacles: anomalous diffraction theory for circular cylinders. Appl. Opt. **23**, 954-959.

Stephens, G.L., S. C. Tsay, P. W. Stackhouse and P. J. Flatau, 1990: The relevance of the microphysical properties of cirrus clouds to climate and climatic feedback. J. Atmos. Sci. **47**, 1742-1753.

Strabala, K.I., S.A. Ackerman, and W.P. Menzel, 1994: Cloud properties inferred from 8-12 μm data. J. Appl. Meteorol. **33**, 212-229.

Streekstra, G.J., Hoekstra, A.G. and Heethaar, R.M., 1994: Anomalous diffraction by arbitrarily oriented ellipsoids: application in ektacytometry. Appl. Opt. **33**, 7288-7296.

Stubenrauch, C.J., R. Holz, A. Chedin, D.L. Michell, and A.J. Baran, 1999: Retrieval of cirrus ice crystal size from 8.3 and 11.1 μm emissivities determined by the improved initialization inversion of TIROS-N Operational Vertical Sounder Observations. J. Geophys. Res. **104**, 31,793-31,808.

Sullivan, D.M., 1996: A simplified PML for use with the FDTD method. IEEE Microwave and guided wave letters **6**, 97-99.

Sun, Z., and K.P. Shine, 1995: Parameterization of ice cloud radiative properties and its application to the potential climatic importance of mixed-phase clouds. J. Climate **8**, 1874-1888.

Taflove, A., 1975: Computation of the electromagnetic fields and induced temperatures within a model of the microwave-irradiated human eye. Ph.D. dissertation, Northwestern University.

Taflove, A., and M. E. Brodwin, 1975: Numerical solution of steady-state electromagnetic scattering problems using the time-dependent Maxwell's equations. IEEE Trans. Microwave Theory Tech. **MTT-23**, 623-630.

Taflove, A., 1995: Computational electrodynamics: The finite-difference time domain method. Artech House, Boston.

Tai, C.T., 1971: Dyadic Green's functions in electromagnetic theory. International Textbook, Scranton, Pa.

Takano, Y., and K. Jayaweera, 1985: Scattering phase matrix for hexagonal ice crystals computed for ray optics. Appl. Opt. **24**, 3254-3263.

Takano, Y., and K.N. Liou, 1989: Solar radiative transfer in cirrus clouds. Part I: single scattering and optical properties of hexagonal ice crystals. J. Atmos. Sci. **46**, 3-19.

Takano, Y., K.N. Liou, and P. Minnis, 1992: The effects of small ice crystals on cirrus infrared radiative properties. J. Atmos. Sci. **49**, 1487-1493.

Tuminello, P.S., E.T. Arakawa, B.N. Khare, J.M. Wrobel, M.R. Querry, and M.E. Milham, 1997: Optical properties of Bacillus subtilis spores from 0.2 to 2.5 μm. Appl. Opt. **36**, 2818-2824.

Umashankar, K.R., and A. Taflove, 1982: A novel method to analyze electromagnetic scattering of complex objects. IEEE Trans. Electromagnetic Compatibility **24**, 397-405.

van de Hulst, H.C., 1957: Light scattering by small particles. Wiley, New York.

Videen, G., D. Ngo, and M.B. Hart, 1996: Light scattering from a pair of conducting, osculating spheres. Opt. Comm. **125**, 275-287.

Videen, G., W.B. Sun, Q. Fu, D.R. Secker, R. Greenaway, P.H. Kaye, E. Hirst, and D. Bartley, 2000: Light scattering from deformed droplets and droplets with inclusions: II. Theoretical treatment. Appl. Opt. (Submitted)

Videen, G., W.B. Sun and Q. Fu, 1998: Light scattering from irregular tetrahedral aggregates. Opt. Comm., **156**, 5-9.

Wait, J. R., 1955: Scattering of a plane wave from a circular dielectric cylinder at oblique incidence. Can. J. Phys. **33**, 189-195.

Warren, S.G., 1984: Optical constants of ice from ultraviolet to the microwave. Appl. Opt. **19**. 3057-3067.

Waterman. P.C., 1971: Symmetry, unitarity and geometry in electromagnetic scattering. Phys. Rev. D**3**, 825-839.

Wielaard. D.J., M.I. Mischenko, A. Macke, and B.E. Carlson. 1997: Improved T-matrix computations for large, nonabsorbing and weakly absorbing nonspherical particles and comparison with geometrical-optics approximation. Appl. Opt. **36**, 4305-4313.

Xu, J., Z. Chen, and J. Chuang, 1997: Numerical implementation of PML in the TLM-based finite-difference time-domain grids. IEEE Transactions on Microwave Theory and Techniques **45**, 1263-1266.

Xu, J., J.G. Ma, and Z. Chen, 1998: Numerical validations of a nonlinear PML scheme for absorption of nonlinear electromagnetic waves. IEEE Transactions on Microwave Theory and Techniques **46**, 1752-1758.

Yang, P., and K.N. Liou, 1995: Light scattering by hexagonal ice crystals: comparison of finite-difference time domain and geometric optics models. *J. Opt. Soc. Am. A* **12**, 162-176.

Yang, P., and K.N. Liou, 1996a: Finite-difference time domain method for light scattering by small ice crystals in three-dimensional space. J. Opt. Soc. Am. A **13**, 2072-2085.

Yang, P., and K.N. Liou, 1996b: Geometric-optics integral-equation method for light scattering by nonspherical ice crystals. Appl. Opt. **35**, 6568-6584.

Yang, P., and K.N. Liou, 1998a: An efficient algorithm for truncating spatial domain in modeling lighting scattering by finite-difference technique. J. Compt. Phys., **140**, 346-369.

Yang, P., and K.N. Liou, 1998b: Application of finite-difference time domain technique to light scattering by irregular and inhomogeneous particles. Conference on Light Scattering by Nonspherical Particles, American Meteorology Society, New York (29 September-1 October 1998).

Yee, K.S., 1966: Numerical solution of initial boundary value problems involving Maxwell's equation in isotropic media. IEEE Trans. Antennas Propag. **AP-14**, 302-307.

Yee, K.S., D. Ingham, and K. Shlager, 1991: Time-domain extrapolation to the far field based on FDTD calculations. IEEE Trans. Antennas Propag. **AP-39**, 410-413.